Molecular Simulation of Expanding Matter and Nuclear Multifragmentation

Shinpei CHIKAZUMI

A dissertation submitted to the Doctoral Program
in Physics, the University of Tsukuba
in partial fulfillment of the requirements
for the degree of Doctor of Philosophy in Science

January 2002

Abstract

A new model based on Quantum Molecular Dynamics (QMD) is developed to investigate the instability and the fragmentation of expanding nuclear matter, where generalized periodic boundary conditions make it possible to simulate the dynamics of fragmentation free from the complication of the finiteness of the system.

The equation of state (EOS) of static nuclear matter is calculated by the Metropolis method with the QMD potential. As compared to the EOS, the spinodal region of expanding nuclear matter is calculated by the new model. To investigate how expanding motion affects the liquid-gas phase transition, the new model is applied to the quasi static expanding matter with the Lennard-Jones (LJ) potential, which is compared with the coexistent region calculated by the Gibbs ensemble method for static matter.

The fragment mass distribution resulting from expanding matter is investigated and is compared with that of static matter. The exponential distribution is obtained from rapid expanding nuclear matter which corresponds to the participant region in heavy ion collision with large radial flow, where the slope increases with increasing speed of expansion. On the other hand, slowly expanding nuclear matter which corresponds to a spectator generates a power law which is different from the power law obtained in thermal equilibrium which is assumed in the Fisher's droplet model. To elucidate the general feature of fragmentation of the expanding matter, the LJ system is also investigated.

Contents

Chapter 1

Introduction

Fragmentations caused by instability are ubiquitous phenomena, which have been studied in several branches of physics [1, 2]. In the field of nuclear physics, the instability of nuclear matter has been an attractive topic in connection with the equation of state [3, 4, 5, 6, 7, 8, 9, 10]. In order to investigate the instability of nuclear matter, a lot of heavy-ion collision experiments have been conducted [11, 12, 13, 14, 15, 16, 17]. An expanding fire ball created in the collisions is a typical experimental example of energetic nuclear matter. The fire ball explodes and generates many fragments simultaneously, which is multifragmentation.

The mechanism of multifragmentation can be investigated from the fragment mass distributions $Y(A)$, where A is the fragment mass. The feature of fragment mass distribution depends on the source where fragmentation occurs. As two important sources of multifragmentation, the participant region and the spectator region are identified. The former is the overlap region of target and projectile in heavy-ion reaction where compression and decompression play an important role, and the latter is non-overlapping region where thermal excitation is dominant. In the participant region, the fragment mass distribution shows an exponential shape $Y(A) = \exp[-\lambda A]$, where λ depends on the speed of the radial flow [12, 14]. On the other hand, in the spectator region, the distribution obeys a power law $Y(A) = A^{-\tau}$, where τ is a critical exponent [11, 13].

In particular, the power law distribution has attracted many authors' interest because the power law is predicted by the Fisher's droplet model as a signature of the liquid-gas phase transition in the vicinity of the critical point [18]. According to the model, nuclear matter undergoes a second order liquid-gas phase transition. However, the Fisher's droplet model is based on the thermal statistical physics, namely it is assumed that the system is in thermal equilibrium. Although the power law is observed experimentally and is attached to spectator region where non-equilibrium effects is thought to play a minor role, it is not clear that thermal equilibrium is fulfilled in the system.

Molecular dynamics (MD) simulations are suitable to deal with the fragmentations under non-equilibrium condition. In order to simulate heavy ion collisions, an extension of MD from a classical MD with the Lennard-Jones potential [19, 20, 21] into more advanced MD including quantum effects has been achieved. Among these

advanced MD, Quantum Molecular Dynamics (QMD) [22] is a semi-classical MD, which describes the nuclear many-body system in terms of gaussian wave packets. The anti-symmetrized version of the QMD are Anti-symmetrized Molecular Dynamics (AMD) [23] and Fermionic Molecular Dynamics (FMD) [24, 25]. These advanced MD approach have succeeded in describing several aspects of fragment production in heavy-ion reaction. Nevertheless it does not mean that the MD can fully elucidate the mechanism of multifragmentation, especially the property of the nuclear phase transition. This is because the result of MD simulation for finite system is too complicated to extract the general properties of multifragmentation. From another point of view, the finiteness of heavy-ion reaction is a main reason of complication to investigate the property of hot nuclear matter. For instance, the surface of a fireball is likely to affect the instability of the system and thus the resultant fragment mass distribution.

What we intend in this thesis is to develop a new model which links more directly the properties of nuclear matter and the multifragmentation. With this model, we try to understand more systematically the mechanism of multifragmentation which follows from the properties of hot and expanding nuclear matter. Special interest is devoted to investigate the role of the liquid-gas phase transition in dynamically evolving matter. At the same time, we try to obtain more directly the property of such excited nuclear matter by applying the model to the multifragmentation analysis. For this purpose, we also investigate the Lennard-Jones system in addition to QMD model as an example of matter governed by the different interaction. Since we start from such motivation, we disregard some feature of multifragmentation which originates from the finiteness of the nuclear system, like surface effect.

The QMD with periodic boundary condition was applied for the first time in [26] to investigate the surface structure of the neutron star. As opposed to several models based on plane waves, nuclear matter below saturation density shows nonuniform structure in the framework of the QMD based on wave packets. In [26], the structure of nuclear matter at subsaturation density shows some exotic shapes which change according to the change of the density.

In this study, we generalize the QMD with periodic boundary condition to expanding nuclear matter, which corresponds to a fire ball without surface. The time evolution of expanding nuclear matter is carried out in the framework of the QMD under a generalized periodic boundary condition [27, 28, 29]. This generalized periodic boundary condition enables us to simulate the dynamics of fragmentation free from the complication due to the finiteness of the system. When the expansion is slow, it simulates a spectator region where the collective motion is small. On the other hand, the rapid expansion simulates a participant region where collective motion plays an important role. The rate of expansion is controlled by one parameter (h). By changing h, we can investigate both spectator and participant regions. One of our main purpose is to investigate how the fragment mass distribution depends on expansion velocities and temperatures. Slow expanding matter is expected to generate a power law distribution, while rapid expanding matter is expected to show an exponential shape.

When $h = 0$, the system is just in a static thermal equilibrium state with tem-

perature (T), which is similar to what is assumed in Fisher's droplet model. The Metropolis method [30] is used to calculate configurations of the static nuclear matter in wide range of densities and temperatures, where the energy and the pressure are calculated in order to investigate the stability condition of nuclear matter. On the other hand, it is possible to calculate the instantaneous pressure and the effective temperature during the time evolution of the expanding matter. In this case, from the change of the pressure and the temperature, we analyze the dynamical instability of the system. How the expanding motion affects the nuclear phase transition defined in thermal equilibrium is our main concern of the liquid-gas phase transition.

Expanding matter is not restricted to nuclear matter [28, 29]. Using a classical MD instead of QMD, the expanding matter composed of classical particles can be simulated. We perform the expanding matter model with the Lennard-Jones (LJ) potential to investigate general features of expanding matter. The LJ system is a typical example to show the liquid-gas phase transition in thermal equilibrium. Therefore, the expanding matter model with the LJ potential is used to investigate how the expanding motion affects the liquid-gas phase transition. Furthermore, it is possible to calculate the exact coexistent region for the LJ system by the Gibbs ensemble method [30] (see Appendix C). Therefore we can compare directly the density-temperature curve in the expanding matter model with the coexistent region.

In this thesis, two topics are mainly discussed using the expanding matter model. One is the instability of the expanding matter, and the other is the fragment mass distributions resulting from the instability. The latter is a main source of the experimental information for the stability of excited matter.

This thesis is based on [31, 32] and organized as follows. In Chapter 2, we will explain how the expanding matter model works. In the model, the QMD with generalized periodic boundary condition is developed to solve the equations of motion and the Metropolis method is used to prepare static nuclear matter, which is also used as an initial state of expanding matter model. We will see that the time evolution of the expanding matter is subject to only two parameters: the initial temperature T and the expanding velocity h.

Chapter 3 is devoted to discussion of the instability of the expanding matter. The Metropolis method enables us to calculate the equation of state (EOS) of static nuclear matter in wide range of densities and temperatures, where the spinodal region is identified. On the other hand, the pressure and the temperature calculated during the time evolution of the expanding matter gives another spinodal region for dynamical system. These two spinodal regions are compared to investigate how the expanding motion affects the instability of nuclear matter. Furthermore, to confirm general features of expanding matter, the same calculation is repeated with the classical Molecular Dynamics with Lennard-Jones system, the coexistent region of which can be exactly calculated by the Gibbs ensemble method.

In Chapter 4, we concentrate on the fragment mass distribution coming from the expanding matter. The distribution is expected to depend on both the initial temperature T and the expanding velocity h. We will see that slow expanding

matter gives a power law, while rapid expanding matter gives an exponential shape. The LJ expanding matter is again examined to confirm what is the general feature of the distribution.

In Chapter 5, the conclusion is given.

Chapter 2

Molecular simulation

In this chapter, we will discuss molecular simulations used to investigate the property of nuclear matter. Molecular simulations are composed of Molecular Dynamics (MD) simulations and Monte Carlo simulations, the former is used to deal with non-equilibrium phenomena directly with equation of motions and the latter is used to calculate specific ensembles based on statistical mechanics [30].

Expanding nuclear matter, which is a main object of this study, is simulated by an expanding matter model, where saturated nuclear matter at a certain temperature is given as an initial state by the Metropolis method and afterward boosted in such a way that the matter expands homogeneously. The time evolution of expanding nuclear matter is calculated based on the equation of motion of the Quantum Molecular Dynamics (QMD) under generalized periodic boundary conditions.

The QMD is a MD simulation developed to treat nuclear system, which has been developed to simulate heavy ion reaction experiments [22] and is the basis of more advanced MD with wave packets like the Anti-symmetrized Molecular Dynamics (AMD) and the Fermionic Molecular Dynamics (FMD). With periodic boundary conditions, static nuclear matter can be described in the framework of the QMD [26]. What we will show in this thesis is that we can extend the model to dynamically expanding system.

Metropolis method is the simplest one in several Monte Carlo simulations for ensemble calculations, which calculates configurations subject to canonical ensembles. That is, static matter for a given density and temperature can be obtained by this method. This method is used in this thesis to calculate the statistical properties of matter.

In the following, we will start with the framework of the QMD and discuss the method to apply the QMD to nuclear matter. After that, the Metropolis method which uses the same interaction as that of QMD is explained. The Metropolis method gives not only the initial state of the expanding matter model but also the equation of state (EOS) of nuclear matter. Finally, the expanding matter model is introduced, where generalized periodic boundary conditions to simulate infinite matter with expanding motion is explained.

2.1 Quantum molecular dynamics (QMD)

The Quantum Molecular Dynamics (QMD) is a Molecular Dynamics (MD) which has been developed to simulate heavy ion reactions experiments, where nucleons are expressed in terms of gaussian wave packets. The QMD Lagrangian is obtained by replacing the anti-symmetrized state of the Anti-symmetrized Molecular Dynamics (AMD) by a tensor products of single particle states. This simplicity leads to a simple Hamilton's equation. The Hamiltonian has the effective interaction which includes momentum dependent parts to compensate the lack of anti-symmetrization in the many-body state. The parameters in the effective interaction are determined under periodic boundary conditions so as to reproduce several properties of nuclear matter. In the following, we will explain the framework of the QMD and the method to apply the QMD to nuclear matter.

2.1.1 Gaussian wave packets

A gaussian wave packet is regarded as the coordinate representation of a coherent state. In general, a coherent state is an eigenstate of annihilation operator as follows:

$$\hat{\mathbf{a}}|\phi_{\mathbf{Z}}\rangle = \mathbf{Z}|\phi_{\mathbf{Z}}\rangle, \tag{2.1}$$

where $\hat{\mathbf{a}}$ is an annihilation operator and $\mathbf{Z}$ is the eigenvalue of the coherent state $|\phi_{\mathbf{Z}}\rangle$. Assuming that $\langle\phi_{\mathbf{Z}}|\phi_{\mathbf{Z}}\rangle = 1$, the following expression is obtained:

$$|\phi_{\mathbf{Z}}\rangle = \frac{e^{\mathbf{Z}\cdot\hat{\mathbf{a}}^{\dagger}}}{e^{\frac{1}{2}|\mathbf{Z}|^2}}|0\rangle, \tag{2.2}$$

where $\hat{\mathbf{a}}^{\dagger}$ is a creation operator and $|0\rangle$ is the vacuum state defined as $\hat{\mathbf{a}}|0\rangle = 0$. To express $|\phi_{\mathbf{Z}}\rangle$ in terms of the coordinate of a particle $\mathbf{r}$, remember the operator transformation in view of harmonic oscillators:

$$\hat{\mathbf{a}} = \sqrt{\nu}\hat{\mathbf{r}} + \frac{i}{2\hbar\sqrt{\nu}}\hat{\mathbf{p}}, \tag{2.3}$$

where ν is a parameter and $\hat{\mathbf{p}}$ is the momentum of a particle. With the help of this relation, a gaussian wave packet is obtained as a coordinate representation of coherent states:

$$\langle\mathbf{r}|\phi_{\mathbf{Z}_i}\rangle = \left(\frac{2\nu}{\pi}\right)^{\frac{3}{4}}\exp\left[-\nu\left(\mathbf{r} - \frac{\mathbf{Z}_i}{\sqrt{\nu}}\right)^2 + \frac{1}{2}\mathbf{Z}_i^2\right]. \tag{2.4}$$

This expression is widely used in the literatures regarding AMD and FMD [23, 25], where $\mathbf{Z}_i$ is introduced for the i-th nucleon. In the framework of AMD, $\mathbf{Z}_i(i = 1, 2, \cdots, N)$ are variational parameters to represent a system of N identical particles. In the case of QMD, it is assumed that a system of N identical particles is represented by a tensor product of $\langle\mathbf{r}|\phi_{\mathbf{Z}_i}\rangle$. As a result, it is possible to discuss each single

particle state $\langle \mathbf{r}|\phi_{\mathbf{Z}_i}\rangle$ independently. In this case, $\mathbf{Z}_i$ includes the information about the position and momentum of the i-th nucleon. If we define $\mathbf{R}_i$ and $\mathbf{P}_i$ as

$$\mathbf{Z}_i = \sqrt{\nu}\mathbf{R}_i + \frac{i}{2\hbar\sqrt{\nu}}\mathbf{P}_i, \tag{2.5}$$

we get the following expression by substituting this into Eq. (2.4):

$$\langle \mathbf{r}|\phi_{\mathbf{Z}_i}\rangle = \left(\frac{2\nu}{\pi}\right)^{\frac{3}{4}}\exp\left[-\nu(\mathbf{r}-\mathbf{R}_i)^2 + \frac{i}{\hbar}\mathbf{r}\cdot\mathbf{P}_i\right]. \tag{2.6}$$

From this equation, we find that $\mathbf{R}_i$ and $\mathbf{P}_i$ stand for the expectation values of the position and momentum of i-th particle respectively.

2.1.2   Lagrangian

Let us derive the QMD Lagrangian in a formal way. The most general expression of Lagrangian is given as follows:

$$L \equiv \frac{\langle \Phi(Z)|(i\hbar\frac{d}{dt} - \mathcal{H})|\Phi(Z)\rangle}{\langle \Phi(Z)|\Phi(Z)\rangle}, \tag{2.7}$$

where $\mathcal{H}$ is the Hamiltonian density of the whole system and $|\Phi(Z)\rangle$ is the corresponding many body state composed of $|\phi_{\mathbf{Z}_1}\rangle, |\phi_{\mathbf{Z}_2}\rangle, \cdots, |\phi_{\mathbf{Z}_N}\rangle$. Calculating the derivative of $|\Phi(Z)\rangle$ with respect to t, the Lagrangian is expressed as follows:

$$L = i\hbar \sum_{j\alpha} \frac{\partial}{\partial Z_{j\alpha}} \ln\langle \Phi(Z)|\Phi(Z)\rangle \frac{dZ_{j\alpha}}{dt} - \frac{\langle \Phi(Z)|\mathcal{H}|\Phi(Z)\rangle}{\langle \Phi(Z)|\Phi(Z)\rangle}, \tag{2.8}$$

where $\alpha = x, y, z$. Assuming that $|\Phi(Z)\rangle$ is the tensor products of $|\phi_{\mathbf{Z}_i}\rangle$ ($i = 1, 2, \cdots, N$), the following simple Lagrangian is obtained:

$$L = i\hbar \sum_{j\alpha} Z_{j\alpha}^{\star} \frac{dZ_{j\alpha}}{dt} - H(\mathbf{R}^N, \mathbf{P}^N, \chi^N), \tag{2.9}$$

where $\mathbf{R}^N$, $\mathbf{P}^N$ and χ^N stand for $\mathbf{R}_i$, $\mathbf{P}_i$ and χ_i ($i = 1, 2, \cdots, N$) respectively and χ_i indicates the spin and the isospin of i-th nucleon. Notice that the Hamiltonian is expressed in terms of new variables.

2.1.3   Equation of motion

The equation of motion is derived from the following Lagrange's equation:

$$\frac{d}{dt}\left(\frac{\partial L}{\partial \frac{dZ_{j\alpha}^{\star}}{dt}}\right) - \frac{\partial L}{\partial Z_{j\alpha}^{\star}} = 0. \tag{2.10}$$

The derivative of the Hamiltonian in terms of $Z_{j\alpha}^{\star}$ can be transformed into the following form:

$$\frac{\partial H(\mathbf{R}^N, \mathbf{P}^N, \chi^N)}{\partial Z_{j\alpha}^{\star}} = i\hbar\sqrt{\nu}\frac{\partial H(\mathbf{R}^N, \mathbf{P}^N, \chi^N)}{\partial P_{j\alpha}} + \frac{1}{2\sqrt{\nu}}\frac{\partial H(\mathbf{R}^N, \mathbf{P}^N, \chi^N)}{\partial R_{j\alpha}}. \tag{2.11}$$

With this relation, the Lagrange's equation is separated into real and imaginary part, which are found to be the following Hamilton's equations:

$$\frac{dR_{j\alpha}}{dt} = \frac{\partial H(\mathbf{R}^N, \mathbf{P}^N, \chi^N)}{\partial P_{j\alpha}}, \qquad (2.12)$$

$$\frac{dP_{j\alpha}}{dt} = -\frac{\partial H(\mathbf{R}^N, \mathbf{P}^N, \chi^N)}{\partial R_{j\alpha}}. \qquad (2.13)$$

In this way, the time evolution of QMD is subject to N sets of the Hamilton's equations. To solve the equations of motion, the fourth order Runge-Kutta method is used (see Appendix B.1).

Notice that $\mathbf{R}_j$ and $\mathbf{P}_j$ are the eigenvalues of the position and the momentum of the coherent state $|\phi_{\mathbf{Z}_j}\rangle$:

$$\hat{\mathbf{r}}|\phi_{\mathbf{Z}_j}\rangle = \mathbf{R}_j|\phi_{\mathbf{Z}_j}\rangle, \qquad (2.14)$$

$$\hat{\mathbf{p}}|\phi_{\mathbf{Z}_j}\rangle = \mathbf{P}_j|\phi_{\mathbf{Z}_j}\rangle. \qquad (2.15)$$

This relations allow us to regard $\mathbf{R}_j$ and $\mathbf{P}_j$ as the position and the momentum of the j-th particle.

2.1.4 Effective interaction

The equation of motion is subject to the Hamiltonian, which is expressed in terms of the position, the momentum and the internal degrees of freedom:

$$\frac{\langle \Phi(Z)|\mathcal{H}|\Phi(Z)\rangle}{\langle \Phi(Z)|\Phi(Z)\rangle} = H(\mathbf{R}^N, \mathbf{P}^N, \chi^N). \qquad (2.16)$$

The Hamiltonian operator is composed of the kinetic energy operator and the potential energy operator. The expectation value of the kinetic energy operator in the anti-symmetrized state includes a function which represents the Pauli exclusion effect. In the QMD, this function is approximated by the Pauli potential, which is a two body potential expressed in terms of the relative momentum and the relative distance. Thus, the Hamiltonian is written as follows:

$$H(\mathbf{R}^N, \mathbf{P}^N, \chi^N) = \left[\sum_{i=1}^{N} \frac{\mathbf{P}_i^2}{2M} + V_{\mathrm{Pauli}}\right] + V_{\mathrm{nucl}}, \qquad (2.17)$$

where V_{Pauli} is the Pauli potential and V_{nucl} is the nuclear potential to reproduce several properties of nuclear matter.

Pauli potential

The Pauli potential is a crude approximation of the matrix element of the kinetic energy operator in the anti-symmetrized states. The accurate expression of the matrix element is still complicated even though only two identical particles are taken into account (see Appendix A.1). Therefore, the Pauli potential is introduced

in a phenomenological way to mimic the Pauli exclusion effect. In practice, the Pauli potential is expressed as follows:

$$V_{\text{Pauli}} \equiv \frac{C_{\text{P}}}{2(q_0 p_0/\hbar c)^3} \sum_{i,j \neq i}^{N} \exp\left[-\frac{|\mathbf{R}_i - \mathbf{R}_j|^2}{2q_0^2} - \frac{|\mathbf{P}_i - \mathbf{P}_j|^2}{2p_0^2} \right] \delta_{\tau_i,\tau_j} \delta_{\sigma_i,\sigma_j}, \qquad (2.18)$$

where C_{P}, q_0, p_0 are parameters, $\hbar c = 197.3$ MeV fm, and τ_i, σ_i are the isospin and the spin of the i-th particle respectively.

The parameters are determined so that the kinetic energy fits to that of free Fermi gas. The fitting is performed in such a way that the equation of motion is solved for the Hamiltonian consisting of the Pauli potential and $\sum_{i=1}^{N} \frac{\mathbf{P}_i^2}{2M}$ and afterwards the value of $\sum_{i=1}^{N} \frac{\mathbf{P}_i^2}{2M}$ is fitted to the Fermi gas value. It is controversial if the kinetic energy should be replaced by the kinetic energy plus the Pauli potential. In this study, the Pauli potential is not regarded as the part of the kinetic energy, that is, only $\sum_{i=1}^{N} \frac{\mathbf{P}_i^2}{2M}$ is regarded as the kinetic energy. Actually, it is possible to carry out similar fitting in such a way that the kinetic plus the Pauli potential energy is in agreement with the energy of free Fermi gas.

Nuclear potential

The nuclear potential consists of several two-body interactions like:

$$V_{\text{nucl}} = \frac{1}{2} \sum_{i=1}^{N} \sum_{j=1}^{N} \langle \phi_i \phi_j | \hat{v}_{12} | \left(|\phi_i \phi_j\rangle - |\phi_j \phi_i\rangle \right), \qquad (2.19)$$

$$|\phi_i\rangle = |\phi_{\mathbf{Z}_i}\rangle \otimes |\chi_{\alpha_i}\rangle, \qquad (2.20)$$

where $|\chi_{\alpha_i}\rangle$ indicates the state vector of both the spin and the isospin for the i-th particle. There are five terms in the nuclear potential:

$$V_{\text{nucl}} = V_{\text{Skyrme}} + V_{\text{density}} + V_{\text{symmetry}} + V_{\text{Yukawa}} + V_{\text{surface}}. \qquad (2.21)$$

The V_{Skyrme} is the Skyrme interaction given as follows:

$$V_{\text{Skryme}} = \frac{1}{2} \sum_{i=1}^{N} \sum_{j=1}^{N} \langle \phi_i \phi_j | t_0 \delta(\mathbf{r}_i - \mathbf{r}_j)(1 + x_0 P_\sigma) \left(|\phi_i \phi_j\rangle - |\phi_j \phi_i\rangle \right), \qquad (2.22)$$

where t_0, x_0 are constants and P_σ is the spin-exchange operator. The Skyrme interaction includes the delta function so that the exchange term is equivalent to the direct term. Substituting the expression of $|\phi_i\rangle$ into the above formula gives the following expression:

$$V_{\text{Skyrme}} = \frac{\alpha}{2\rho_0} \sum_{i=1}^{N} \langle \rho_i \rangle, \qquad (2.23)$$

where $\alpha \equiv \frac{3}{\sqrt{2}} \rho_0 t_0$ is a constant, ρ_0 is the saturation density, $\langle \rho_i \rangle$ is an overlap of one body density ρ_i for i-th nucleon with other nucleons defined as

$$\langle \rho_i \rangle \equiv \sum_{j(\neq i)}^{N} \rho_{ij} \equiv \sum_{j(\neq i)}^{N} \int d^3 r \rho_i(\mathbf{r}) \rho_j(\mathbf{r}), \qquad (2.24)$$

11

$$\rho_i(\mathbf{r}) \equiv \langle \phi_{\mathbf{z}_i} | \mathbf{r} \rangle \langle \mathbf{r} | \phi_{\mathbf{z}_i} \rangle = \frac{1}{(2\pi L)^{\frac{3}{2}}} \exp \left\{ -\frac{1}{2L} (\mathbf{r} - \mathbf{R}_i)^2 \right\}, \qquad (2.25)$$

where $L \equiv \frac{1}{4\nu} = 1.95$ fm^2 is the squared width of the wave packet.

The V_{density} is the density-dependent potential, which is also a part of the Skyrme interaction:

$$
\begin{aligned}
V_{\text{density}} &= \frac{1}{2} \sum_{i=1}^{N} \sum_{j=1}^{N} \langle \phi_i \phi_j | t_3 \delta(\mathbf{r}_i - \mathbf{r}_j) \rho(\frac{\mathbf{r}_i + \mathbf{r}_j}{2})^{\tau-1} \left(|\phi_i \phi_j\rangle - |\phi_j \phi_i\rangle \right) \\
&= \frac{\beta}{(1+\tau)\rho_0^\tau} \sum_{i=1}^{N} \langle \tilde{\rho}_i \rangle^\tau, \qquad (2.26)
\end{aligned}
$$

where t_3, τ, β are constants and $\tilde{\rho}_i$ is given by:

$$
\begin{aligned}
\tilde{\rho}_i(\mathbf{r}) &= \frac{1}{(2\pi\tilde{L})^{\frac{3}{2}}} \exp \left\{ -\frac{1}{2\tilde{L}} (\mathbf{r} - \mathbf{R}_i)^2 \right\}, \qquad (2.27) \\
\tilde{L} &= \frac{L}{2}(\tau+1)^{\frac{1}{\tau}}. \qquad (2.28)
\end{aligned}
$$

The above relation between $\tilde{L}$ and L comes from the following condition[26]:

$$\int d^3r \left(\sum_{i=1}^{N} \rho_i(\mathbf{r}) \right)^{\tau+1} = \sum_{i=1}^{N} \left(\sum_{j=1}^{N} \int d^3r \, \tilde{\rho}_i(\mathbf{r}) \tilde{\rho}_j(\mathbf{r}) \right)^\tau. \qquad (2.29)$$

The V_{symmetry} is the symmetry potential which distinguishes the proton and the neutron:

$$
\begin{aligned}
V_{\text{symmetry}} &= \frac{1}{2} \sum_{i=1}^{N} \sum_{j=1}^{N} \langle \phi_i \phi_j | t_s (1 - 2|c_1 - c_2|) \delta(\mathbf{r}_i - \mathbf{r}_j) \left(|\phi_i \phi_j\rangle - |\phi_j \phi_i\rangle \right) \\
&= \frac{C_{\text{s}0}}{2\rho_0} \sum_{i,j \neq i}^{N} (1 - 2|c_i - c_j|)\rho_{ij}, \qquad (2.30)
\end{aligned}
$$

where $t_s, C_{\text{s}0}$ are constants, $c_i = 1$ for protons and $c_i = 0$ for neutrons. In this study, it is assumed that the proton number is equal to the neutron number so that the symmetry potential plays a miner role.

The V_{Yukawa} is the exchange term of the Yukawa potential, which has a finite range as opposed to the above Skyrme type potentials. The finite range potentials integrated over wave packets become momentum dependent like the Pauli potential. We introduce two kinds of ranges for the Yukawa potential as follows:

$$
\begin{aligned}
V_{\text{Yukawa}} &= \frac{1}{2} \sum_{i=1}^{N} \sum_{j=1}^{N} \langle \phi_i \phi_j | \left[\frac{E_1 e^{-\mu_1 |\mathbf{r}_1 - \mathbf{r}_2|}}{\mu_1 |\mathbf{r}_1 - \mathbf{r}_2|} + \frac{E_2 e^{-\mu_2 |\mathbf{r}_1 - \mathbf{r}_2|}}{\mu_2 |\mathbf{r}_1 - \mathbf{r}_2|} \right] |\phi_j \phi_i\rangle \\
&= \frac{C_{\text{ex}(1)}}{2\rho_0} \sum_{i,j \neq i}^{N} \frac{1}{1 + \left(\frac{|\mathbf{P}_i - \mathbf{P}_j|}{\mu_1 \hbar} \right)^2} \rho_{ij} + \frac{C_{\text{ex}(2)}}{2\rho_0} \sum_{i,j \neq i}^{N} \frac{1}{1 + \left(\frac{|\mathbf{P}_i - \mathbf{P}_j|}{\mu_2 \hbar} \right)^2} \rho_{ij},
\end{aligned}
$$
$$(2.31)$$

where $C_{\text{ex}(1)}, \mu_1, C_{\text{ex}(2)}, \mu_2$ are parameters and $\hbar$ is the Planck constant.

The V_{surface} is the surface potential, which is introduced to improve the geometrical structure of the finite nucleus. Without the surface interaction, the finite nucleus is distorted mainly due to the Pauli potential. The surface interaction is given by:

$$V_{\text{surface}} = \frac{V_{\text{SF}}}{2\rho_0^{5/3}} \sum_{i,j \neq i}^{N} \int d^3 r \nabla \rho_i(\mathbf{r}) \nabla \rho_j(\mathbf{r}), \tag{2.32}$$

where V_{SF} is a constant.

Putting the above terms together, the total nuclear potential is obtained as follows:

$$
\begin{aligned}
V_{\text{nucl}} \equiv \ & \frac{\alpha}{2\rho_0} \sum_{i=1}^{N} \langle \rho_i \rangle + \frac{\beta}{(1+\tau)\rho_0^\tau} \sum_{i=1}^{N} \langle \rho_i \rangle^\tau + \frac{C_{\text{s0}}}{2\rho_0} \sum_{i,j \neq i}^{N} (1 - 2|c_i - c_j|)\rho_{ij} \\
& + \frac{C_{\text{ex}(1)}}{2\rho_0} \sum_{i,j \neq i}^{N} \frac{1}{1 + \left(\frac{|\mathbf{P}_i - \mathbf{P}_j|}{\mu_1 \hbar}\right)^2} \rho_{ij} + \frac{C_{\text{ex}(2)}}{2\rho_0} \sum_{i,j \neq i}^{N} \frac{1}{1 + \left(\frac{|\mathbf{P}_i - \mathbf{P}_j|}{\mu_2 \hbar}\right)^2} \rho_{ij} \\
& + \frac{V_{\text{SF}}}{2\rho_0^{5/3}} \sum_{i,j \neq i}^{N} \int d^3 r \nabla \rho_i(\mathbf{r}) \nabla \rho_j(\mathbf{r}). \tag{2.33}
\end{aligned}
$$

Parameter fitting

There are many parameters in the effective interaction. It is difficult to set these parameters in systematic way. In practice, the fitting is carried out step by step as given in [26] and [33]. There are four requirements from experimental data.

- The property of free Fermi gas

- The real part of the optical potential

- The equation of state

- The property of finite nucleus

The effective interaction should satisfy the above requirements, which are connected to each other. It is technically crucial to determine the order of the fitting procedure, which is not unique but first of all the free Fermi gas should be taken into account.

As mentioned earlier, the parameters in the Pauli potential are fitted to the free Fermi gas. The average energy of the free Fermi gas at zero temperature is given by:

$$\frac{E}{N} = \frac{3}{10M} \left(\frac{3\pi^2}{2}\right)^{\frac{2}{3}} \rho^{\frac{2}{3}}, \tag{2.34}$$

where M is the nucleon mass. When the ground state of nuclear matter is calculated with the Hamiltonian composed of the Pauli potential and the kinetic energy, the kinetic energy of the matter should obey the above formula.
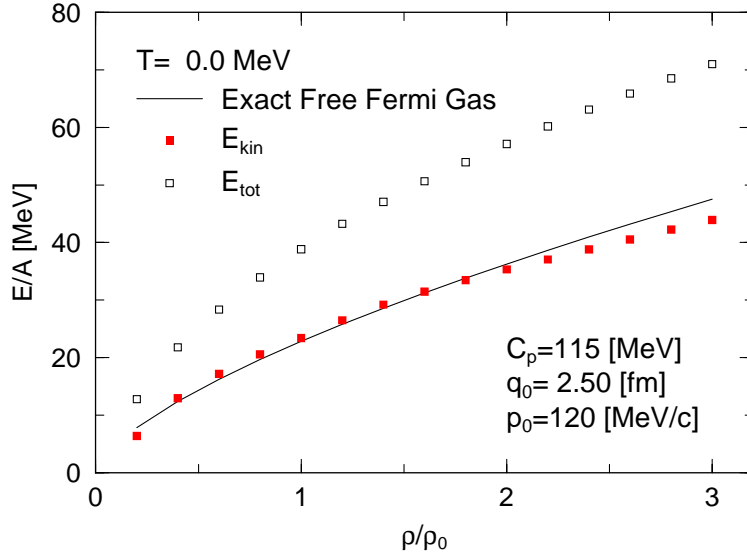
Figure 2.1: The fitting of the Fermi-gas with the Pauli potential

It is necessary to prepare the matter at zero temperature. For this purpose, the frictional cooling method is utilized. This method is carried out by calculating the equation of motion with the following damping terms:

$$\frac{dR_{j\alpha}}{dt} = \frac{\partial H(\mathbf{R}^N, \mathbf{P}^N, \chi^N)}{\partial P_{j\alpha}} + \mu_{\mathbf{R}} \frac{\partial H(\mathbf{R}^N, \mathbf{P}^N, \chi^N)}{\partial R_{j\alpha}}, \tag{2.35}$$

$$\frac{dP_{j\alpha}}{dt} = -\frac{\partial H(\mathbf{R}^N, \mathbf{P}^N, \chi^N)}{\partial R_{j\alpha}} + \mu_{\mathbf{P}} \frac{\partial H(\mathbf{R}^N, \mathbf{P}^N, \chi^N)}{\partial P_{j\alpha}}, \tag{2.36}$$

where $\mu_{\mathbf{R}}$ and $\mu_{\mathbf{P}}$ are the damping coefficients. The above equations of motion ensure that the total energy decreases as long as $\mu_{\mathbf{R}} < 0$ and $\mu_{\mathbf{P}} < 0$.

Imposing the condition that the results of the cooling calculation simulate free Fermi gas, we can fix a set of the parameters C_p, q_0, p_0 in Eq. (2.18). The values of parameters obtained are

$$
\begin{aligned}
C_{\mathbf{p}} &= 115 \text{ MeV}, \\
q_0 &= 2.5 \text{ fm}, \\
p_0 &= 120.0 \text{ MeV/c}. \tag{2.37}
\end{aligned}
$$

Figure 2.1 shows the fitting of the Fermi gas using these coefficients of the Pauli potential.

Next, consider the real part of the optical potential, which contains the information about the momentum dependence in nuclear matter at the saturation density. Assuming that nuclear matter is completely homogeneous, the potential for one nucleon with the momentum $\mathbf{P}$ in nuclear matter at the saturation density is calculated as follows:

$$U(\mathbf{p}) = \alpha + \beta + \left(\frac{4}{3}\pi p_F^3\right)^{-1} \int_0^{p_F} d^3\acute{p} \left\{ \frac{C_{ex(1)}}{1 + \left(\frac{|\mathbf{p}-\acute{\mathbf{p}}|}{\mu_1}\right)^2} + \frac{C_{ex(2)}}{1 + \left(\frac{|\mathbf{p}-\acute{\mathbf{p}}|}{\mu_2}\right)^2} \right\}$$
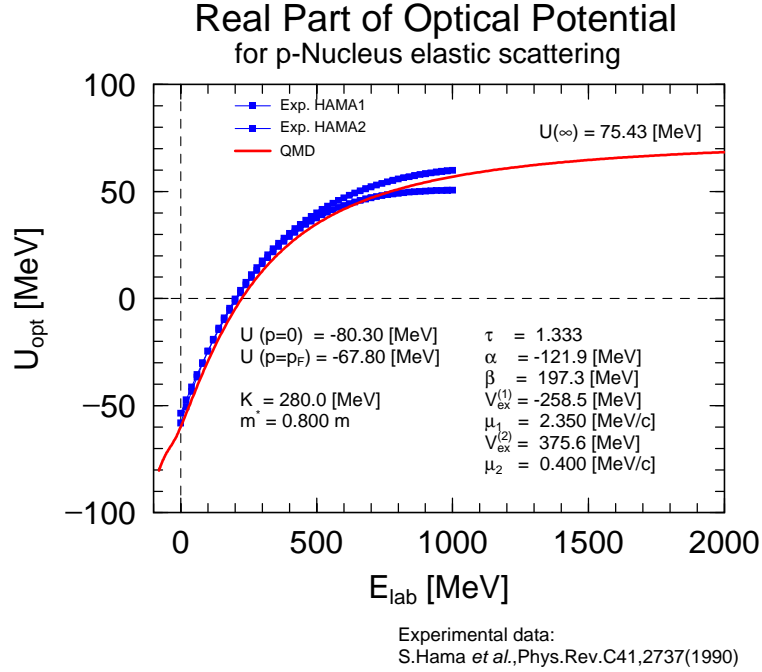
14

Figure 2.2: The real part of the optical potential

$$= \alpha + \beta + C_{ex(1)}g\left(x = \frac{\mu_1}{p_F}, y = \frac{p}{p_F}\right) + C_{ex(2)}g\left(x = \frac{\mu_2}{p_F}, y = \frac{p}{p_F}\right), \tag{2.38}$$

where p_F is the Fermi momentum and $g(x,y)$ is given by:

$$g(x,y) = \frac{3}{4}x^3 \left\{ \frac{1 + x^2 - y^2}{2xy} \ln \frac{(y+1)^2 + x^2}{(y-1)^2 + x^2} + \frac{2}{x} - 2\left\{ \arctan \frac{y+1}{x} - \arctan \frac{y-1}{x} \right\} \right\}. \tag{2.39}$$

Figure 2.2 shows the corresponding experimental data and fitted curves using the above formula subject to the following conditions [26].

$$U(0) \quad = \quad -80 \text{ MeV}, \tag{2.40}$$

$$U(p) \quad = \quad 0 \quad \text{at} \quad E_\mathrm{lab} = 200 \text{ MeV}, \tag{2.41}$$

$$U(p \to \infty) \quad = \quad 75.43 \text{ MeV}. \tag{2.42}$$

On the other hand, the derivative of the optical potential $U(p)$ in terms of the momentum p is related to the effective mass:

$$\frac{1}{m^\star} = \frac{1}{m} + \left(\frac{1}{p} \frac{\partial U(p)}{\partial p} \right)_{p=p_\mathrm{F}}. \tag{2.43}$$

In the above relation, we impose $m^\star = 0.8m$ at the saturation density. There are altogether four conditions regarding to the optical potential, thus four parameters $C_{ex(1)}, \mu_1, C_{ex(2)}, \mu_2$ are determined.
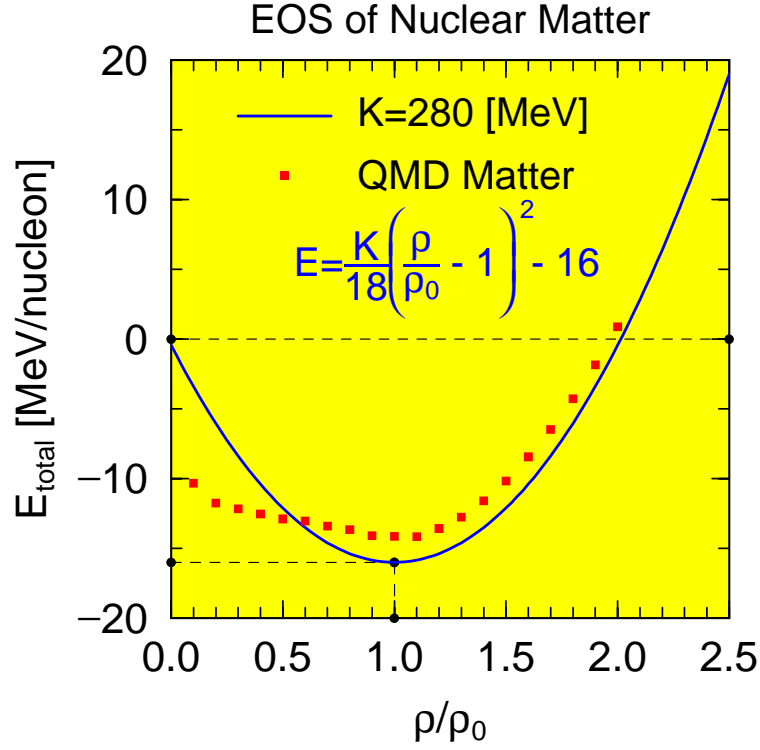
Figure 2.3: The equation of state at zero temperature

The next condition to be considered is the equation of state (EOS). It is assumed that the EOS of nuclear matter at zero temperature in the vicinity of the saturation density is expressed by a parabolic function with the ground state energy per particle -16 MeV and the incompressibility K. The incompressibility K is defined by:

$$K \equiv p_{\mathrm{F}}^2 \frac{\partial^2 E}{\partial p_{\mathrm{F}}^2}\bigg|_{\rho=\rho_0}, \qquad (2.44)$$

where E is the total energy per particle and p_{F} is the Fermi momentum. Using the fact that p_{F} is proportional to $\rho^{1/3}$, it is found that the parabolic function is obtained as follows:

$$E = -16 + \frac{K}{18}\left(\frac{\rho}{\rho_0} - 1\right)^2. \qquad (2.45)$$

This parabolic function is compared with the energy of the QMD nuclear matter at zero temperature, which is prepared by the frictional cooling method under periodic boundary conditions. Figure 2.3 shows the density dependence of the ground state QMD nuclear matter and the parabolic function with $K = 280$ MeV. Coincidence of these two constrains the value of τ and β in the density dependent potential V_{density}. It is assumed in this procedure that the value of τ is set at a typical value of $4/3$.

To fix the values of the parameters, $V_{\mathrm{SF}}, C_{\mathrm{S0}}$ and the wave packet length L, the properties of finite nucleus are used, which are the binding energy and the radius of finite nuclei. The experimental data for stable nucleus is compared with the QMD

Table 2.1: Effective interaction parameter set (K=280 MeV)

α (MeV)	-121.9	β (MeV)	197.3	τ	4/3
C_{s0} (MeV)	25.0	$C_{\mathrm{ex}(1)}$ (MeV)	-258.5	$C_{\mathrm{ex}(2)}$ (MeV)	375.6
μ_1 (MeV)	2.35	μ_2 (MeV)	0.4	V_{SF} (MeV)	20.68
C_{P} (MeV)	115.0	p_0 (MeV/c)	120.0	q_0 (fm)	2.5
L (fm^2)	1.95				

prediction for the ground state nuclei prepared by the frictional cooling. In this fitting, the Coulomb potentials is included. Figure 2.4 shows the binding energy of finite nuclei and the Fig. 2.5 shows the radius of finite nuclei. For both properties, the experimental data are in good agreement with the values calculated by the QMD.

At this stage, all parameters are determined in principle. The parameters determined by four requirements are summarized in the Table 2.1.

2.1.5   Periodic boundary condition

To simulate nuclear matter by QMD, periodic boundary conditions are imposed. Here, we will discuss general aspect of normal periodic boundary conditions.

One primitive and 26 replica cells

The purpose of periodic boundary conditions is to simulate infinite matter. Therefore, we must be careful that the periodicity caused by boundary conditions should not affect the quantities calculated in the simulation. We assume that the infinite matter is simulated in periodic cubic cells. In order to avoid the appearance of the periodicity, it is necessary that the cell size is at least larger than the twice of interaction length. It is better that the cell size is as large as possible because the correlation length is likely to be larger than the interaction length in critical conditions near phase transition.

Since we are interested in subsaturated nuclear matter, the cell size is the smallest when the density is the saturation density:

$$R_{\mathrm{cell}} = \left(\frac{N}{\rho_0} \right)^{\frac{1}{3}}, \qquad (2.46)$$

where N is the total number in a cell and $\rho_0 = 0.168$ fm^{-3} is the saturation density. We set $N = 200$ and $R_{\mathrm{cell}} = 10.6$ fm, which is not so bad because the force between two particles separated more than 5 fm is negligible with the wave packet length $L = 1.95$ fm^2.

The actual calculation is carried out for the particles in the primitive cell but these particles interact with the mirror particles in 26 replica cells surrounding the primitive cell shown in Fig. 2.6. In general, periodic boundary conditions impose additional calculation besides the calculation for the primitive cell. However, the
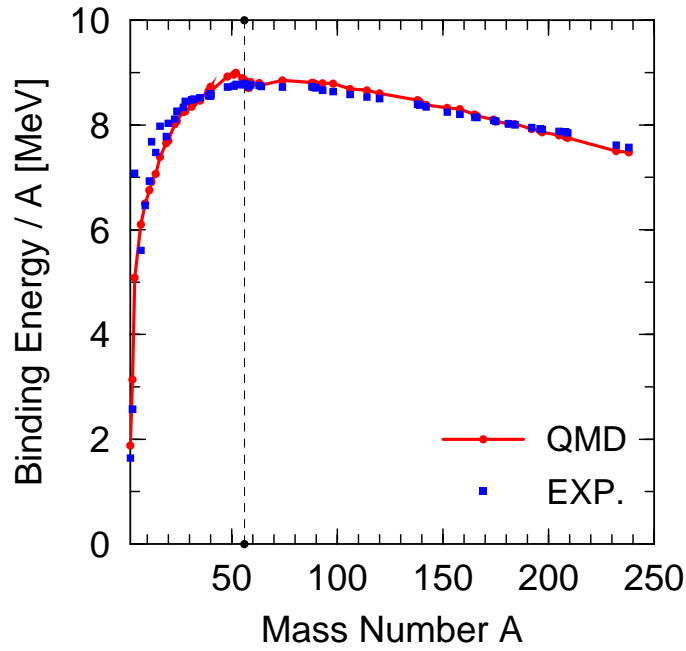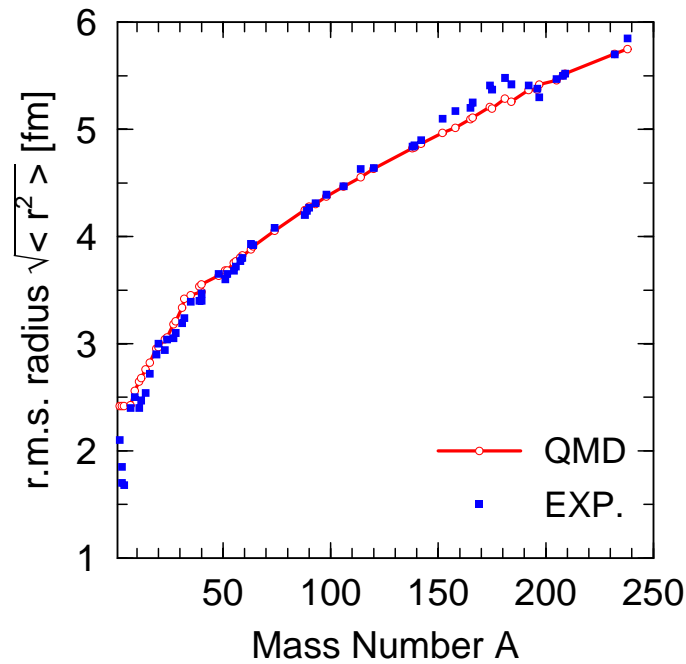
Figure 2.4: The binding energy of finite nuclei

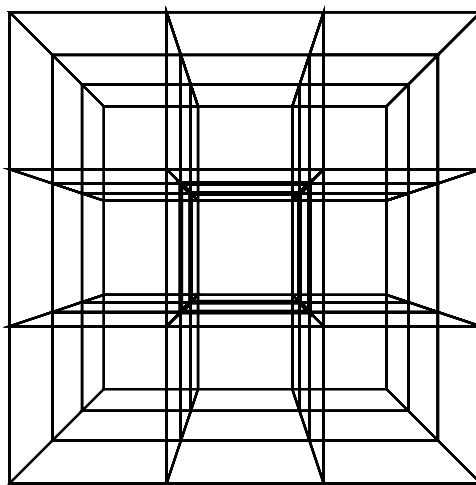Figure 2.5: The radius of finite nuclei

18

Figure 2.6: A schematic picture of periodic boundary conditions. The primitive cell marked by thick lines is surrounded by 26 replica cells.

minimum image convention given below allows us to reduce the additional computational task.

Minimum image convention

In the molecular simulation, the calculation of the force is one of the most time consuming part. When calculating the two-body interaction in the cell with N particles, we have to check $N(N-1)/2$ pairs with the loop $i = 1, \cdots, N-1$ and the inside loop $j = i+1, \cdots, N$. However, the two particles in most of the pairs are more separated from each other than the interaction length so that they are negligible in the dynamics of the system. Clearly it is a waste of time to check these pairs.

In the minimum image convention, we introduce a cutoff length r_{cut} within which the interaction is active. When the relative distance $|\mathbf{r}_{ij}|$ between i-th particle and j-th particle is larger than r_{cut}, we check whether the following quantity is within the r_{cut} or not:

$$r_{ij} = \min\left[\sqrt{(x_{ij} + n_x R_{\text{cell}})^2 + (y_{ij} + n_y R_{\text{cell}})^2 + (z_{ij} + n_z R_{\text{cell}})^2}\right], \qquad (2.47)$$

where n_x, n_y, n_z assume the values $0, \pm 1$ and R_{cell} is the cell size. In this convention, the number of pairs we must calculate is restricted within the primitive cell, where the boundary condition is naturally introduced without taking the replica cells into account. As a result, we can save much computational time.

It is possible to reduce the computational time further by keeping a list of pairs. All interactions are expressed in terms of the relative distance $\Delta\mathbf{R}$ and the relative

momentum $\Delta \mathbf{P}$. Thus, it is possible to calculate the interactions in a single loop over the pairs instead of in the double loop over the $(N \times N)$ particles.

To evaluate the pairs, we introduce a definite length r_{out}, which is larger than r_{cut}. The point is that the list of pairs is not significantly changed during a few time steps as long as r_{out} is reasonably chosen. Once the list of pairs is calculated, the same list is used to calculate the force for next several steps before the updating of the list.

Notice that the actual efficiency depends on the computer hardware to be used. The method of the pair list is effective in the scalar computer but not in the vector computer. In the vector computer, it is better to use the triple loop over the $N \times N \times 27$ particles with replica cells because such structure of the loop is suitable to the architecture.

2.2 Metropolis method

The Metropolis method is a method to generate configurations of matter at fixed temperature and density, which are regarded as the canonical ensembles. In this study, the Metropolis method is used to prepare the initial state of the expanding matter model and to calculate the equation of state (EOS) of static nuclear matter.

2.2.1 Canonical ensemble

First, we remember the basic formula regarding the canonical ensemble, where the number of particle N, the volume of the system V and the temperature T are fixed. An expectation value of an observable $\mathcal{O}$ is calculated as follows:

$$\langle \mathcal{O} \rangle_{N,V,T} = \frac{\frac{1}{N!} \int \left(\frac{d\mathbf{r}d\mathbf{p}}{\hbar^6} \right)^N \exp \left[-\frac{H(\mathbf{r}^N, \mathbf{p}^N)}{k_B T} \right] \mathcal{O}(\mathbf{r}^N, \mathbf{p}^N)}{Z(N,V,T)}, \tag{2.48}$$

where k_B is the Boltzmann constant, $\mathbf{r}^N$ stands for the positions of N particles, $\mathbf{p}^N$ for the corresponding momenta and the partition function $Z(N,V,T)$ is given by:

$$Z(N,V,T) \equiv \frac{1}{N!} \int \left(\frac{d\mathbf{r}d\mathbf{p}}{\hbar^6} \right)^N \exp \left[-\frac{H(\mathbf{r}^N, \mathbf{p}^N)}{k_B T} \right]. \tag{2.49}$$

Notice that the Hamiltonian does not include the degrees of freedom for the spin and the isospin. In general, the integral should include these internal degrees of freedom but we will neglect them for simplicity.

In the case that the interaction does not include momentum dependent potentials, the partition function becomes simpler form:

$$Z(N,V,T) = \frac{1}{N! \Lambda(T)^{3N}} \int (d\mathbf{r})^N \exp \left[-\frac{V(\mathbf{r}^N)}{k_B T} \right], \tag{2.50}$$

where

$$\Lambda(T) = \left(\frac{\hbar^2}{2\pi M k_B T} \right)^{\frac{1}{2}}. \tag{2.51}$$

2.2.2 Algorithm of Metropolis method

In the procedure of the Metropolis method, the configuration of the system is modified step by step with evaluating the transition probability to go from one configuration to other configurations. In the canonical ensemble, the probability that the system has a configuration characterized by $(\mathbf{r}^N, \mathbf{p}^N)$ is given by:

$$\mathcal{N}(\mathbf{r}^N, \mathbf{p}^N) = \frac{\exp \left[-\frac{H(\mathbf{r}^N, \mathbf{p}^N)}{k_B T} \right]}{Z(N,V,T)}. \tag{2.52}$$

Let us to assume that the system has the configuration denoted by "o". Our task is to modify the configuration "o" to approach a specific equilibrated configuration

we want to obtain. The procedure is as follows. After the current configuration "o" is stored in the memory of the computer, a new configuration "n" is generated from the old configuration "o" based on the probability $\alpha(o \to n)$. This probability itself does not assure that the obtained new configuration is adequate for our demand. To check whether the new configuration should be accepted or not, the acceptance probability $\mathrm{acc}(o \to n)$ is introduced. That is, the transition probability is expressed as $\alpha(o \to n) \times \mathrm{acc}(o \to n)$.

We introduced, three unknown probabilities: $N(o)$, $\alpha(o \to n)$ and $\mathrm{acc}(o \to n)$. Now we will investigate the relations among these probabilities under the condition that the system is in thermal equilibrium. Consider the flow of configuration "o" to "n" as follows:

$$\kappa(o \to n) = \mathcal{N}(o) \times \alpha(o \to n) \times \mathrm{acc}(o \to n), \tag{2.53}$$

where $\mathcal{N}(o)$ is the probability of being in configuration "o", $\alpha(o \to n)$ is the probability of generating configuration "n", and $\mathrm{acc}(o \to n)$ is the probability of accepting this modification. In thermal equilibrium, we can assume that the above flow is equal to the reverse flow:

$$\kappa(o \to n) = \kappa(n \to o). \tag{2.54}$$

This condition is called as the detailed balance condition. Furthermore, it is possible to require that the way of generating configuration is symmetric:

$$\alpha(o \to n) = \alpha(n \to o). \tag{2.55}$$

Then, we obtain the following relation:

$$\frac{\mathrm{acc}(o \to n)}{\mathrm{acc}(n \to o)} = \frac{\mathcal{N}(n)}{\mathcal{N}(o)} = \exp\left[-\frac{U(n) - U(o)}{k_B T}\right]. \tag{2.56}$$

This relation indicates that we can determine whether the new configuration is accepted or not by evaluating $U(n) - U(o)$. There are several choices for $\mathrm{acc}(o \to n)$ to satisfy the above relation. In the Metropolis method, the following choice is used:

$$\mathrm{acc}(o \to n) = \begin{cases} \exp\left[-\frac{U(n) - U(o)}{k_B T}\right] & U(n) > U(o) \\ 1 & U(n) < U(o) \end{cases}. \tag{2.57}$$

This tells us how to proceed by modifying the system. When the energy of the new configuration is larger than that of the old configuration, the acceptance probablity is $0 < \mathrm{acc}(o \to n) < 1$. With a random number $0 < rand < 1$, we can check whether the new modification is accepted or not. Specifically, the new configuration is accepted when $rand < \mathrm{acc}(o \to n)$. On the other hand, for $U(n) < U(o)$, the new configuration is always accepted. In principle, many modifications to this acceptance probablility are possible to give the equilibrated configuration at the temperature T.

It should be noted that the above method is independent of $\alpha(o \to n)$, i.e., how to modify the configuration. In pactice, how to modify configurations are crucial in view of computational time. It is also important to estimate whether the obtained configuraion is really in thermal equilibrium or not. In the next subsection, we will discuss the actual procedure to obtain the cannonical ensembles of nuclear matter.

2.2.3 Canonical ensembles of nuclear matter

In the Metropolis method, nuclear matter is described in terms of $N = 200$ nucleons under periodic boundary conditions in the same way as was used in QMD. First of all, a temperature T and a density ρ are given as input parameters.

Initialization

We assign the initial positions, momenta, spins and isospins to the particles. The initial positions are distributed randomly in the cubic cell with a size $R_{\text{cell}} = \left(\frac{N}{\rho}\right)^{\frac{1}{3}}$. Using a random number $rand$ in the range $[0, 1]$, such a random distribution is given by:

$$
\begin{aligned}
R_x &= (rand - 0.5)R_{\text{cell}}, \\
R_y &= (rand - 0.5)R_{\text{cell}}, \\
R_z &= (rand - 0.5)R_{\text{cell}}.
\end{aligned}
\tag{2.58}
$$

However, we must avoid the situation where any two particles are too close to each other, in which case the Pauli potential energy may cause overflow. Thus we require additional condition that the distance of any two particles is larger than 0.1 fm.

For the momentum distribution, it is reasonalble to use the Fermi distribution for a given temperature as the initial distribution, in which case the corresponding chemical potential has to be calculated. In practice, it is not necessary to use the exact Fermi distribution for the initial configuration. Instead, we generate a random configuration inside the Fermi surface in the momentum space. The procedure is very similar to the case of the positional configuration:

$$
\begin{aligned}
P_x &= (1 - 2 * rand)P_{\text{F}}, \\
P_y &= (1 - 2 * rand)P_{\text{F}}, \\
P_z &= (1 - 2 * rand)P_{\text{F}},
\end{aligned}
\tag{2.59}
$$

where $P_{\text{F}} = \hbar c \left(\frac{3\pi^2 \rho}{2}\right)^{\frac{1}{3}}$ is the Fermi momentum. To ensure that the particles are inside the Fermi surface, we impose an additional condition that $\sqrt{P_x^2 + P_y^2 + P_z^2} < P_{\text{F}}$. The obtained momentum configuration is thought to be near to the ground state and the temperature T will be recovered in the Metropolis method.

Finally we comment on the spin and the isospin. These internal degrees of freedom are phenomenologically assigned to the particles. Each particle belongs to one of four kinds of attribute $p \uparrow, p \downarrow, n \uparrow, n \downarrow$, where p is the proton, n is the neutron, $\uparrow$ is the spin up and $\downarrow$ is the spin down. We assign these degrees of freedom to the particles sequentially in the same weight.

Modification

The modification of the configuration is carried out in two steps. First we generate a new configuration "n" from the old configuration "o", then check whether the new

configuration should be accepted or not by the acceptance probability, which is a function of the energy difference $U(n) - U(o)$. The original configuration is stored in case of rejecting the new configuration.

Now, we modify the configuration to calculate the new energy $U(n)$. The modification is carried out by changing the position and the momentum of a particle selected at random. Assuming that the i_{ran}-th particle is selected, its position and momentum are changed as follows:

$$
\begin{aligned}
R_\alpha(i_{\mathrm{ran}}) &\rightarrow R_\alpha(i_{\mathrm{ran}}) + (rand - 0.5)\Delta R, \\
P_\alpha(i_{\mathrm{ran}}) &\rightarrow P_\alpha(i_{\mathrm{ran}}) + (rand - 0.5)\Delta P,
\end{aligned} \tag{2.60}
$$

where $\alpha = x, y, z$, $\Delta R, \Delta P$ are constants and $rand$ is a random number in the region $[0, 1]$. The value of ΔR and ΔP should be determined so that the sequentially obtained configurations range over the whole configuration space.

For the positional configuration, $\Delta R = R_{\mathrm{cell}}$ is a reasonable choice. When a new position is over the boundary, the new position is shifted by $\pm R_{\mathrm{cell}}$ so that the particle is in the primitive cell.

On the other hand, ΔP should be set at the value which is larger than the corresponding value for the fluctuation of a given temperature T. It is safe to set $\Delta P \geq 10 P_{\mathrm{F}}$ even for $T = 30$ MeV. For lower temperatures, smaller value should be used because too large ΔP leads to too large system energy $U(n)$ which causes the very small acceptance probability resulting in the too long computational time.

With the new configuration, the energy of the new configuration $U(n)$ is calculated. When $U(n) < U(o)$, the new configuration is always accepted by difinition. When $U(n) > U(o)$, the acceptance probability $exp\left(-\frac{U(n)-U(o)}{k_B T}\right)$ is evaluated with a random number $rand$ in the range $[0, 1]$.

In case the new configuration is accepted, the initial configuration is updated, otherwise, the original configuration is reserved. Anyhow, at this stage, one Monte Carlo step is completed. Afterwards, a next particle is selected at random and the same procedure is carried out again. This loop should continue untill the detailed balance condition is fulfilled.

When should we stop the modification?

To obtain good statistics, it is necessary to extract many independent samples from the configurations obtained by Metropolis method. It is clear that sequential two configurations are almost the same because the configuration of all particles except one is the same. After the first sample is extracted, the second sample should be extracted from the configuration which is modified well enough to be independent of the first sample.

We can check whether the detailed balance condition is fulfilled or not by investigating the fluctuation of the total energy. In almost all cases, the total energy of the initial configuration is much larger than the energy adequate for a given temperature. Thus, in the course of the modification, the energy decreases gradually step by step and afterwards, fluctuates in a certain region. This fluctuation is the signature of the detailed balance.

Calculation of the energy

In practice, we do not need to calculate the total energy $U(n)$ at each time step because we have already known $U(o)$ at this stage. In other words, we need to calculate only the difference between $U(o)$ and $U(n)$. The total energy U is calculated as follows:

$$U = \sum_{i=1}^{N} \frac{p(i)^2}{2M} + \frac{1}{2} \sum_{i=1}^{N} \sum_{j \neq i} V_{\text{two}}(i,j) + V_{\text{density}}, \tag{2.61}$$

where $\frac{1}{2} \sum_{i=1}^{N} \sum_{j \neq i} V_{\text{two}}(i,j)$ indicates the total potential energy except for the density dependent potential V_{density}. Naively, one may think that $U(n) - U(o)$ can be calculated by the difference of the following single particle energy of the displaced particle $e(i_{\text{ran}})$:

$$e(i_{\text{ran}}) = \frac{p(i_{\text{ran}})^2}{2M} + \sum_{j \neq i_{\text{ran}}} V_{\text{two}}(i_{\text{ran}}, j) + \frac{1}{N} V_{\text{density}}. \tag{2.62}$$

Note that V_{density} cannot be split into N single particle energies because the sum over i and the sum over j are not symmetric as the expression $\sum_{i=1}^{N} \left(\sum_{j=1}^{N} \rho_{ij} \right)^{\tau}$ shows. It should also be noted that the single particle energy does not include the factor $1/2$ for compensating the double counting.

Now it is important to understand that $U(n) - U(o) \neq e(n) - e(o)$, where $e(o)$ and $e(n)$ mean the single particle energy for the configuration "o" and "n" respectively. Actually, $U(n) - U(o)$ is expressed by the difference of the following quantity:

$$\tilde{e}(i_{\text{ran}}) = \frac{p_{i_{\text{ran}}}^2}{2M} + \sum_{j \neq i_{\text{ran}}} V_{\text{two}}(i_{\text{ran}}, j) + V_{\text{density}}. \tag{2.63}$$

That is to say, it is inevitable to calculate the total energy for the density dependent potential.

Single particle energy distributions

Figure 2.7 shows the single particle energy distributions of the samples obtained by the Metropolis method. The single particle energy is calculated for each particle in the samples. The value of the vertical axis indicates the number of particles which belong to the energy regions divided by 1 MeV on the horizontal axis. The upper figure 2.7(a)(b) is the case of the saturation density $\rho = \rho_0$ and the lower figure 2.7(c)(d) is the case of $\rho = 0.05\rho_0$. The left hand side is the case $T = 5$ MeV and the right hand side is the case $T = 30$ MeV.

Each distribution consists of 1000 samples, each of which includes 200 particles. Namely, each distribution indicates the canonical ensemble composed of 200000 particles at a given temperature and density. The samples are picked up from the configurations generated by the Metropolis method after the detailed balance condition is fulfilled. It is necessary to pick up the samples in such a way that the obtained samples are statistically independent. To assure this, we do not pick up the next sample untill the old sample is modified $N = 200$ times.
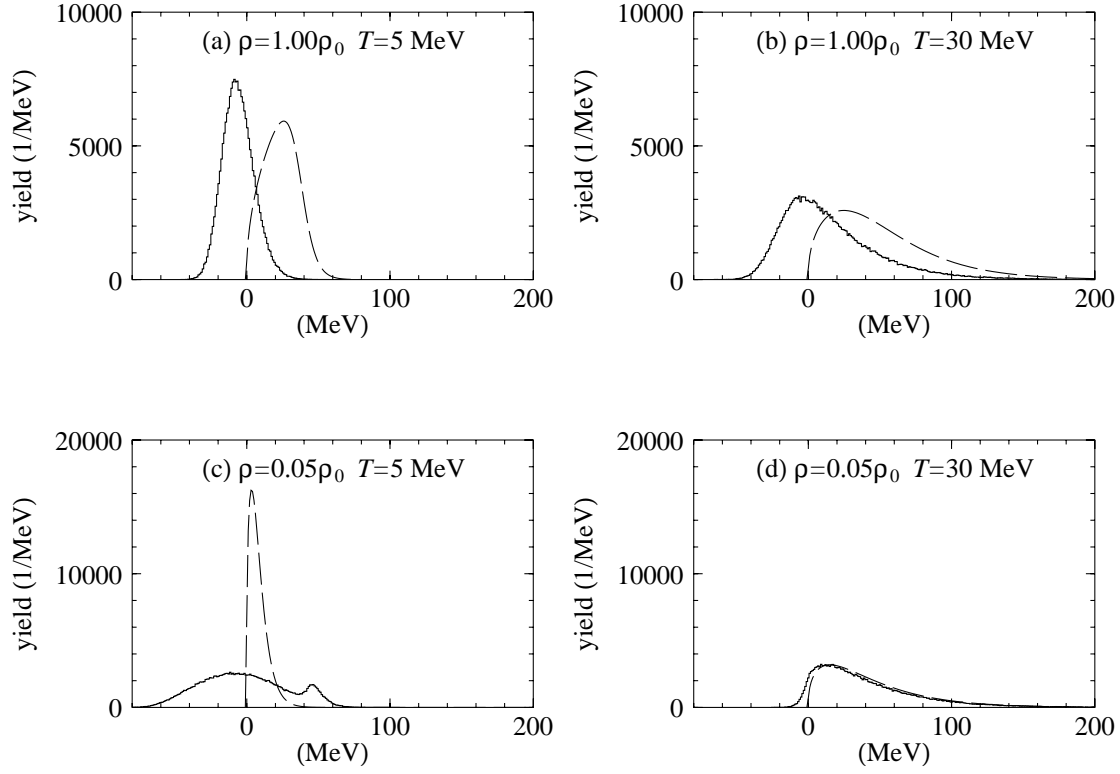
25

Figure 2.7: Single particle energy distribution over 1000 samples: (a) $\rho = 1.00\rho_0$, $T = 5$ MeV. (b) $\rho = 1.00\rho_0$, $T = 30$ MeV. (c) $\rho = 0.05\rho_0$, $T = 5$ MeV. (d) $\rho = 0.05\rho_0$, $T = 30$ MeV. The abscissa is the single particle energy and the ordinate is the number of particle per 1 MeV. There are 200000 particles because one sample consists of 200 particles. Dashed line refers to the Fermi distribution multiplied by the density of state.

In each figure, corresponding Fermi-Dirac distribution $f(E)$ multiplied by the density of state $D(E)$ is also depicted (dashed line):

$$D(E)f(E) = 1000N \frac{\sqrt{E}}{\pi^2 \rho} \left(\frac{2M}{\hbar^2}\right)^{\frac{3}{2}} \frac{1}{1 + \exp\left(\frac{E-\mu}{T}\right)}, \tag{2.64}$$

where M is the nucleon mass and μ is the chemical potential. The chemical potential is determined by:

$$\int_0^\infty f(E)D(E)dE = 1000N. \tag{2.65}$$

Consider the case (a)(b) of $\rho = \rho_0$, which is used as the initial state of expanding matter. At the saturation density, the particle is under the influence of the attractive interaction so that the obtained distribution is shifted in the negative energy direction as compared to the Fermi-Dirac distribution. Apart from this difference, the shape of the obtained distribution is similar to that of the Fermi-Dirac distribution.

On the other hand, the case (c)(d) is the distributions at low density $\rho = 0.05\rho_0$. In this case, it is expected that the calculated distribution is close to the Fermi-Dirac distribution because the particles behave like free particles at low density. Nevertheless, the case (c) of $T = 5$ MeV shows that the obtained distribution deviates significantly from the Fermi-Dirac distribution. This is because some fragments appear in the samples at $T = 5$ MeV. As this example shows, the local density fluctuation is allowed in the framework of the Metropolis method.

For the case (d) of $T = 30$ MeV, the system is clearly outside the coexistent region and the particles are effectively free. As a result, the obtained distribution is in good agreement with the Fermi-Dirac distribution. In this case, the system is thought to be classical and the Fermi distribution reduces to the Boltzmann distribution.
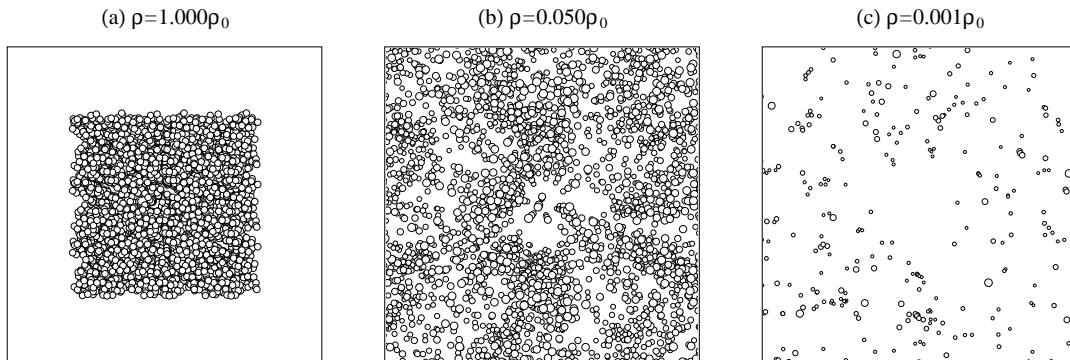
Figure 2.8: Snapshots of expanding nuclear matter at different densities. (a) an initial state with $\rho = \rho_0$. (b) an intermediate state at $\rho = 0.05\rho_0$ during the expansion. (c) a final state with $\rho = 0.001\rho_0$. (a) shows not only the primitive cell but also 26 replica cells used in periodic boundary conditions. Although it looks like a finite system, it is a part of an infinite system.

2.3   Expanding matter model

The expanding matter model simulates the matter which expands at a fixed rate, where the time evolution of matter is calculated by Molecular Dynamics under generalized periodic boundary conditions. The generalized periodic boundary conditions allow us to investigate the dynamics of expanding matter free from any finite size effects. We apply this model to nuclear matter with the QMD in order to investigate how the expanding motion affects the nuclear phase transition, which is examined experimentally in heavy ion reactions with large radial flow.

2.3.1   Overview

Now, we will explain how the model works in terms of the classical Molecular Dynamics, in which the position $\mathbf{r}$ and the velocity $\mathbf{v}$ are basic quantities.

First, we prepare the thermally equilibrated matter at saturation density by the Metropolis method. Based on the procedure in the previous section, 1000 samples at a given temperature T_{ini} are generated. The obtained matter has thermal motion resulting from a given temperature but such a thermal motion cannot cause the system to expand. This is because the particles cannot escape from the cell at a fixed density.

To let the whole system expand, it is necessary that the cubic cell expands so that the average density can decrease. We assume that the average density decreases as follows:

$$\rho(t) = \frac{N}{R_{\mathrm{cell}}(t)^3} = \frac{\rho(0)}{(1 + ht)^3}, \tag{2.66}$$

where t is the time, R_{cell} is the cell size and h is the parameter, which controls the

speed of expansion. This constraint determines the macroscopic constraint of the system. The cell size $R_{\mathrm{cell}}(t)$ increases in such a way that it is proportional to time t.

In microscopic point of view, the particle is considered to have the following velocity:

$$\mathbf{v}(t) = \mathbf{v}_{\mathrm{local}}(t) + h\mathbf{r}(0). \qquad (2.67)$$

The above velocity consists of the local velocity and the collective velocity. When $t = 0$, the local velocity is $\mathbf{v}_{\mathrm{local}}(0)$, which is given by the Metropolis method. The system cannot expand only with $\mathbf{v}_{\mathrm{local}}(0)$ and therefore, the collective velocity $h\mathbf{r}(0)$ is also given at $t = 0$, which is consistent with the way the density decreases as given by Eq. (2.66). The collective velocity is proportional to the initial position of the particle $\mathbf{r}(0)$. Forcing all particles have collective velocities which is proportional to the initial position, we find that the whole system expands homogeneously at a fixed rate characterized by the parameter h. This is because any two particles have the relative collective velocity which is proportional to their relative distance.

The time evolution of expanding matter proceeds according to the equations of motion. At each time step, we need to evaluate the relative distance between two particles for calculating the force in the equation of motion. The force is calculated only when the distance Δr is smaller than the cutoff length r_{cut}. If Δr is larger than r_{cut}, we check whether the following modified distance is within r_{cut}:

$$\Delta r_\alpha(t) \to \Delta r_\alpha(t) \pm R_{\mathrm{cell}}(t), \qquad (2.68)$$

where $\alpha = x, y, z$. This procedure is same as normal periodic boundary conditions except that the cell length depends on the time. Under the generalized periodic boundary conditions, the following procedure is additionally assumed:

$$\Delta v_\alpha(t) \to \Delta v_\alpha(t) \pm h R_{\mathrm{cell}}(0). \qquad (2.69)$$

Notice that $R_{\mathrm{cell}}(0)$ is used instead of $R_{\mathrm{cell}}(t)$. This procedure is valid because the relative collective velocity of the two particles separated by $R_{\mathrm{cell}}(t)$ is $h R_{\mathrm{cell}}(0)$ at $t = 0$ and this velocity is assumed to be conserved. These procedures also applies when the particle is over the boundary. Actually, particles seldom go over the boundary because the speed of the boundary is always higher than particles inside the cell as long as thermal motions do not boost particles significantly.

As time evolution proceeds, the density of the system decreases and the system becomes unstable with decreasing its effective temperature. The effective temperature is proportional to the kinetic energy composed of the thermal component of the velocity. The instability of the system causes the density fluctuation and results in the fragmentation. One of our purpose is to investigate how the system becomes unstable and how the density fluctuation grows during the expansion process which depends on both the initial temperature and the expansion velocity given at the beginning.

The time evolution continues untill the density of the system reaches $\rho = 0.001\rho_0$ where fragments can be unambiguously identified. At this stage, we obtain several fragments in the primitive cell. Using 1000 samples prepared by the Metropolis

method, we can obtain the fragment mass distribution composed of 200000 particles for a given temperature and a given expanding speed h. To investigate how the expanding motion and the temperature affect the final fragment mass distribution is another purpose of this study.

2.3.2 QMD under generalized periodic boundary conditions

In the case of the QMD, the momentum is the basic quantity rather than the velocity. Therefore, the discussion of previous subsection is a little modified. The average density of the system is given by:

$$\rho(t) = \frac{N}{R_{\text{cell}}(t)^3} = \frac{\rho(0)}{\left(1 + h\frac{P_{\text{F}}t}{M\rho_0^{-\frac{1}{3}}}\right)^3}, \tag{2.70}$$

where M is the nucleon mass, ρ_0 is the saturation density and P_{F} is the Fermi momentum. Notice that the parameter h is non-dimension and $\rho_0^{-\frac{1}{3}} = 1.81$ fm is introduced as the scale of the distance. The momentum of the particle is expressed as follows:

$$\mathbf{P}_i(t) = \mathbf{P}_{i,\text{local}}(t) + h\frac{\mathbf{R}_i(0)}{\rho_0^{-\frac{1}{3}}}P_{\text{F}}. \tag{2.71}$$

In this way, the Fermi momentum is the scale of the momentum and $\rho_0^{-\frac{1}{3}}$ is the scale of the distance.

Consider the relation between the particle in the primitive cell and the particle in the replica cell. The replica cell is located at $\mathbf{R}_{\text{cell}}(t)$ from the origin of the primitive cell. The velocity of the replica cell $\mathbf{V}_{\text{cell}}$ is given by:

$$M\mathbf{V}_{\text{cell}} = h\frac{\mathbf{R}_{\text{cell}}(0)}{\rho_0^{-\frac{1}{3}}}P_{\text{F}}. \tag{2.72}$$

The position of the particle in the replica cell is deduced from the position of the particle in the primitive cell as follows:

$$\mathbf{R}_i(t) \rightarrow \mathbf{R}_i(t) + \mathbf{R}_{\text{cell}}(t). \tag{2.73}$$

Now, what is the momentum of the particle in the replica cell? It is given by:

$$\mathbf{P}_i(t) \rightarrow \mathbf{P}_i(t) + h\frac{\mathbf{R}_{\text{cell}}(0)}{\rho_0^{-\frac{1}{3}}}P_{\text{F}} = \mathbf{P}_{i,\text{local}}(t) + h\frac{\mathbf{R}_i(0) + \mathbf{R}_{\text{cell}}(0)}{\rho_0^{-\frac{1}{3}}}P_{\text{F}}. \tag{2.74}$$

In this way, it is found that the collective momentum in the replica cell obeys the same rule that the collective momentum is proportional to the corresponding distance. Figure 2.9 illustrates the relation between particle position and its collective momentum.
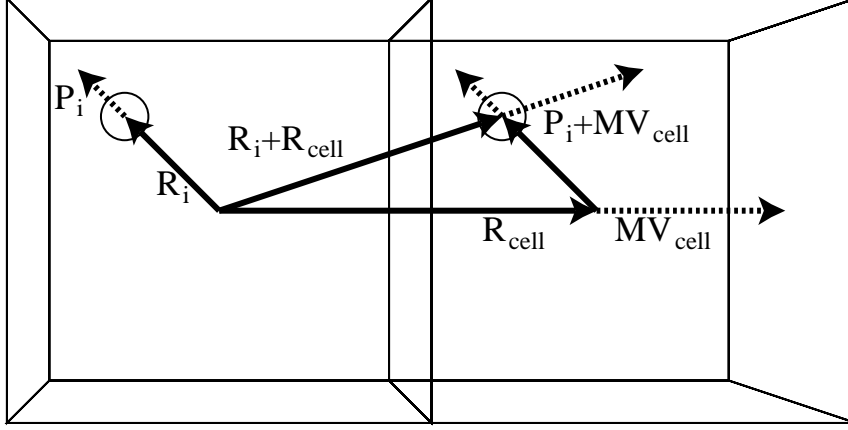
Figure 2.9: The relation between particle position and its collective momentum. The left hand side is the primitive cell and the right hand side is a replica cell.

2.3.3 Characteristic of infinite expanding system

In the framework of the expanding matter model, the speed of expansion is conserved during the time evolution. This means that an external force exists and it controls the system so that the system expands at a fixed rate. As a result, the energy conservation is violated during the time evolution as opposed to simulations of finite systems.

For the thermalized finite system, the system expands due to the thermal motion characterized by the temperature. Such a system expands with decreasing the temperature and as a result, the speed of expansion also decreases. Differently from this situation, for infinite expanding matter, the system expands constantly regardless of the thermal motion. When the thermal motion overcomes the expanding motion given by h, the total energy decreases because the thermal motion is suppressed by the slow expansion. On the other hand, when the system is forced to expand rapidly in spite of low temperature, the system gains the energy during the expansion.

Figure 2.10 shows the dependence of energy on a mean nearest-neighbor distance for $T_{ini} = 5$ MeV and $T_{ini} = 30$ MeV with $h = 0.1$. The case of $h = 0.5$ is almost the same as $h = 0.1$ except for the fact that the error bars become larger as h increases. However, when $h = 0.1$ or $h = 2.0$, the energy decreases even with $T_{ini} = 5$ MeV.
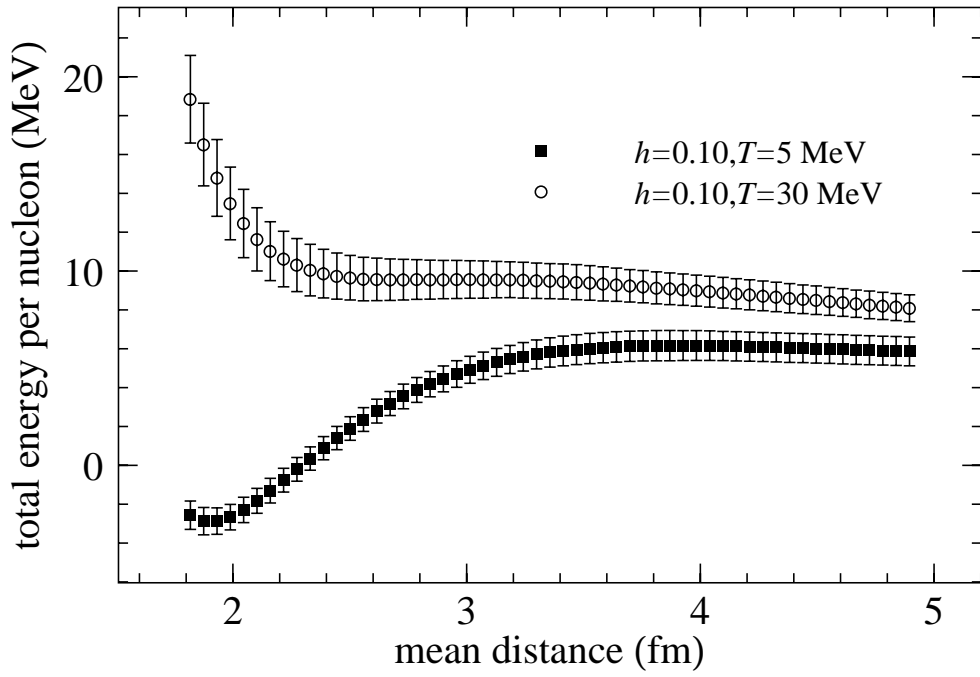
Figure 2.10: The dependence of energy on the mean nearest neighbor distance for the initial temperature $T_{\mathrm{init}} = 5$ and 30 MeV with $h = 0.10$.

Chapter 3

Instability of expanding matter

In this chapter, the instability of nuclear matter is investigated based on molecular simulation discussed in the previous chapter. The molecular simulation illustrates the property of nuclear matter as composite of nucleons, where the instability of nuclear matter leads to nuclear fragmentation.

The instability appears in both static and dynamic nuclear matter. Static nuclear matter is characterized by the equation of state (EOS), which can be calculated by the Metropolis method. On the other hand, dynamical aspects of nuclear matter can be investigated by the expanding matter model, where the pressure and the effective temperature are calculated at each time step during time evolution. These instantaneous quantities can be compared with the EOS obtained by the Metropolis method because the small h limit of expanding matter approaches to static nuclear matter. In this way, both static and dynamic properties can be discussed in the same framework.

Using the Lennard-Jones potential instead of complicated QMD potentials, it is possible to simulate very slow expanding matter which can be regarded as quasi-static. Introducing an inhomogeneity function, we will investigate how the expanding motion affects the liquid-gas phase transition as compared to the coexistent region, which can be exactly calculated by the Gibbs ensemble method.

3.1   EOS of nuclear matter

In this section, we calculate the EOS of nuclear matter by the Metropolis method to know the static property of nuclear matter. For given temperature and density (T, ρ), the Metropolis method provides us with the canonical ensembles of nuclear matter, from which 100 independent samples are extracted. Each sample includes 200 nucleons so that 100 samples give nuclear matter composed of 20000 particles. Averaging these samples, the energy and the pressure for given (T, ρ) are obtained.

3.1.1   Density dependence of the energy

Figure 3.1 shows the data points of the total energy per particle plotted in the density-energy plane. Temperatures are $3, 8, 10, 15, 20, 30$ MeV and the density
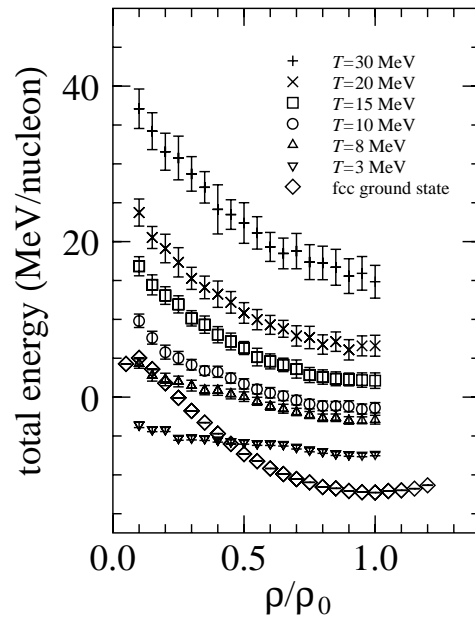
Figure 3.1: The density dependence of energy per particle in static nuclear matter. Each data point is an average over 100 samples calculated independently by the Metropolis method for given (ρ, T). Except for "fcc ground state", nucleon are allowed to form fragments.
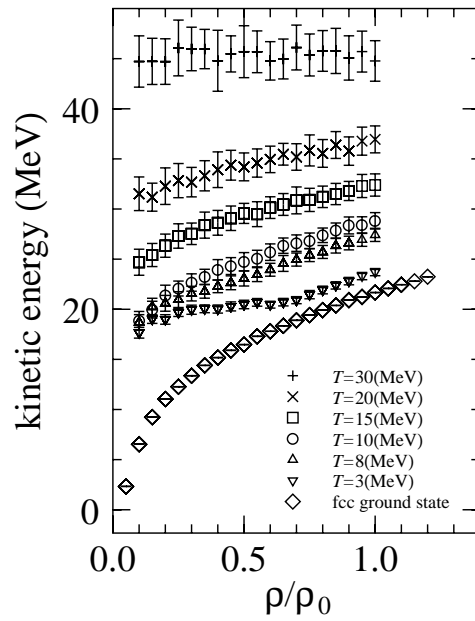

Figure 3.2: The density dependence of kinetic energy per particle in static nuclear matter.

ranges from $0.05\rho_0$ to ρ_0 by increment of $0.05\rho_0$. A set of data with a fixed temperature forms an isotherm. The "fcc ground state" indicates the ground state energy for the configuration that the positions of particles are fixed on the face-centered cubic (fcc) lattice.

First of all, it should be noted that fragments may appear in the samples obtained by the Metropolis method. This means that the resultant EOS is not necessarily that of the homogeneous matter. When the selected (ρ, T) belongs to unstable regions, fragments are likely to appear in the corresponding samples. In this sense, our EOS based on the Metropolis method is different from usual EOS diagrams. To clarify this point, the "fcc ground state" is also depicted, where the homogeneity of the system is maintained.

As shown in Fig. 3.1, the line for "fcc ground state" has a parabolic shape, which is expected around the saturation density. It should be noted that the energy of low density matter is positive for "fcc ground state". This is because the matter behaves like free Fermi gas in low density region due to the Pauli potential. On the other hand, the isotherm for $T = 3$ MeV is significantly different from the parabolic shape despite $T = 3$ MeV is still near to the ground state. We see that the energy for $T = 3$ MeV is constant at -5 MeV in the region $0.3\rho_0 < \rho < 0.7\rho_0$. This is due to the fact that fragmentation occurred in the matter at $T = 3$ MeV. The energy of -5 MeV is considered to be the sum of the binding energy of a fragment and its kinetic energy par particle.

In the next subsection, we will see that the $T = 8$ MeV is the critical temperature. Thus, the data points for $T < 8$ MeV can fall on the spinodal region, in which case fragments can appear in the samples so that the corresponding isotherm deviates from a palaboric shape. On the other hand, for $T > 8$ MeV we see that the isotherm approaches a palaboric shape as the temperature increases. The isotherm for $T = 30$ MeV shows almost the same density dependence as the "fcc ground state".

This is because the matter is homogeneous and the kinetic energy per particle is independent of density in the classical limit. That is to say, the density dependence of the energy for $T = 30$ MeV is due to the density dependence of the potential energy for homogeneous matter. Figure 3.2 shows the density dependence of kinetic energy. We see that the kinetic energy for $T = 30$ MeV is constant around $\frac{3}{2}T = 45$ MeV, which indicates that the matter is in a classical limit.

It is found that the kinetic energy of "fcc ground state" is similar to that of free Fermi gas, which is mentioned in the parameter fitting of the Pauli potential. Figure 3.2 together with Fig. 3.1 shows how the momentum dependent potential affects the matter at a given temperature.

3.1.2 Density dependence of the pressure

Next, we study the pressure against density, which enables us to analyze the unstable region of the system. The pressure is calculated using the virial equation as follows:

$$P = \frac{\rho}{3N} \left(\mathbf{P}_i \cdot \frac{\partial H}{\partial \mathbf{P}_i} - \sum_{i=1}^{N-1} \sum_{j=i+1}^{N} (\mathbf{R}_i - \mathbf{R}_j) \cdot \frac{\partial H}{\partial \mathbf{R}_i} \right). \tag{3.1}$$

Notice that the kinetic part of the pressure includes $\mathbf{P}_i \cdot \frac{\partial H}{\partial \mathbf{P}_i}$ instead of $\mathbf{P}_i \cdot \mathbf{P}_i$, where $\frac{\partial H}{\partial \mathbf{P}_i}$ indicates the velocity in the equations of motion. This difference is very important in the model with the momentum-dependent potential.

Figure 3.3 shows the dependence of pressure on density for the same temperatures used in Fig. 3.1. The "fcc ground state" is also depicted. The isothermal spinodal region is defined by the condition $\left(\frac{\partial P}{\partial \rho}\right)_T < 0$, where the system is unstable. The critical temperature T_c under which isothermal spinodal region appears is determined as the temperature at which the local minimum of the density-pressure curve disappears. We calculate the density-pressure curve for each temperature by 1 MeV step and find that $T_c = 8$ MeV. We can see in this figure that local minimum disappears for $T > 8$ MeV.

Now it should be reminded that our procedure allows that particles form fragments when the system is unstable. This means that the instability is suppressed by fragmentation which is allowed in our approach. In fact, this is the reason why $T_c = 8$ MeV is smaller than typical values (~ 15 MeV [34]) predicted by models based on plane wave using similar interactions. Traditional models explicitly assume continuous matter, which has higher critical temperature and wider spinodal region. The pressure of "fcc ground state" simulates the continuous matter. The larger negative pressure region is caused by the constraint that the particles cannot form fragments. This negative pressure region is thought to belong to coexistent regions, inside which the pressure is expected to be constant and equal to the saturated vapor pressure. The saturated vapor pressure is always positive. If the particles can form fragments, the pressure is thought to approach the positive pressure.

Nevertheless, it is found that the pressure for $T = 3$ MeV has negative value around $\rho = 0.7\rho_0$ despite the fact that fragmentation is allowed. This is because the interfaces between fragment (liquid) and gas play a dominant role in the system which includes only $N = 200$ particles. In principle, percentages of particles in interfaces is negligible in real infinite matter. However, in the small system, percentages of particles which belong to interfaces are essential and contribute to the negative pressure. To investigate the coexistent state exactly, we need a different technique called Gibbs ensemble method. However, the Gibbs ensemble method with QMD interaction is a future work. The Gibbs ensemble method with the Lennard-Jones potential will be introduced in the later section.

3.2 Instability of expanding matter

In this section, the expanding matter model is utilized to investigate how the expanding motion affects the instability of nuclear matter. The instability is investigated by the pressure calculated in the course of the time evolution, which is compared with the isotherms obtained from the Metropolis method. The pressure is usually obtained from the virial equation but it should be noted that expanding matter is not in thermal equilibrium. The virial equation is often derived with the help of the ergodic theorem, which states that a time average is equivalent to an ensemble average. In this case, it is assumed that a time average is performed at a fixed density.
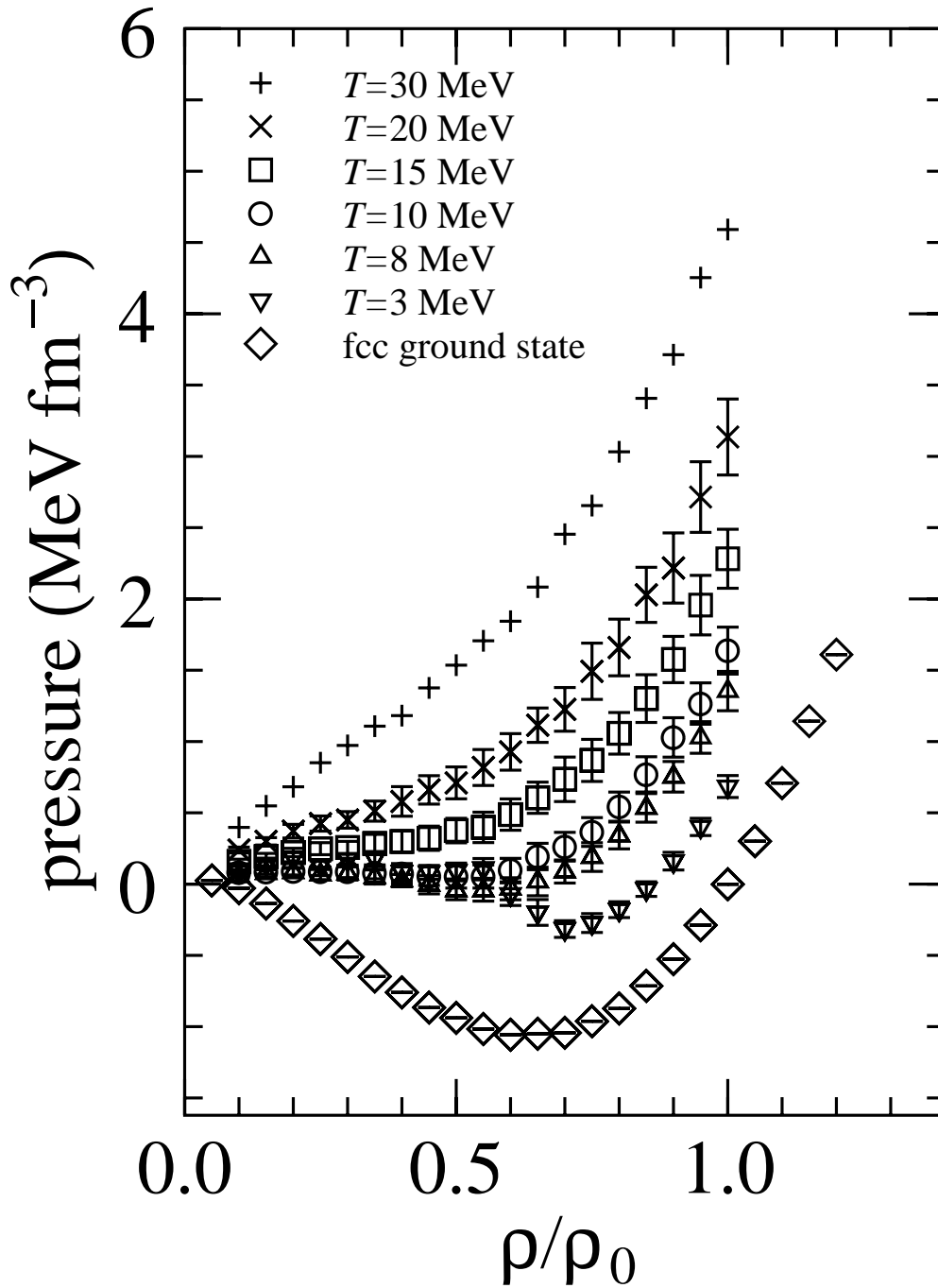
Figure 3.3: The density dependence of pressure in static nuclear matter. The pressure is calculated on the basis of the virial equation. Each data point for (ρ, T) corresponds to that of Fig. 3.1

To apply the virial equation to expanding matter, it is necessary to confirm that the virial equation works for the instantaneous pressure during the time evolution of expanding matter [35].

3.2.1 Virial equation for the instantaneous pressure

Consider the pressure in the cubic cell with the length R_{cell}, where N particles are distributed at random. The following derivation is based on the fact that the pressure is regarded as the momentum flux which pass through an unit area in a space. The momentum flux is composed of two kinds of sources. One is the momentum of each particle and the other is the forces on particles. First, we estimate the contribution of the momentum of particles. Given a unit area $dydz$ located at an arbitrary position in the cell, the probability that i-th particle pass through the area $dydz$ is given by

$$\left(\frac{v_x(i)dt}{R_{\text{cell}}}\right)\left(\frac{dydz}{R_{\text{cell}}R_{\text{cell}}}\right) = v_x(i)\frac{dtdydz}{R_{\text{cell}}R_{\text{cell}}R_{\text{cell}}}, \tag{3.2}$$

where $v_x(i)$ is the x component of the i-th velocity and dt is an unit time. Statistically the xx component of the momentum flux is estimated as the product of $\frac{p_x(i)}{dtdydz}$ and the above probability:

$$P_{\text{kin}}^{xx}(i) = p_x(i)v_x(i)\frac{1}{R_{\text{cell}}R_{\text{cell}}R_{\text{cell}}}. \tag{3.3}$$

The above discussion is valid for any component of any particle. Assuming

$$\sum_{i=1}^{N} P_{\text{kin}}^{xx}(i) = \sum_{i=1}^{N} P_{\text{kin}}^{yy}(i) = \sum_{i=1}^{N} P_{\text{kin}}^{zz}(i) \equiv P_{\text{kin}}, \tag{3.4}$$

P_{kin} is expressed as follows:

$$P_{\text{kin}} = \frac{1}{3R_{\text{cell}}R_{\text{cell}}R_{\text{cell}}} \sum_{i=1}^{N} \mathbf{p}(i) \cdot \mathbf{v}(i). \tag{3.5}$$

Notice that we distinguish between $\mathbf{p}(i)$ and $\mathbf{v}(i)$ on purpose because $\mathbf{p}(i)$ is not proportional to $\mathbf{v}(i)$ in the model where momentum dependent potentials are used.

Next, we estimate the contribution of the forces. Defining x_{ij} as the x component of the distance vector between the two particles i and j, the probability that x_{ij} traverses the area $dydz$ is as follows:

$$\left(\frac{x_{ij}}{R_{\text{cell}}}\right)\left(\frac{dydz}{R_{\text{cell}}R_{\text{cell}}}\right) = \frac{x_{ij}dydz}{R_{\text{cell}}R_{\text{cell}}R_{\text{cell}}}. \tag{3.6}$$

The momentum carried by the force $F_x(i,j)$ during the unit time is $F_x(i,j)dt$. Thus, the corresponding momentum flux is expressed as follows:

$$P_{\text{force}}^{xx}(i,j) = \frac{F_x(i,j)dt}{dydzdt}\frac{x_{ij}dydz}{R_{\text{cell}}R_{\text{cell}}R_{\text{cell}}} = \frac{x_{ij}F_x(i,j)}{R_{\text{cell}}R_{\text{cell}}R_{\text{cell}}}. \tag{3.7}$$

The other components can be similarly derived. Now we assume the following equality:

$$\sum_{i=1}^{N-1} \sum_{j=i+1}^{N} P_{\text{force}}^{xx}(i,j) = \sum_{i=1}^{N-1} \sum_{j=i+1}^{N} P_{\text{force}}^{yy}(i,j) = \sum_{i=1}^{N-1} \sum_{j=i+1}^{N} P_{\text{force}}^{zz}(i,j) \equiv P_{\text{force}}. \qquad (3.8)$$

Then, P_{force} is obtained by

$$P_{\text{force}} = \frac{1}{3 R_{\text{cell}} R_{\text{cell}} R_{\text{cell}}} \sum_{i=1}^{N-1} \sum_{j=i+1}^{N} \mathbf{r}_{ij} \cdot \mathbf{F}_{ij}. \qquad (3.9)$$

Summing P_{kin} and P_{force}, the total pressure is given in the the following form:

$$\begin{aligned}
P &= \frac{1}{3 R_{\text{cell}} R_{\text{cell}} R_{\text{cell}}} \left[\sum_{i=1}^{N} \mathbf{p}(i) \cdot \mathbf{v}(i) + \sum_{i=1}^{N-1} \sum_{j=i+1}^{N} \mathbf{r}_{ij} \cdot \mathbf{F}_{ij} \right] \\
&= \frac{\rho}{3N} \left[\sum_{i=1}^{N} \mathbf{p}(i) \cdot \mathbf{v}(i) + \sum_{i=1}^{N-1} \sum_{j=i+1}^{N} \mathbf{r}_{ij} \cdot \mathbf{F}_{ij} \right],
\end{aligned} \qquad (3.10)$$

where $\rho = \frac{N}{R_{\text{cell}} R_{\text{cell}} R_{\text{cell}}}$ is used. In the above discussion, time-average is not invoked but statistical concept is significant throughout the derivation. To obtain the pressure under a certain condition, we need a lot of samples which correspond to the specific condition.

3.2.2 Expanding nuclear matter

Since we understand the instantaneous pressure expression, we can use the virial equation in the expanding matter model. However, when applying the virial equation to the expanding matter model, we should take into account the effect of collective motion appropriately. It is assumed that the system expands at a specific rate in the expanding matter model. Thus, we extract the local momentum from the total momentum and use only the local momentum in the virial equation. The local momentum is expressed as follows:

$$\mathbf{P}_{i,\text{local}}(t) = \mathbf{P}_i(t) - h \frac{\mathbf{R}_i(t)}{\rho(t)^{-\frac{1}{3}}} P_{\text{F}}, \qquad (3.11)$$

where the second term is the collective component, which depends on time but notice that

$$h \frac{\mathbf{R}_i(t)}{\rho(t)^{-\frac{1}{3}}} P_{\text{F}} \sim h \frac{\mathbf{R}_i(0)}{\rho_0^{-\frac{1}{3}}} P_{\text{F}}. \qquad (3.12)$$

In this case, Eq. (3.11) is the same as Eq. (2.71). All potentials used in the QMD are represented in terms of the relative distance and the relative momentum. Using the QMD potentials, the virial equation is expressed as follows:

$$P = \rho T_{\text{eff}} + \frac{\rho}{3N} \sum_{i=1}^{N-1} \sum_{j=i+1}^{N} (\mathbf{R}_i - \mathbf{R}_j) \cdot \left[-\frac{\partial}{\partial \mathbf{R}_i} U(\mathbf{R}_i - \mathbf{R}_j, \mathbf{P}_i - \mathbf{P}_j) \right], \qquad (3.13)$$

$$\frac{3}{2}T_{\text{eff}} = \frac{1}{N} \sum_{i=1}^{N} \frac{\mathbf{P}_{i,\text{local}}}{2} \cdot \left(\frac{\partial H}{\partial \mathbf{P}_i}\right)_{\text{local}}, \tag{3.14}$$

$$\left(\frac{\partial H}{\partial \mathbf{P}_i}\right)_{\text{local}} = \frac{\mathbf{P}_{i,\text{local}}}{M} + \sum_{j \neq i} \frac{\partial}{\partial \mathbf{P}_i} U(\mathbf{R}_i - \mathbf{R}_j, \mathbf{P}_i - \mathbf{P}_j), \tag{3.15}$$

where U is the total potential and T_{eff} is an effective temperature expressed in terms of the local momentum. Notice that the derivative of the potential with respect to the momentum is also calculated with the local momentum.

Figure 3.4 shows the pressure and the effective temperature calculated by the above virial equation during the time evolution of expanding matter. The speed of expansion is set at $h = 0.1$, which is the minimum in the QMD expanding matter because slower expansion demands very long computational time. The time unit dt is set such that $hdt = 0.02$. The smooth lines in the upper figures (a)(b)(c) indicate the pressures calculated during expansions and the lower figures (d)(e)(f) show the corresponding effective temperatures respectively. The initial temperatures are set at $T_{\text{ini}} = 30$ MeV in (a)(d), $T_{\text{ini}} = 15$ MeV in (b)(e) and $T_{\text{ini}} = 5$ MeV in (c)(f), each of which is compared with the isotherm with the same temperature. These isotherms are the same as those in Fig. 3.3, where each data point is calculated independently by the Metropolis method.

Let us evaluate the kinetic energy resulting from the expansion with $h = 0.1$. The expanding energy per particle of a sphere with a radius l fm at $\rho_0 = 0.168$ fm^{-3} is estimated as follows:

$$\frac{1}{N} \int_0^l 4\pi R^2 dR \rho_0 \frac{1}{2M} \left(h \frac{R}{\rho_0^{-\frac{1}{3}}} P_{\text{F}}\right)^2 = \frac{3}{5} \left(\frac{l}{1.81}\right)^2 37.6 h^2 \text{ MeV}, \tag{3.16}$$

where N is the number of particles and the Fermi energy $\frac{P_{\text{F}}^2}{2M} = 37.6$ MeV. The typical value of l should be set based on the range of the potentials used in the model. In the case of the QMD potential, the effective range is estimated within 5 fm. When $l = 5$ fm and $h = 0.1$, the expanding energy per particle is 1.72 MeV. Thus, the expanding energy per particle for $h = 0.1$ is smaller than the initial temperatures.

The pressure of expanding matter is calculated successively during time evolution. This means that the data points on the density-pressure curve are connected by the equations of motion. Once the density fluctuation occurs at a certain density, it affects later stages at lower density. Such grow of fluctuation is considered to depend on both the speed of expansion and the temperature.

As shown in the Fig. 3.4, for all the initial temperatures, the pressure of expanding matter with $h = 0.1$ is below the isotherm in all density region except ρ_0, where both pressures agree. This is because T_{eff} decreases with decreasing density.

For $T_{\text{ini}} = 30$ MeV, the pressure and T_{eff} decrease with decreasing density untill the density reaches $0.3\rho_0$ where T_{eff} is around 8 MeV, which is equal to the critical temperature T_c for static nuclear matter. We can say that the matter is considered to be stable against fragmentation at least for $T_{\text{eff}} > T_c$ because fragmentation cannot occur. We see that the pressure is zero for $\rho < 0.3\rho_0$, while $T_{\text{eff}} > 4$ MeV holds in
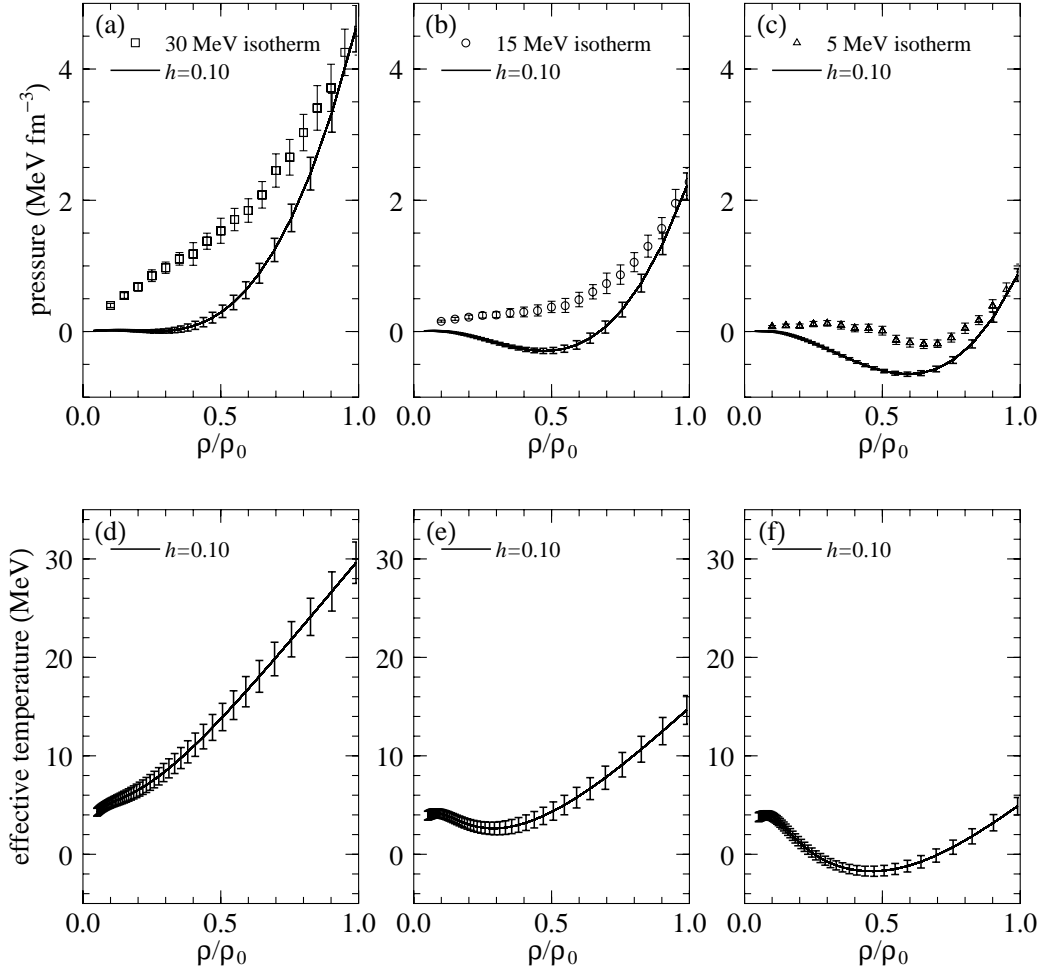
40

Figure 3.4: The density dependence of both pressure (upper part) and effective temperature (lower part). Figures (a) and (d) have the same initial temperature $T_{\text{init}} = 30$ MeV. Similarly, figures (b) and (e) have $T_{\text{init}} = 15$ MeV. (c) and (f) have $T_{\text{init}} = 5$ MeV. Smooth lines are the mean value of the results of expanding nuclear matter, and various symbols in (a), (b) and (c) are obtained by the Metropolis method in static nuclear matter.

the same region. This means that the attractive force works in this region because T_{eff} contributes to the positive pressure. Therefore, fragmentation is considered to start from $\rho = 0.3\rho_0$

For $T_{\mathrm{ini}} = 15$ MeV, the pressure decreases with decreasing density and reaches zero around $\rho = 0.7\rho_0$, where $T_{\mathrm{eff}} = 8$ MeV holds again. In this case, the pressure decreases further and reaches -0.3 MeV fm^{-3} around $\rho = 0.5\rho_0$. The density-pressure curve is similar to the case of "fcc ground state". This is because the matter maintains its homogeneity due to the collective motion. In the case of expanding matter, the positions of the particles are not fixed like fcc lattice but it is a strong constraint that the matter expands at a fixed rate. The spinodal region $\frac{\partial P}{\partial \rho} < 0$ is found in the region $\rho < 0.5\rho_0$, where fragmentation is expected to occur. Notice that T_{eff} starts to increase around $\rho = 0.3\rho_0$, where fragmentation may start since it means the increase of the local temperature. However, it is not certain that this increase of T_{eff} indicates the fragmentation because T_{eff} is affected by the momentum dependent forces.

For $T_{\mathrm{ini}} = 5$ MeV, the matter is below $T_c = 8$ MeV from the beginning. We see that the pressure decreases with decreasing density and reaches zero around $\rho < 0.85\rho_0$ and afterwards decreases further and reaches -0.7 MeV fm $^{-3}$ around $\rho = 0.6\rho_0$. That is to say, the spinodal region is in the range $\rho < 0.6\rho_0$. It may look strange that T_{eff} is a little below zero at $\rho = 0.6\rho_0$. This is because the momentum is not proportional to the velocity due to the momentum dependent potentials. The situation $\mathbf{P}_i \cdot \frac{\partial V}{\partial \mathbf{P}_i} < 0$ leads to the negative temperature.

The Fig. 3.4 includes only $h = 0.1$ case. More rapid expansions $h = 0.5, 1.0, 2.0$ are also carried out but the results are almost the same as those of $h = 0.1$. This is partly because the virial equation is used with the local component of the momentum so that the effects of expansion does not directly affect the dynamics. To see the effect of h on the local pressure and the local temperature, it is necessary to carry out the simulation of slower expanding matter. Unfortunately, $h = 0.1$ is the lowest limit in our QMD simulation because slower expansion requires very long computational time.

3.3   Quasi static limit

In this section, to simulate a very slow expanding system which is regarded as quasi static, a classical Molecular Dynamics with the Lennard-Jones (LJ) potential is utilized. The LJ potential has features similar to the nuclear potential in the sense that it has a short range repulsion and a long range attraction. We can expect that expanding matter with the LJ potential behaves similarly as that with the QMD potential. Using the LJ potential instead of the QMD potential, the quantities which appear in the model becomes simple. In particular, the effective temperature is always positive as opposed to the negative temperature of the QMD expanding matter. This allows us to clarify some uncertain points in the previous discussion.

For the LJ system, it is possible to calculate the exact coexistent region by the Gibbs ensemble method. The coexistent region is compared with the effective

temperature of the expanding matter with $h = 0.001$. In addition, an inhomogeneity function is introduced to investigate how the density fluctuation grows during time evolution.

3.3.1 Molecular Dynamics with Lennard-Jones system

Lennard-Jones potential

The original LJ potential is given as follows:

$$v_0(r) = 4\epsilon \left[(\frac{\sigma}{r})^{12} - (\frac{\sigma}{r})^6 \right]. \tag{3.17}$$

However, we use the following modified form with a cutoff distance:

$$v(r) = \begin{cases} v_0(r) - v_0(r_{\text{cut}}) - \frac{\partial v_0(r)}{\partial r}(r - r_{\text{cut}}) & r \leq r_{\text{cut}} \\ 0 & r > r_{\text{cut}}, \end{cases} \tag{3.18}$$

where $r_{\text{cut}} = 2.5$ and σ, ϵ are the unit of length and energy respectively. The derivative with respect to r is introduced to ensure that the potential approaches smoothly zero at r_{cut}. Without this additional term, the cutoff would cause an unphysical force at r_{c} [36].

Reduced units

All quantities are expressed in reduced units, including σ, ϵ and the particle mass M. In particular, the collective momentum is simply expressed by $h\mathbf{r}$, where h is also non-dimension. Thus, the effective temperature is given by:

$$\frac{3}{2}T_{\text{eff}} = \frac{1}{N}\sum_{i=1}^{N} \frac{(\mathbf{P}_i - h\mathbf{R}_i)^2}{2}, \tag{3.19}$$

where particle mass is 1 in reduced units.

Equations of motion

The equation of motion with the LJ potential is solved by the velocity-Verlet algorithm (see Appendix B.2). The time step dt is set at $hdt = 0.0004$ in reduced units. For $h = 0.001$, however, $dt = 0.004$ is used.

3.3.2 Coexistent region

It is known that the LJ system shows the liquid-gas phase transition. That is to say, the expanding matter model with the LJ system allows us to investigate how the expanding motion affects the liquid-gas phase transition. Furthermore, for the LJ system, an exact coexistent curve in the density-temperature plane can be calculated with the help of the Gibbs ensemble method, which is an advanced version of the Metropolis method (see Appendix C). The inside of the coexistent curve is the

coexistent region, where fragmentation is expected to occur in the thermodynamical limit.

Notice that the spinodal region defined as $\frac{\partial P}{\partial \rho} < 0$ is different from the coexistent region, where liquid and gas have the common pressure and the common chemical potential. On the other hand, there are two kinds of the spinodal region, one is isothermal spinodal region and the other is adiabatic spinodal region. In case of van der Waals model, the isothermal spinodal region is inside of the coexistent region and the adiabatic spinodal region is further inside of the isothermal spinodal region (see Appendix D).

3.3.3 Inhomogeneity function

During the time evolution, the pressure and the temperature change with decreasing density, where the density fluctuation grows. To measure the density fluctuation directly, the following function is introduced:

$$S(\rho) = \frac{n_{\mathrm{pair}}}{\frac{n}{2}\left(\frac{4}{3}\pi r_{\mathrm{cut}}^3 \rho - 1\right)}, \tag{3.20}$$

where the denominator is the number of the pairs when the system is completely homogeneous, while the numerator n_{pair} is the actual number of pairs which is calculated in the minimum image convention.

When the system is completely homogeneous, the number of particles which interacts with a particle is $\frac{4}{3}\pi r_{\mathrm{cut}}^3 \rho - 1$. The total number is divided by two to avoid the double counting.

By definition, $S(\rho) = 1$ only when the system is homogeneous, in which case the number of the pairs in the system is minimum. As the density fluctuation grows, the number of pairs increases. Using this property of the function, the inhomogeneity of the system is estimated during the time evolution of expanding matter.

3.3.4 Expanding matter with Lennard-Jones potential

We will perform the simulation of expanding matter composed of 1372 particles with $h = 0.1$ and $h = 0.001$, the latter of which is slow enough to be regarded as quasi static. The pressure, the effective temperature and the inhomogeneity function are calculated during the expansion and compared with the coexistence curve obtained by the Gibbs ensemble method. Figure 3.5 shows the density dependence of the pressure, the effective temperature and the inhomogeneity $S(\rho)$ for $h = 0.001$ (left) and $h = 0.1$ (right). The initial temperatures are set at $T_{\mathrm{ini}} = 1$ (thick line), $T_{\mathrm{ini}} = 3$ (thin line) and $T_{\mathrm{ini}} = 5$ (dotted line) in the reduced unit. The pressures are shown in the top panel. The effective temperatures are shown in the middle panel with the coexistence curve (open circle) calculated by the Gibbs ensemble method. The inhomogeneity is shown in the bottom panel.

First of all, it should be noted that the critical temperature T_{c} for the LJ system is around 0.95 in reduced unit, which is identified as the max point of the coexistent curve plotted in the middle panel. Thus, the initial temperature $T_{\mathrm{ini}} = 1$ is near the
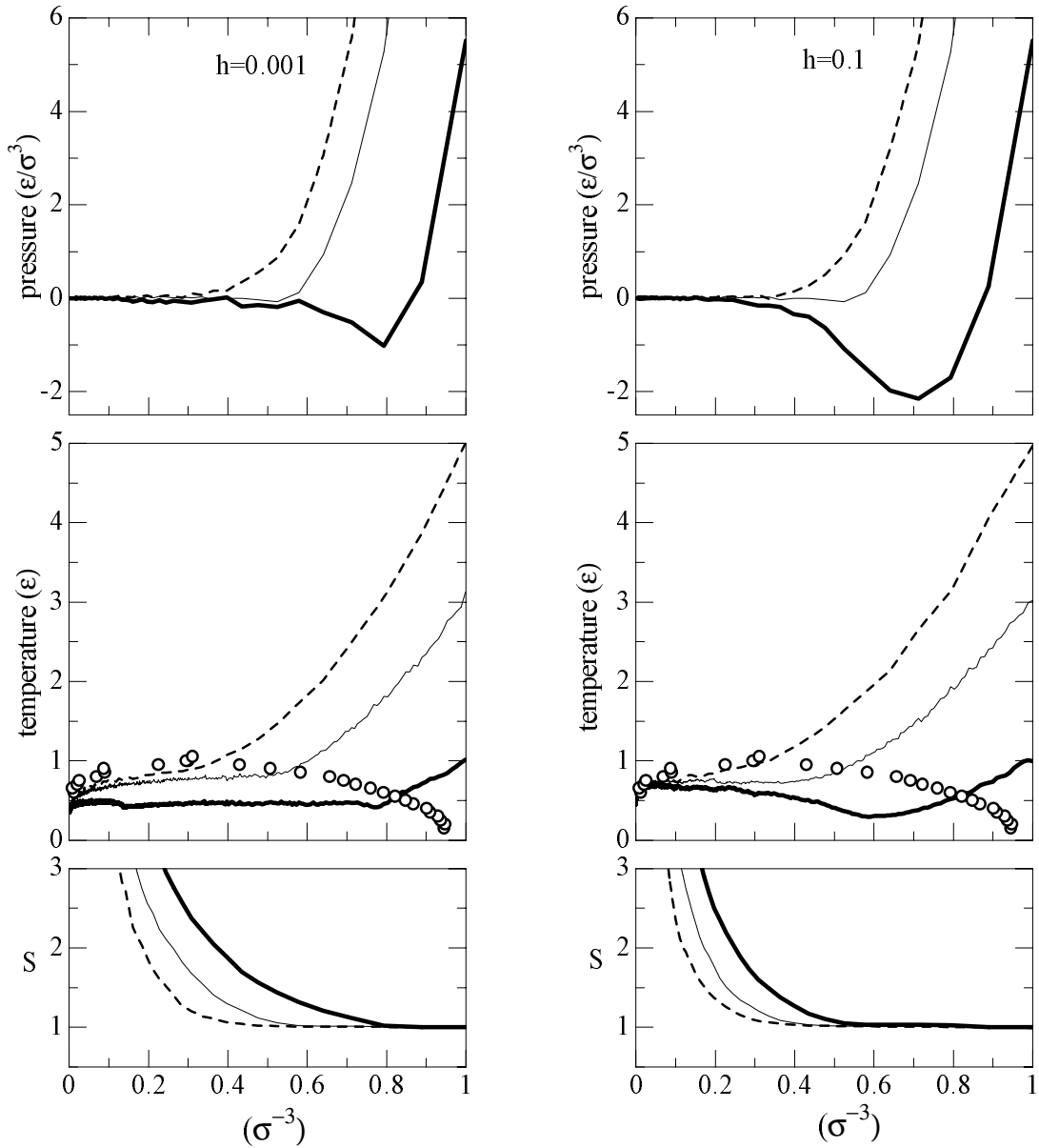
Figure 3.5: The pressure, the effective temperature and the inhomogeneity S as a function of average density ρ. The left hand side is for $h = 0.001$ and the right hand side is for $h = 0.1$. In each side, the pressure is plotted in the top panel, the effective temperature is plotted in the middle panel and corresponding inhomogeneity S is plotted in the bottom panel. The broken line is for $T_{\mathrm{ini}} = 5$, the thin solid line is for $T_{\mathrm{ini}} = 3$, and the bold line is for $T_{\mathrm{ini}} = 1$. The open circles are calculated by the Gibbs ensemble method and form a liquid-gas coexistence curve. ϵ is unit of energy and σ is unit of length used in the LJ system [30].

critical temperature T_c and $T_{ini} = 3, 5$ are above the T_c. Roughly speaking, these initial temperatures $1, 3, 5$ for the LJ system correspond to the initial temperatures $5, 15$ and 30 MeV for the QMD system.

Consider the case of $h = 0.001$ in the left hand side, which is considered to be slow enough to be regarded as quasi static process. In the middle panel, it is impressive that the effective temperatures for $T_{ini} = 1, 3$ remain constant in the coexistent region. The effective temperatures decrease with decreasing density untill the system enters the coexistent region, outside of which we cannot distinguish between gas and liquid. When the system reaches the coexistence curve, the system is separated into liquid and gas, the former of which appears as fragments. During the phase separation, the effective temperatures for $T_{ini} = 1, 3$ remain constant, which is a characteristic of the first order phase transition. However, the effective temperature for $T_{ini} = 5$ continues to decrease after the system enters the coexistent region.

In the top pannel, the corresponding pressures are plotted. We see that the pressures for $T_{ini} = 3, 5$ remain zero just after the system reaches the coexistence curve. On the other hand, the pressure for $T_{ini} = 1$ reaches at a negative minimum when the system reaches the coexistence curve. As the system goes inside the coexistent region, the pressure for $T_{ini} = 1$ fluctuates and reaches to zero, which part corresponds to the spinodal region $\frac{\partial P}{\partial \rho} < 0$.

Now, the bottom panel shows what happens about the stability of matter in expanding matter during the time evolution. An increase in S indicates an increase of the inhomogeneity. The figure clearly shows that the inhomogeneity starts to increase at the density where the system reaches the coexistence curve. In this way, the very slow expanding matter with $h = 0.001$ is governed by the coexistent region.

On the other hand, for the expanding matter with $h = 0.1$, the coexistence curve does not work as the border of the inhomogeneity. All effective temperatures continue to decrease even after the system enters the coexistent region. The effective temperature for $T_{ini} = 1$ decreases towards 0.3 as the density reaches at $\rho = 0.6$ and, afterwards, increases to 0.6, which value is common to other effective temperature cases.

As density decreases, the pressures for $T_{ini} = 5, 3$ become zero similarly to the case of $h = 0.001$. However, the pressure for $T_{ini} = 1$ reaches the minimum at -2.1 after the system goes well inside the coexistent region. The minimum of the pressure for $h = 0.1$ is deeper than that for $h = 0.001$. This is because the fragmentation is not well developed due to the relatively fast expansion for $h = 0.1$. In view of the spinodal region, the density fluctuation should occur at least after the density reaches $\rho = 0.7$.

Actually, the inhomogeneity function in the bottom figure shows that the density fluctuation for $T_{ini} = 1$ occurs at smaller density around $\rho = 0.5$. We see that the other inhomogeneities also start to increase in smaller density region as compared to the case of $h = 0.001$. From the comparison between $h = 0.1$ and $h = 0.001$, the homogeneity of the expanding matter is maintained untill smaller density for faster expanding motion.

Chapter 4

Fragment mass distribution

In the previous chapter, the instability of the expanding matter was investigated by the effective temperature, the pressure and the inhomogeneity during the time evolution. At the end of the simulation, the instability appears as a fragment mass distribution, which can be observed in experiments. In the heavy ion collision experiments, there are two kinds of fragment mass distributions.

One is a power law distribution $Y(A) = A^{-\tau}$, where A is the mass number and τ is a critical exponent, which is observed in the spectator region. The spectator region is often regarded as thermalized matter because collective motions like radial flow play a minor role. The power law is thought to indicate a second order phase transition because the power law includes a critical exponent τ. The other distribution is the exponential distribution, which is observed in the participant region with large radial flow. The exponential distribution is considered to have close relation to the expanding motion.

These two kinds of fragment mass distributions are also observed in the expanding matter model. The power law is found in slow expanding matter, while the exponential shape is found in rapid expanding matter. In the framework of the expanding matter model, we can see that the fragment mass distribution changes from the power law to the exponential shape as the speed of the expanding motion increases. On the other hand, these fragment mass distributions also appear in thermalized systems generated by the Metropolis method, in which case the thermal equilibrium is satisfied. In this chapter, the origin of these fragment mass distributions will be investigated.

4.1   Nuclear fragment mass distribution

In this section, we will investigate the fragment mass distribution resulting from the expanding matter with QMD interaction. There are two parameters in the expanding matter model: the speed of expansion h and the initial temperature T_{ini}. Our purpose is to relate these parameters to the resultant fragment distribution.

We prepare 1000 samples of nuclear matter composed of 200 nucleons at the saturation density ρ_0 with T_{ini} by the Metropolis method, and afterwards boosted them by h. The time evolution of the expanding matter is calculated from ρ_0 to

Table 4.1: The time for expansion from ρ_0 to $0.001\rho_0$

h	0.1	0.5	1.0	2.0
time (fm/c)	575	115	57.5	28.8

$0.001\rho_0$. The same time evolution is carried out for the different 1000 samples. The resultant configurations at $0.001\rho_0$ provide us with a fragment mass distribution for a given (h, T_{ini}).

4.1.1 Fragment identification

Identification of fragments is carried out after the density becomes small enough that fragments are well separated. Fragments can be identified below $0.05\rho_0$, where an average distance between particles is larger than the interaction length. Each fragment is identified in such a way that the distance from a particle to its nearest neighbor is within a certain distance r_{id} in the fragment. Fragment identification should be carried out at densities as low as possible, where the fragment identification is independent of r_{id}. Our fragment mass distribution is calculated at $0.001\rho_0$.

It should be noted that fragments may not be stabilized even at $0.001\rho_0$. In particular, fragments resulting from rapid expanding matter are likely to be unstable. To compare the results of the expanding matter model with experimental observations, so-called secondary decay should be taken into account because the fragments observed in experiments are completely stable.

Unfortunately, typical calculation time in the time evolution with the QMD is much shorter than the time scale of secondary decay. Table 4.1 shows the duration time for expansion with h from ρ_0 to $0.001\rho_0$. Except $h = 0.1$, obtained fragment distributions may change after the system reaches at $0.001\rho_0$. However, such additional change has nothing to do with the phase transition of the expanding matter we are interested in. Thus, in the following discussion, we will concentrate on the primary fragmentation at $0.001\rho_0$. In this respect, the direct comparison between our calculated results and experimental data is not intended in this thesis.

4.1.2 Rapid expansion

Figure 4.1 shows the fragment mass distributions for $T_{\mathrm{ini}} = 30$ MeV, where expanding speeds are set at $h = 0.1, 0.5, 1.0$ and 2.0. Notice that the horizontal axis is linear but the vertical axis is logarithmic, where the calculated values for $h = 0.1, 0.5, 1.0$ and 2.0 are multiplied by $100, 10, 1$ and 0.1 respectively to be easily recognized.

It is found that the distributions for $h = 0.5, 1.0$ and 2.0 show straight line behavior with different slopes. This indicates that these distributions obey exponential functions. We see that the slope increases as the expanding speed increases. These features are also observed in heavy ion collisions with large collective flow [14], which corresponds to large h in the expanding matter model.
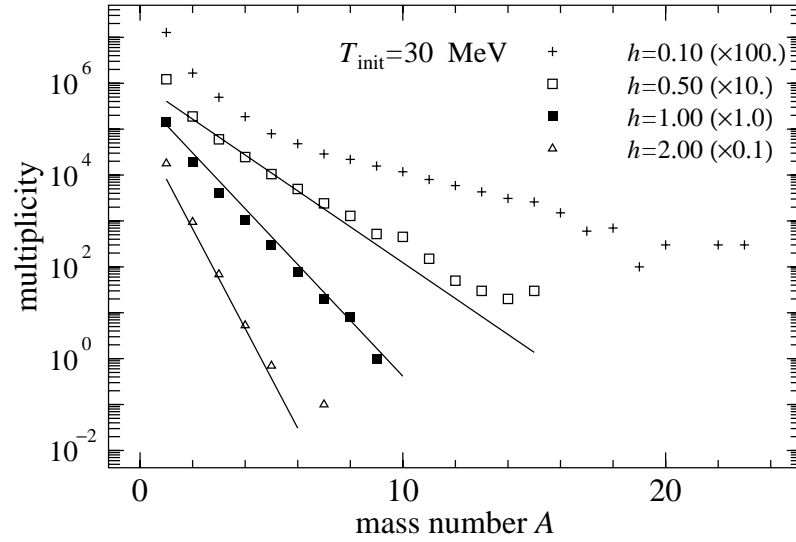
Figure 4.1: The fragment mass distribution resulting from QMD expanding matter. Notice that the graph is in semilogarithmic scale.
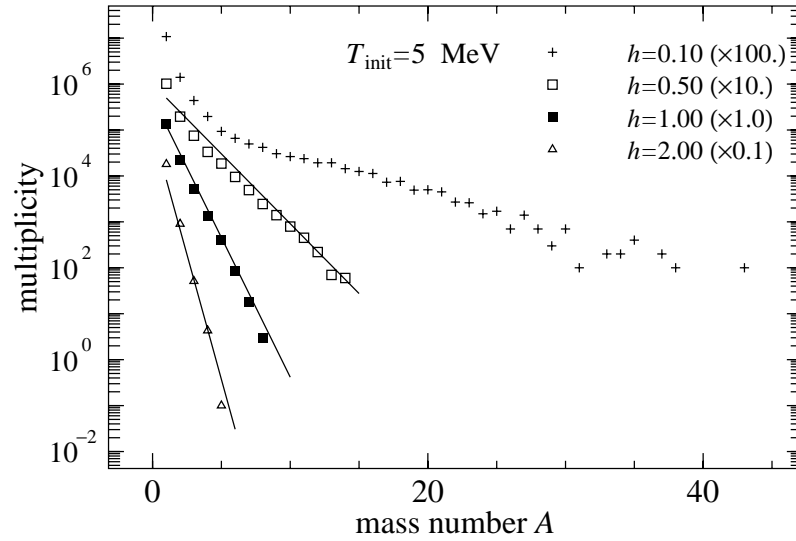

Figure 4.2: The fragment mass distribution resulting from QMD expanding matter. Notice that the graph is in semilogarithmic scale.

The case for $T_{\text{ini}} = 5$ MeV is shown in Fig. 4.2, where each distribution is similar to that of $T_{\text{ini}} = 30$ MeV except for the fact that large fragments appear due to the low temperature. This means that the exponential shape for rapid expansion is independent of initial temperature T_{ini}.

In such rapid expanding matter, the interactions play minor role. As a matter of fact, the exponential function is a characteristic of random distributions. When h is large enough to suppress the interaction, the final distribution is simply an enlarged copy of the initial configuration at saturation density ρ_0. At ρ_0, particles are distributed homogeneously and particle positions form a random distribution irrespective of T_{ini}.

Random distribution

The exponential function can be derived from the random distribution by calculating the most probable configuration of the system composed of fragments with different sizes. Let us assume a system composed of N particles, where there are N_{f} fragments and n_i is defined to be the number of the fragment with the size i. Then, the following two relations hold:

$$N_{\text{f}} \;=\; \sum_{k=1} n_k, \tag{4.1}$$

$$N \;=\; \sum_{k=1} n_k k. \tag{4.2}$$

Now consider what distribution is the most probable. The number of configurations of a set of $(n_1, n_2, \cdots)$ is given by:

$$W = \frac{N_{\text{f}}!}{n_1! n_2! n_3! \cdots}. \tag{4.3}$$

With the help of the Stirling approximation, the variation of $\ln W$ is obtained as follows:

$$\delta\left(\ln W\right) = \sum_{k=1} \delta n_k \left(\ln N_{\text{f}} - \ln n_k\right) + \lambda \sum_{k=1} k \delta n_k, \tag{4.4}$$

where λ is Lagrangian multiplier. The condition $\delta(\ln W) = 0$ leads to the expression of n_k:

$$n_k = N_{\text{f}} \exp\left(\lambda k\right). \tag{4.5}$$

In principle, n_k and λ can be uniquely determined by substituting Eq. (4.5) into the equations (4.1) and (4.2).

This equation indicates that exponential distributions are likely to be found on the condition that fragments are formed free from interactions. However, it should be noted that the above discussion does not tell us how to identify fragments. A random distributions is subject to both the density ρ and r_{id} used for the fragment identification. To assure the exponential shape, ρr_{id}^3 should be so small that fragments are separated completely.

4.1.3 Slow expansion

On the other hand, when h is small, interactions play an important role in the fragmentation. Figures 4.3 and 4.4 show the same data as Fig. 4.1 and Fig. 4.2 respectively in double logarithmic scale. In this case, $h = 0.1$ shows a straight line, which indicates so-called power law $Y(A) \propto A^{-\tau}$, where $Y(A)$ is multiplicity of the fragment of mass A and τ is a critical exponent.

Power law distributions are often explained by the Fisher's droplet model based on the grand canonical ensembles, where the pure power law appears only when the chemical potential of the gas state is equal to the that of the liquid state (see Appendix E). In the context of the droplet model, the power law is regarded as an evidence that the system undergoes a second order liquid-gas phase transition.

However, it should be noted that the power law in the Fisher's droplet model requires that the system is in thermal equilibrium. Therefore, the power law appearing in expanding matter does not necessarily imply that the system passes through the critical state predicted by the Fisher's droplet model. This is because there is no enough time to stabilize the system even for $h = 0.1$. Furthermore, in the Fisher's model, the power law must occur at the critical temperature. Nevertheless, the expanding matter which starts at $T_{\mathrm{ini}} = 5$ MeV gives a power law, in which case the fragmentation occurs well below the critical temperature of 8 MeV, which is estimated from the EOS obtained by the Metropolis method.

4.1.4 Expanding fragmentation vs. static fragmentation

In the case of expanding matter, it seems that the fragment mass distribution changes from the power law to the exponential law as the speed of expansion increases. These two kinds of distribution also appear in thermally equilibrated matter at a certain density and temperature. Using the Metropolis method, the thermalized QMD matter can be generated. Now, we will investigate what condition leads to characteristic distributions in thermalized matter.

Consider the fragment distributions for $T = 5, 8$ and 18 MeV on condition that the density is set at $\rho = 0.05\rho_0$, where the average distance between particles is larger than the interaction length. The EOS indicates that $T = 8$ MeV is the critical temperature. Figure 4.5 shows such isothermal fragment mass distributions in comparison with the distributions resulting from the expanding matter with $h = 0.1$ in double logarithmic scale. Each isothermal fragmentation is given by 1000 samples of nuclear matter at $\rho = 0.05\rho_0$, which is prepared by the Metropolis method.

We see that the fragment mass distribution for $T = 8$ MeV shows a power law with the exponent $\tau = 2.5$. This feature is consistent with the Fisher's droplet model, where the value of τ is restricted within $2 < \tau < 2.5$ [37]. Above the critical temperature, a power law is violated and an exponential shape appears like rapid expansions. In (c), we see that the distribution at $T = 18$ MeV is the exponential shape in a double logarithmic scale, where thermal motion suppresses fragmentation so that the particles are distributed in random way.

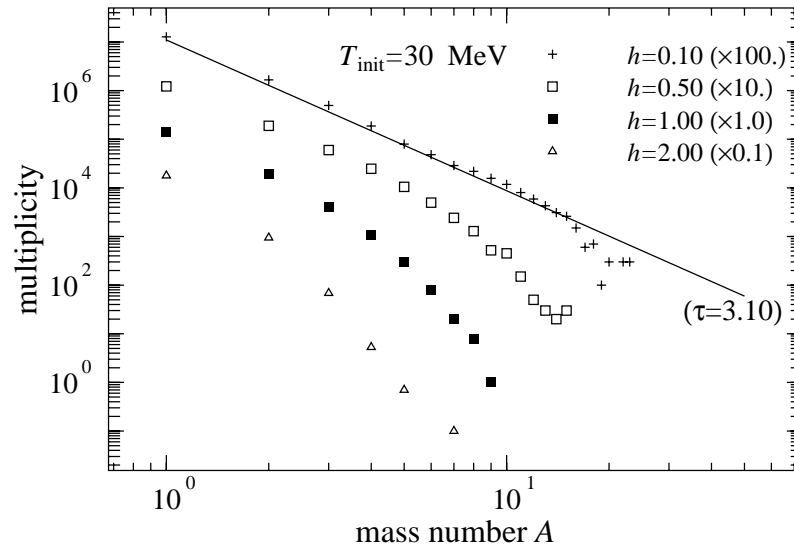It should be noted that isothermal fragment distributions are calculated with

Figure 4.3: The fragment mass distribution resulting from QMD expanding matter. Notice that the graph is in double-logarithmic scale.
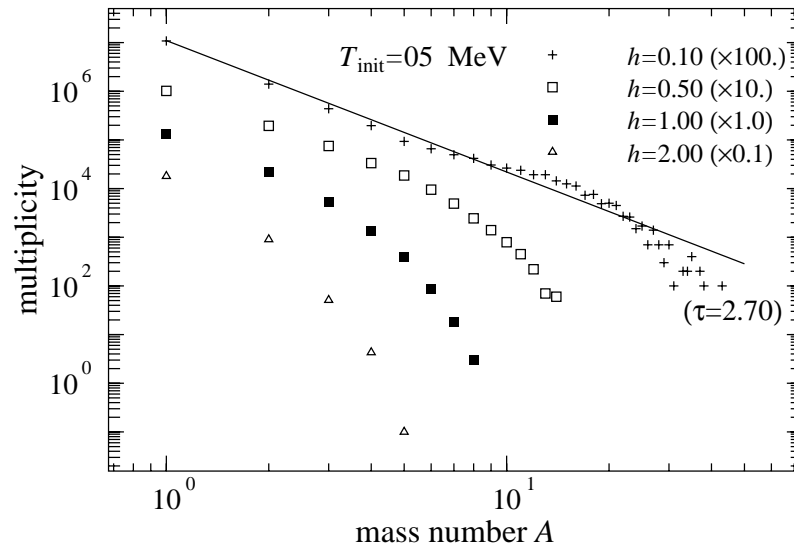

Figure 4.4: The fragment mass distribution resulting from QMD expanding matter. Notice that the graph is in double-logarithmic scale.
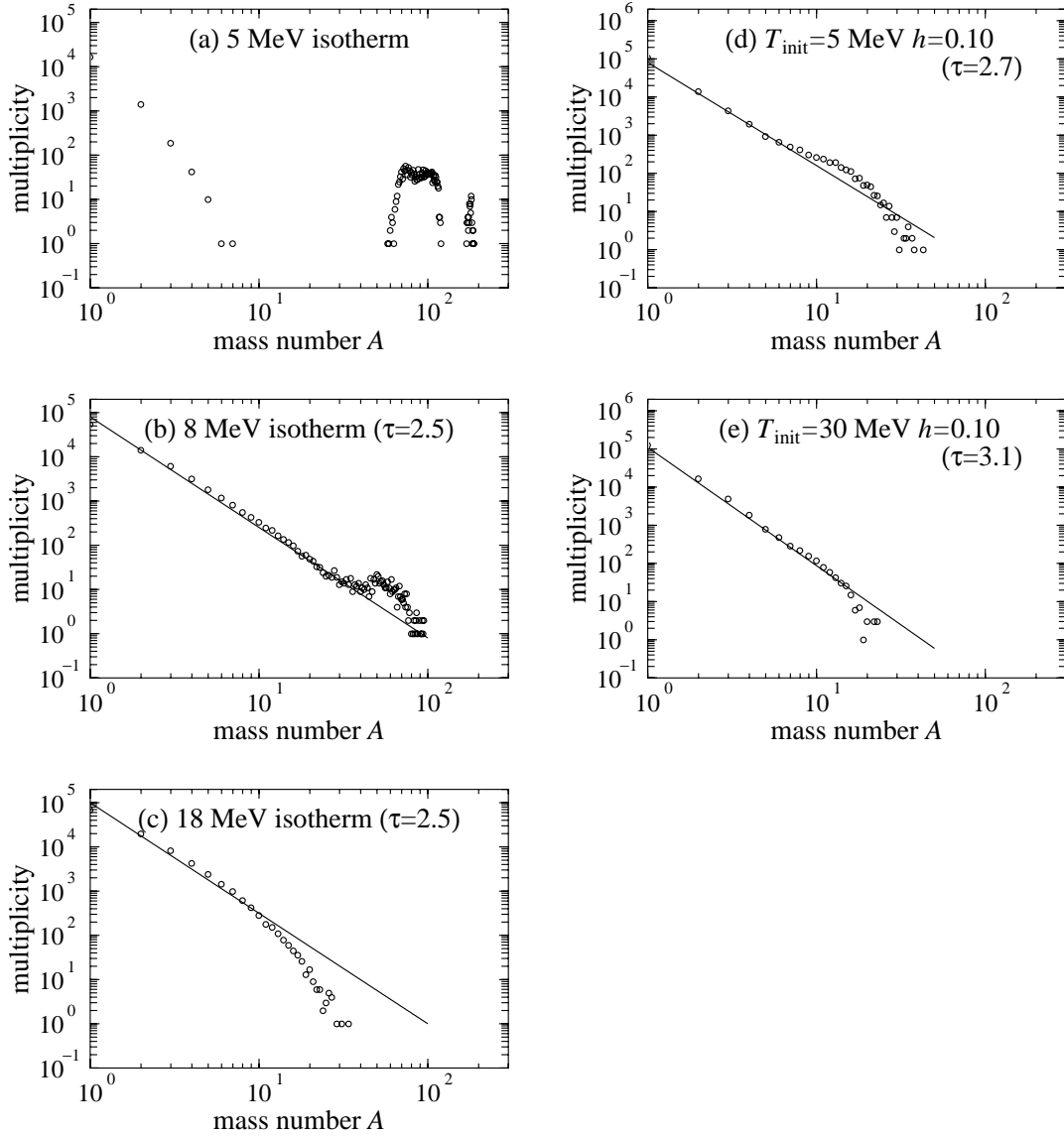
Figure 4.5: The comparison between isothermal fragmentation and expanding fragmentation. The three figures on the left hand side (a), (b) and (c) are isothermal distributions ($T = 5, 8, 18$ MeV) at $\rho = 0.05\rho_0$. The two figures on the right hand side (d) and (e) are the distributions obtained by the expanding model ($h = 0.10$)

$r_{id} = 3$ fm. In the case of the expanding matter, the fragment mass distribution is independent of r_{id} because the distribution is evaluated at a small density $0.001\rho_0$. However, $0.05\rho_0$ adopted for isothermal calculation is not so small to satisfy that the distribution is independent of r_{id}. The power law for $T = 8$ MeV is subject to both $r_{id} = 3$ fm and $\rho = 0.05\rho_0$. In fact, it is possible that the random distribution shows a power law when the ρr_{id}^3 is intentionally selected. In this context, ρr_{id}^3 corresponds to the occupation probability of the site percolation model.

On the other hand, $T = 5$ MeV in (a) is neither the power law nor the exponential law. The system at $0.05\rho_0$ and $T = 5$ MeV is considered to be inside the coexistent region. Thus, each of 1000 samples for $T = 5$ MeV includes a few large fragments and copious monomers, which leads to the U-shape in (a). The U-shape is characteristic of critical condition in finite systems [7].

Such U-shape does not appear in the expanding matter even though the initial temperature is well below the critical temperature. We see that the fragment mass distribution resulting from the expanding matter with $T_{ini} = 5$ MeV shows a power law in (d). In this case, the fragmentation occurs at temperature of at most 5 MeV because the effective temperature decreases during the expansion. This indicates that the fragmentation mechanism of (d) is completely different from that of (b).

4.2   LJ fragment mass distribution

In the previous section, effects of expanding motion on fragment mass distributions are discussed with QMD expanding matter model. We have seen that the fragment mass distribution changes from a power law to an exponential law as the expanding velocity increases regardless of the the initial temperature. These features are considered to be general independent of the potentials used in the model. In this section, we again examine the Lennard-Jones potential and confirm whether similar features are reproduced.

4.2.1   Setup

The initial temperature T_{ini} is set at 1 and 5 in reduced units, where the former is near the critical temperature $T_c = 0.95$ and the latter is above T_c. The speed of expansion is set at $h = 0.1, 0.2, 0.3$ and 0.4. The time evolution of the expanding matter is carried out for 100 independent samples with a given (T_{ini}, h), each of which is composed of 1372 particles.

The time evolution stops when the density reaches at 0.001, where the fragment mass distribution is calculated. Using 100 samples, a distribution for a specific (T_{ini}, h) is calculated. To check the dependence of the number of the particles, the same simulations with only 500 particles are carried out. We confirm that the results from 500 particles are almost the same as the results of 1372 particles except for the $h = 0.1$ and $T_{ini} = 1$.
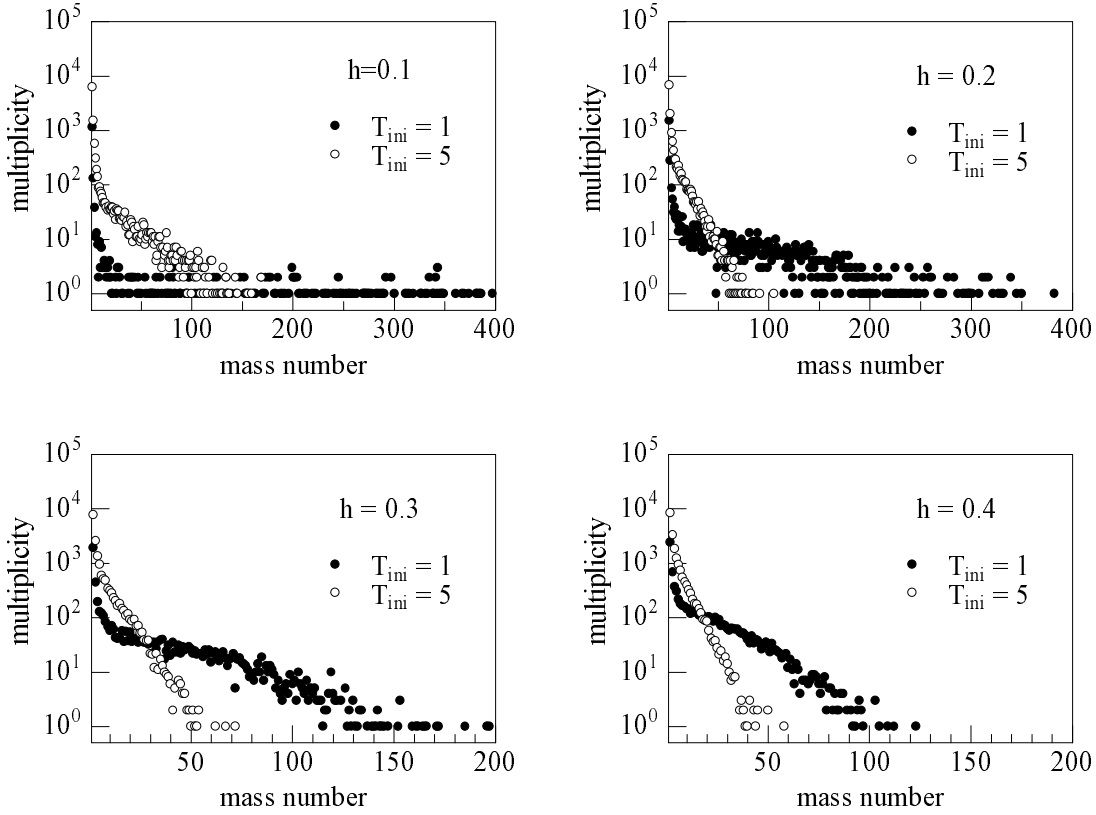
Figure 4.6: Fragment mass distribution as a result of expanding matter. The four figures are for $h = 0.1, 0.2, 0.3$ and 0.4 respectively. Each figure contains two different initial temperatures: $T_{ini} = 1$ (closed circle) and $T_{ini} = 5$ (open circle); each temperature is represented by 100 independent configurations and one primitive cell includes 1372 particles.

4.2.2 Exponential shape and bimodal distribution

Figure 4.6 shows the fragment mass distributions in semi-logarithmic scale. For $T_{ini} = 5$, we see that the distributions show an exponential shape except $h = 0.1$. In addition, the slope of the distribution in semi-log scale becomes steeper as the h increases. These features are similar to the case of the QMD expanding matter. Namely, these exponential shape indicates a random distribution resulting from the rapid expansion.

For $T_{ini} = 1$, only $h = 0.3$ and $h = 0.4$ show a clear straight line. However, there is another part in the small mass number region. The distribution for $h = 0.1$ and $T_{ini} = 5$ also has two components in similar way. This distribution is called a bimodal exponentials, which is discussed in [28, 29] using the same expanding matter model. According to [28], the large mass number region comes from fragments, while the small mass number region comes from monomers. In the case of the QMD expanding matter, the large mass number region is considered to be hidden because there are
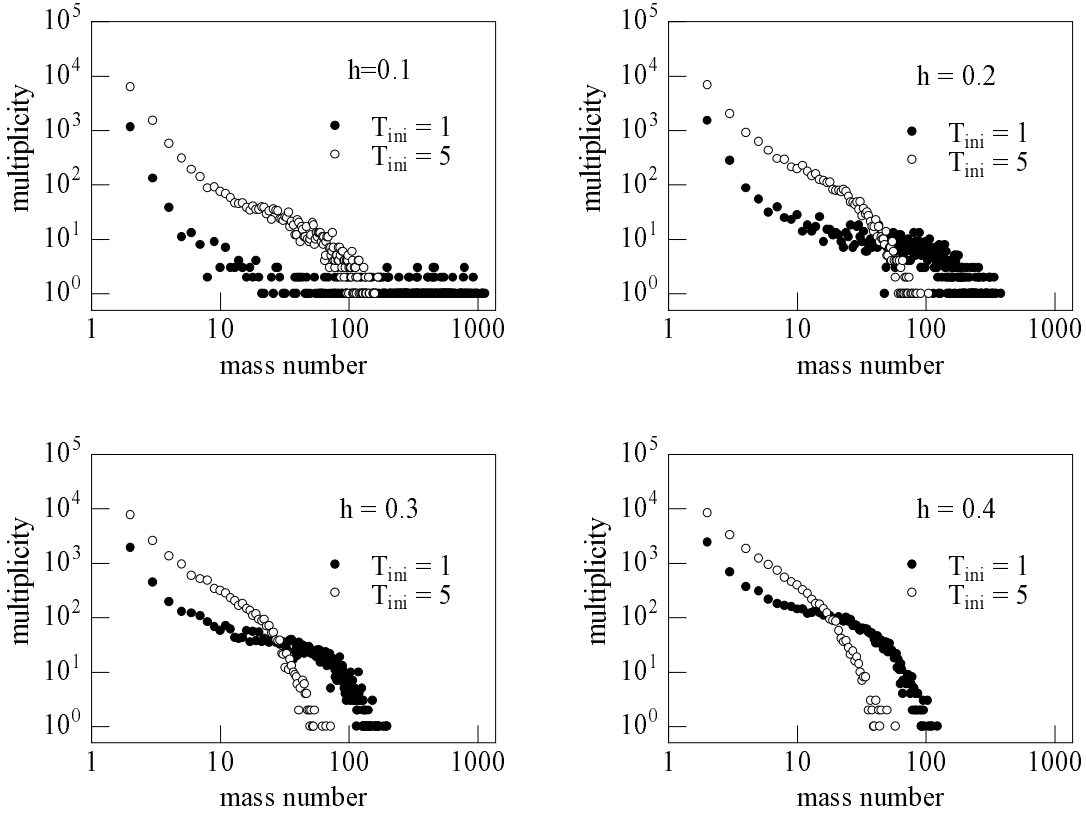
Figure 4.7: The same data as Fig. 4.6 in double logarithmic scale.

only 200 particles in the system.

4.2.3 Power law

Let us investigate the same data in double logarithmic scale shown in Fig. 4.7. We see that the monomer part of the bimodal distribution for $T_{\mathrm{ini}} = 5$ and $h = 0.1$ looks like a power law as opposed to the exponential shape stated in [28]. If the max fragment mass is restricted, it is possible that only this part appears in the system. This is exactly the case of the QMD expanding matter with only 200 particles.

On the other hand, the distribution for $T_{\mathrm{ini}} = 1$ and $h = 0.1$ shows completely different shape, where very large fragments appear. The max fragment mass number reaches almost the number of particles in the primitive cell. This means that the more the system includes particles, the larger the max fragment mass becomes. However, the small mass number region is similar to the corresponding part of the U-shape in Fig. 4.5. For $h = 0.2$ and $T_{\mathrm{ini}} = 1$, the max fragment mass number is independent of the system size. We see that the small mass number region is similar to the $T_{\mathrm{ini}} = 5$ MeV and $h = 0.1$ of the QMD expanding matter shown in Fig. 4.5.

4.2.4 Final remarks

We have investigated the fragment mass distributions resulting from the expanding matter with both the QMD potential and the LJ potential. The exponential shape is considered to be a general feature for rapid expanding matter. However, the monomer part of the bimodal exponentials resembles a power law shape. When only the monomer part survives, it may be regarded as a power law. This situation occurs in small systems like heavy ion collisions.

The two parts of the bimodal exponentials correspond to the liquid phase and the gas phase. That is, the monomer part is subject to the behavior of the gas phase, which depends on how the phase separation between liquid and gas proceeds during the expansion. As discussed in the previous chapter, the system goes through a specific path in the coexistent region according to the initial temperature and the speed of the expansion. During the time evolution, the phase separation proceeds with accumulating density fluctuations, where the bimodal exponentials are organized.

Chapter 5

Conclusion

In this thesis, we have developed the expanding matter model based on QMD, with which we can investigate both statical and dynamical aspects of nuclear matter by making use of generalized periodic boundary conditions. This new QMD model enables us to simulate the dynamics of fragmentation free from the complication due to the finiteness of the system. The expanding matter model has two parameters, which are the speed of expansion h and the initial temperature T_{ini}. By controlling these parameters, the instability and the resultant fragmentation in both static and dynamic nuclear matter have been investigated in an unified way for the first time.

Static nuclear matter which corresponds to $h = 0$ has been studied by the Metropolis method. The equation of state (EOS) of static nuclear matter shows the presence of the isothermal spinodal region. As opposed to the models assuming homogeneous matter, nuclear matter composed of the QMD wave packets shows the special property of nuclear matter as composite of nucleons, i.e., the critical temperature T_{c} is identified as 8 MeV which is lower than typical matter value and the spinodal region is narrower due to the fragmentation. In order to get more clear insight to the relation of these features to the liquid-gas phase transition, we need to investigate the Gibbs ensemble method with the QMD which is a future work. The configuration at $0.05\rho_0$ shows the fragment mass distribution which is consistent with the Fisher's droplet model, where the power law appears at the critical temperature.

Slowly expanding matter with small h simulates the spectator region without surface effect. With the virial equation for the instantaneous pressure, the density-pressure curve has been calculated and compared with the EOS of static matter. The dynamical spinodal region is significantly affected by the expanding motion, which enhances the stability of the matter. That is, the matter maintains its homogeneity after the matter goes over the coexistence curve determined in thermal equilibrium. The fragment mass distribution coming from slowly expanding matter shows a power law in small mass regions irrespective of the initial temperature. The origin of this power law is thought to be different from what is predicted by the Fisher's droplet model, where the power law appears in the critical point and the system is in thermal equilibrium. In our case, the expanding process is clearly in non-equilibrium and the fragmentation happens when the effective temperature is far

below critical temperature.

The rapid expansion with large h simulates the participant region, where collective motion plays an important role. The value of h corresponds to the speed of the radial flow in heavy-ion reaction. The fragment mass distribution coming from rapid expansion shows an exponential shape, which is a characteristic of a random distribution. The slope of the exponential shape becomes steep as the expansion speed increases. This feature is consistent with the experimental results observed in heavy ion collision with strong radial flow. In case of Lennard-Jones system, it is found that the exponential shape is composed of two parts to form a bimodal distribution. The small fragment region of the bimodal distribution appears as a power law in case of the slow expanding matter. This feature may be a common and universal aspect of expanding system, irrespective of the precise form of the interaction between particles.

In this way, the expanding matter has enabled us to explore several aspects of nuclear matter in unified way. This thesis is mainly devoted to nuclear matter, but the dynamics of the expanding matter and resultant fragmentation is thought to be general because the Lennard-Jones system shows several common features to QMD system. In particular, the universality of power law distribution resulting from the expanding matter might be a signature of self-organized criticality. The mechanism of such a power law is subject to how the matter goes through inside the unstable regions, during which density fluctuations are accumulated in a complex way. This process is thought to be a dynamical phase transition which is different from what is considered in thermal physics. The expanding matter model has a capability to tackle this problem.

Acknowledgment

Appendix A

QMD potential

A.1 Pauli potential

The Pauli potential is derived from the eigenvalue of the kinetic energy with respect to the anti-symmetrized state. Let us consider an anti-symmetrized coherent state composed of two particles, which can be separated into center-of-mass and relative motions [24]:

$$|\phi_{\mathbf{Z}_1}\rangle \otimes |\phi_{\mathbf{Z}_2}\rangle - |\phi_{\mathbf{Z}_2}\rangle \otimes |\phi_{\mathbf{Z}_1}\rangle \equiv |\phi_{\mathbf{Z}_1}\phi_{\mathbf{Z}_2} - \phi_{\mathbf{Z}_2}\phi_{\mathbf{Z}_1}\rangle = |\phi_{\mathbf{Z}_G}\phi_{+\mathbf{z}} - \phi_{\mathbf{Z}_G}\phi_{-\mathbf{z}}\rangle, \quad (A.1)$$

where $\mathbf{Z}_i$ indicates the eigenvalue of the coherent state for i-th particle, $\mathbf{Z}_G = \frac{1}{2}(\mathbf{Z}_1 + \mathbf{Z}_2)$ is for the center-of-mass and $\mathbf{Z} = \mathbf{Z}_1 - \mathbf{Z}_2$ is for relative motion. For simplicity, the internal degrees of freedom are neglected. Then, the eigenvalue of the kinetic energy can be expressed as follows:

$$\frac{\langle \phi_{\mathbf{Z}_1}\phi_{\mathbf{Z}_2} | \frac{\hat{\mathbf{p}}^2}{2m} | \phi_{\mathbf{Z}_1}\phi_{\mathbf{Z}_2} - \phi_{\mathbf{Z}_2}\phi_{\mathbf{Z}_1}\rangle}{\langle \phi_{\mathbf{Z}_1}\phi_{\mathbf{Z}_2} | \phi_{\mathbf{Z}_1}\phi_{\mathbf{Z}_2} - \phi_{\mathbf{Z}_2}\phi_{\mathbf{Z}_1}\rangle} = \frac{\langle \phi_{+\mathbf{z}} | \frac{\hat{\mathbf{p}}^2}{2m} | \phi_{+\mathbf{z}} - \phi_{-\mathbf{z}}\rangle}{\langle \phi_{+\mathbf{z}} | \phi_{+\mathbf{z}} - \phi_{-\mathbf{z}}\rangle}. \quad (A.2)$$

The annihilation operator is related to the position operator and the momentum operator as follows:

$$\hat{\mathbf{a}} = \sqrt{\nu}\hat{\mathbf{r}} + \frac{i}{2\hbar\sqrt{\nu}}\hat{\mathbf{p}}, \quad (A.3)$$

Thus, the kinetic energy operator is expressed in terms of $\mathbf{a}$ and $\mathbf{a}^\dagger$:

$$\frac{\hat{\mathbf{p}}^2}{2m} = -\frac{\hbar^2\nu}{2m}(\hat{\mathbf{a}} - \hat{\mathbf{a}}^\dagger)^2. \quad (A.4)$$

Using the eigen equation

$$\hat{\mathbf{a}}|\phi_{\pm\mathbf{z}}\rangle = \pm\mathbf{Z}|\phi_{\pm\mathbf{z}}\rangle, \quad (A.5)$$

we see the eigenvalue of the kinetic energy can be expressed in terms of $\mathbf{Z}$ and $\mathbf{Z}^\star$. Furthermore, $\mathbf{Z} \equiv \mathbf{Z}_1 - \mathbf{Z}_2$ is separated into the position $\mathbf{R} \equiv \mathbf{R}_1 - \mathbf{R}_2$ and the momentum $\mathbf{P} \equiv \mathbf{P}_1 - \mathbf{P}_2$ as follows:

$$\mathbf{Z} = \sqrt{\nu}\mathbf{R} + \frac{i}{2\hbar\sqrt{\nu}}\mathbf{P} = \sqrt{\nu}(\mathbf{R}_1 - \mathbf{R}_2) + \frac{i}{2\hbar\sqrt{\nu}}(\mathbf{P}_1 - \mathbf{P}_2). \quad (A.6)$$

Then, the direct term and the exchange term of the kinetic energy are obtained by:

$$\langle \phi_{+\mathbf{z}} | \frac{\hat{\mathbf{p}}^2}{2m} | \phi_{+\mathbf{z}} \rangle = \left[\frac{\mathbf{P}^2}{2m} + \frac{3}{2} \frac{\hbar^2 \nu}{m} \right] \langle \phi_{+\mathbf{z}} | \phi_{+\mathbf{z}} \rangle, \tag{A.7}$$

$$\langle \phi_{+\mathbf{z}} | \frac{\hat{\mathbf{p}}^2}{2m} | \phi_{-\mathbf{z}} \rangle = \left[-2\mathbf{R}^2 \frac{\hbar^2 \nu}{m} + \frac{3}{2} \frac{\hbar^2 \nu}{m} \right] \langle \phi_{+\mathbf{z}} | \phi_{-\mathbf{z}} \rangle. \tag{A.8}$$

When $\langle \phi_{\mathbf{Z}} | \phi_{\mathbf{Z}} \rangle = 1$, the coherent state $|\phi_{\mathbf{Z}}\rangle$ is given by

$$|\phi_{\mathbf{Z}}\rangle = \frac{e^{\mathbf{Z} \cdot \hat{\mathbf{a}}^\dagger}}{e^{\frac{1}{2}|\mathbf{Z}|^2}} |0\rangle, \tag{A.9}$$

and the overlap of different coherent states are obtained as follows:

$$\langle \phi_{\mathbf{Z}_1} | \phi_{\mathbf{Z}_2} \rangle = \frac{e^{\mathbf{Z}_1^\star \cdot \mathbf{Z}_2}}{e^{\frac{1}{2}|\mathbf{Z}_1|^2} e^{\frac{1}{2}|\mathbf{Z}_2|^2}}. \tag{A.10}$$

Using this, the following relation is obtained:

$$\frac{\langle \phi_{+\mathbf{z}} | \frac{\hat{\mathbf{p}}^2}{2m} | \phi_{+\mathbf{z}} - \phi_{-\mathbf{z}} \rangle}{\langle \phi_{+\mathbf{z}} | \phi_{+\mathbf{z}} - \phi_{-\mathbf{z}} \rangle} = \frac{\langle \phi_{+\mathbf{z}} | \frac{\hat{\mathbf{p}}^2}{2m} | \phi_{+\mathbf{z}} \rangle}{\langle \phi_{+\mathbf{z}} | \phi_{+\mathbf{z}} \rangle} + \frac{\hbar^2 \nu}{m} \frac{|\mathbf{Z}^2|}{\sinh(|\mathbf{Z}|^2)} \exp\left[-|\mathbf{Z}|^2 \right]. \tag{A.11}$$

The first term in the right hand side is the eigenvalue of the kinetic energy with respect to the single particle state. The second term becomes the Pauli potential, which is a function of $|\mathbf{Z}|^2$:

$$|\mathbf{Z}|^2 = \nu |\mathbf{R}_1 - \mathbf{R}_2|^2 + \frac{1}{4\hbar^2 \nu} |\mathbf{P}_1 - \mathbf{P}_2|^2. \tag{A.12}$$

On the other hand, the function $\frac{|\mathbf{Z}|^2}{\sinh(|\mathbf{Z}^2|)} \sim 1$ holds around $\mathbf{Z} = 0$. Therefore, the second term is approximated as follows:

$$
\begin{aligned}
\frac{\hbar^2 \nu}{m} \frac{|\mathbf{Z}^2|}{\sinh(|\mathbf{Z}|^2)} \exp\left[-|\mathbf{Z}|^2 \right] \quad &\sim \quad \frac{\hbar^2 \nu}{m} \exp\left[-\nu |\mathbf{R}_1 - \mathbf{R}_2|^2 - \frac{1}{4\hbar^2 \nu} |\mathbf{P}_1 - \mathbf{P}_2|^2 \right] \\
&\rightarrow \quad \frac{C_{\mathrm{P}}}{(q_0 p_0 / \hbar c)^3} \exp\left[-\frac{|\mathbf{R}_1 - \mathbf{R}_2|^2}{2q_0^2} - \frac{|\mathbf{P}_1 - \mathbf{P}_2|^2}{2p_0^2} \right],
\end{aligned} \tag{A.13}
$$

where p_0 and q_0 are introduced as free parameters. The replacement of the last line is carried out in a phenomenological sense. Taking the internal degrees of freedom into account, this is the Pauli potential.

A.2 Derivatives of QMD potential

QMD potential is summarized as follows:

$$V = \frac{1}{2} \sum_{i=1}^{N} \sum_{j=1}^{N} v_{ij} + g_{\mathrm{density}} \sum_{i=1}^{N} \langle \tilde{\rho}_i \rangle^\tau, \tag{A.14}$$

where v_{ij} is two-body potentials, g_{density} is a constant and $\langle \tilde{\rho}_i \rangle^\tau$ is given by

$$\langle \tilde{\rho}_i \rangle \equiv \sum_{j(\neq i)}^{N} \frac{1}{(4\pi \tilde{L})^{3/2}} \exp\left[-\frac{R_{ij}^2}{4\tilde{L}} \right], \tag{A.15}$$

where $\tilde{L}$ is defined by

$$\tilde{L} = \frac{L}{2}(\tau + 1)^{\frac{1}{\tau}}. \tag{A.16}$$

The two-body potentials are proportional to the overlap ρ_{ij} except for the Pauli potential:

$$\begin{aligned}
v_{ij} &= \left[g_{\text{Skyrme}} + g_{\text{symmetry}} \left(1 - 2|c_i - c_j| \right) + g_{\text{surface}} \left(\frac{3}{2} - \frac{R_{ij}^2}{4L} \right) \right. \\
&\quad \left. + \frac{g_{\text{ex}(1)}}{1 + \left(\frac{P_{ij}}{\mu_1 \hbar} \right)^2} + \frac{g_{\text{ex}(2)}}{1 + \left(\frac{P_{ij}}{\mu_2 \hbar} \right)^2} \right] \rho_{ij} + g_{\text{Pauli}} \exp\left[-\frac{R_{ij}^2}{2q_0^2} - \frac{P_{ij}^2}{2p_0^2} \right] \delta_{\tau_i, \tau_j} \delta_{\sigma_i, \sigma_j},
\end{aligned} \tag{A.17}$$

where $g_{\text{Skyrme}}, g_{\text{symmetry}} \cdots$ are constants and ρ_{ij} is given by

$$\rho_{ij} \equiv \int d^3 r \rho_i(\mathbf{r}) \rho_j(\mathbf{r}) = \frac{1}{(4\pi L)^{3/2}} \exp\left[-\frac{R_{ij}^2}{4L} \right]. \tag{A.18}$$

The form of the surface potential is calculated by

$$\int d^3 r \nabla \rho_i(\mathbf{r}) \cdot \nabla \rho_j(\mathbf{r}) = \frac{1}{L} \left(\frac{3}{2} - \frac{R_{ij}^2}{4L} \right) \rho_{ij}. \tag{A.19}$$

The derivative of v_{1j} with respect to R_{1j} or P_{1j} are calculated as follows:

$$\begin{aligned}
\frac{\partial v_{1j}}{\partial R_{1x}} &= -\frac{R_{1jx}}{2L} \left[g_{\text{Skyrme}} + g_{\text{symmetry}} \left(1 - 2|c_1 - c_j| \right) + g_{\text{surface}} \left(\frac{5}{2} - \frac{R_{1j}^2}{4L} \right) \right. \\
&\quad \left. + \frac{g_{\text{ex}(1)}}{1 + \left(\frac{P_{1j}}{\mu_1 \hbar} \right)^2} + \frac{g_{\text{ex}(2)}}{1 + \left(\frac{P_{1j}}{\mu_2 \hbar} \right)^2} \right] \rho_{1j} \\
&\quad - g_{\text{Pauli}} \frac{R_{1jx}}{q_0^2} \exp\left[-\frac{R_{1j}^2}{2q_0^2} - \frac{P_{1j}^2}{2p_0^2} \right] \delta_{\tau_1, \tau_j} \delta_{\sigma_1, \sigma_j},
\end{aligned} \tag{A.20}$$

$$\begin{aligned}
\frac{\partial v_{1j}}{\partial P_{1x}} &= -\frac{2}{(\mu_1 \hbar)^2} P_{1jx} \left[\frac{g_{\text{ex}(1)}}{\left\{ 1 + \left(\frac{P_{1j}}{\mu_1 \hbar} \right)^2 \right\}^2} + \frac{g_{\text{ex}(2)}}{\left\{ 1 + \left(\frac{P_{1j}}{\mu_2 \hbar} \right)^2 \right\}^2} \right] \rho_{1j} \\
&\quad - \frac{P_{1jx}}{p_0^2} g_{\text{Pauli}} \exp\left[-\frac{R_{1j}^2}{2q_0^2} - \frac{P_{1j}^2}{2p_0^2} \right] \delta_{\tau_1, \tau_j} \delta_{\sigma_1, \sigma_j}.
\end{aligned} \tag{A.21}$$

The derivative of the density dependent potential with respect to R_{1x} is calculated as follows.

$$\frac{\partial}{\partial R_{1x}} \sum_{i=1}^{N} \langle \tilde{\rho}_i \rangle^\tau = -\frac{\tau}{2\tilde{L}} \sum_{j(\neq i)}^{N} R_{1jx} \rho_{1j} \left[\langle \tilde{\rho}_1 \rangle^{\tau-1} + \langle \tilde{\rho}_j \rangle^{\tau-1} \right]. \tag{A.22}$$

62

Appendix B

Integration Scheme

B.1 Runge-Kutta method

The Runge-Kutta method can be derived from comparing two different kinds of Talor expansions [38]. The Talor expansion of $y(t + \tau)$ is given by

$$y(t + \tau) = y(t) + \frac{dy}{dt}\tau + \frac{1}{2}\frac{d^2 y}{dt^2}\tau^2 + \frac{1}{6}\frac{d^3 y}{dt^3}\tau^3 + \frac{1}{24}\frac{d^4 y}{dt^4}\tau^4. \tag{B.1}$$

Using new variable $g(y, t) = \frac{dy}{dt}$, $y(t + \tau)$ is expressed as a function of several derivatives of g as follows:

$$y(t + \tau) = y(t) + g\tau + \frac{1}{2}(g_t + gg_y)\tau^2 + \frac{1}{6}(g_{tt} + 2gg_{ty} + g^2 g_{yy} + gg_y^2 + g_t g_y)\tau^3$$
$$+ \frac{1}{24}(3gg_{tty} + g_{ttt} + 3g^2 g_y g_{yy} + g^3 g_{yyy} + 3g^2 g_{yyt} + gg_y^3 + g_t g_y^2$$
$$+ 5gg_{ty}g_y + g_{tt}g_y + 3gg_t g_{yy} + 3g_t gyt)\tau^4. \tag{B.2}$$

On the other hand, it is possible to represent $y(t + \tau)$ in another way. We introduce a set of functions of g as follows:

$$k_1 \equiv g(y, t)\tau, \tag{B.3}$$
$$k_2 \equiv g(y + \nu_{21}k_1, t + \nu_{21}\tau)\tau, \tag{B.4}$$
$$k_3 \equiv g(y + \nu_{31}k_1 + \nu_{32}k_2, t + \nu_{31}\tau + \nu_{32}\tau)\tau, \tag{B.5}$$
$$k_4 \equiv g(y + \nu_{41}k_1 + \nu_{42}k_2 + \nu_{43}k_3, t + \nu_{41}\tau, \nu_{42}\tau + \nu_{43}\tau)\tau, \tag{B.6}$$

where, $\nu_{21}, \nu_{31}, \cdots$ are free parameters which will be defined later. We represent $y(t + \tau)$ in terms of k_1, k_2, k_3, k_4:

$$y(t + \tau) = y(t) + \alpha_1 k_1 + \alpha_2 k_2 + \alpha_3 k_3 + \alpha_4 k_4, \tag{B.7}$$

where $\alpha_1, \alpha_2, \cdots$ are also parameters. Now, we compare two kinds of expansion to obtain the Runge-Kutta method. Before that, it is necessary to fix some parameters.

We assume the following relations:

$$\nu_{21} = \frac{1}{2}, \tag{B.8}$$

$$\nu_{32} = \frac{1}{2}, \tag{B.9}$$

$$\nu_{43} = 1, \tag{B.10}$$

$$\text{the others} = 0. \tag{B.11}$$

In this case, we can express $y(t + \tau)$ as follows:

$$
\begin{aligned}
y(t + \tau) = {} & y(t) + (\alpha_1 + \alpha_2 + \alpha_3 + \alpha_4)g\tau \\
& + \frac{1}{2}(\alpha_2 + \alpha_3 + 2\alpha_4)(g_t + gg_y)\tau^2 \\
& + \frac{1}{4}(\alpha_3 + 2\alpha_4)g_t(g_y + gg_y)\tau^3 \\
& + \frac{1}{4}\alpha_4 g_y^2(g_t + gg_y)\tau^4.
\end{aligned}
\tag{B.12}
$$

Notice that there are no 2nd order term due to the choice of parameters. To compare this expansion and previous one, we obtain the relations for the parameters:

$$\alpha_1 + \alpha_2 + \alpha_3 + \alpha_4 = 1, \tag{B.13}$$

$$\alpha_2 + \alpha_3 + 2\alpha_4 = 1, \tag{B.14}$$

$$2 = 3(\alpha_3 + 2\alpha_4), \tag{B.15}$$

$$1 = 6\alpha_4. \tag{B.16}$$

Substituting these relations into $y(t + \tau)$, we obtain the following Runge Kutta formula:

$$y(t + \tau) = y(t) + \frac{1}{6}(k_1 + 2k_2 + 2k_3 + k_4), \tag{B.17}$$

$$k_1 = \tau g(y, t), \tag{B.18}$$

$$k_2 = \tau g(y + \frac{1}{2}k_1, t + \frac{1}{2}\tau), \tag{B.19}$$

$$k_3 = \tau g(y + \frac{1}{2}k_2, t + \frac{1}{2}\tau), \tag{B.20}$$

$$k_4 = \tau g(y + k_3, t + \tau). \tag{B.21}$$

B.2   Velocity-Verlet algorithm

The velocity-Verlet algorithm is a set of equations as follows:

$$r(t + \tau) = r(t) + \frac{p(t)}{m}\tau + \frac{f(t)}{2m}\tau^2, \tag{B.22}$$

$$p(t + \tau) = p(t) + \frac{f(t + \tau) + f(t)}{2}\tau. \tag{B.23}$$

The velocity-Verlet algorithm is derived from the second order Talor expansion as follows. Using the equation of motion

$$\frac{dr(t)}{dt} = \frac{p(t)}{m},\tag{B.24}$$

$$\frac{d^2 r(t)}{dt^2} = \frac{f(t)}{m},\tag{B.25}$$

$r(t + \tau)$ is expressed as follows:

$$r(t + \tau) = r(t) + \frac{p(t)}{m}\tau + \frac{f(t)}{2m}\tau^2.\tag{B.26}$$

This is just the first equation. We prepare the same equation with 2τ:

$$r(t + 2\tau) = r(t + \tau) + \frac{p(t + \tau)}{m}\tau + \frac{f(t + \tau)}{2m}\tau^2.\tag{B.27}$$

Combining Eq. (B.26) and Eq. (B.27), the following relation is obtained:

$$r(t + 2\tau) - r(t + \tau) = r(t + \tau) - r(t) + \frac{p(t + \tau) - p(t)}{m}\tau + \frac{f(t + \tau) - f(t)}{2m}\tau^2.\tag{B.28}$$

Dividing the both side by τ, the above equation is expressed in terms of p and f as follows:

$$\frac{p(t + \tau)}{m} = \frac{p(t)}{m} + \frac{f(t)}{m}\tau + \frac{f(t + \tau) - f(t)}{2m}\tau.\tag{B.29}$$

Thus, we obtain the second equation:

$$p(t + \tau) = p(t) + \frac{f(t + \tau) + f(t)}{2}\tau.\tag{B.30}$$

Appendix C

Gibbs ensemble method

The Gibbs ensemble method is a technique to calculate the coexistence curve in the density-temperature plane. The algorithm is similar to the Metropolis method, which is based on the partition function of the canonical ensemble [30].

C.1   Algorithm

First of all, we introduce an useful form of the partition function. When the interaction is independent of the momentum, the partition function of the canonical ensemble is obtained as follows:

$$Z(N,V,T) = \frac{1}{N!\Lambda(T)^{3N}} \int (d\mathbf{r})^N \exp\left[-\frac{U(\mathbf{r}^N)}{k_B T}\right], \tag{C.1}$$

where $\Lambda(T)$ is defined by

$$\Lambda(T) \equiv \left(\frac{\hbar^2}{2\pi m k_B T}\right)^{\frac{1}{2}}. \tag{C.2}$$

Under periodic boundary conditions, the integral should be performed inside the cell with R_{cell}:

$$Z(N,V,T) = \frac{1}{N!\Lambda(T)^{3N}} \int_0^{R_{\text{cell}}} (d\mathbf{r})^N \exp\left[-\frac{U(\mathbf{r}^N)}{k_B T}\right]. \tag{C.3}$$

Introducing the scaled coordinates $\mathbf{r}_i = R_{\text{cell}}\mathbf{s}_i$ for $i = 1, 2, \cdots, N$, the integral can be transformed into a form which is independent of the volume V. We define the following reduced partition function:

$$Z_{\text{red}}(N,V,T) = \frac{V^N}{N!\Lambda(T)^{3N}} \int_0^1 (d\mathbf{s})^N \exp\left[-\frac{U(\mathbf{s}^N)}{k_B T}\right]. \tag{C.4}$$

The idea of the Gibbs ensemble method is that a coexistent system can be represented by two cells interacting with each other by exchanging their particles and volume. One cell corresponds to the pure gas phase and the other corresponds to the pure liquid phase. The introduction of two cells enables us to express a

66

coexistent system free from the difficulty of the interface which is inevitable in the single cell used in the Metropolis method. Our task is to construct the partition function for the combined system, which is expressed by the products of the two partition functions. Assuming that N_1 particles are in one cell with a volume V_1 and $N - N_1$ particles are in the other cell with a volume $V - V_1$, the partition function for the total system is given as follows:

$$
\begin{aligned}
& Z_{\mathrm{red}}(N - N_1, V - V_1, T) Z_{\mathrm{red}}(N_1, V_1, T) \\
= \quad & \frac{V_1^{N_1} (V - V_1)^{N - N_1}}{\Lambda(T)^{3N} N_1! (N - N_1)!} \\
& \times \quad \int_0^1 (d\mathbf{s}_1)^{N_1} \int_0^1 (d\mathbf{s}_2)^{N - N_1} \exp\left[-\frac{U(\mathbf{s}_1^{N_1})}{k_B T} \right] \exp\left[-\frac{U(\mathbf{s}_2^{N - N_1})}{k_B T} \right].
\end{aligned}
\tag{C.5}
$$

Notice that the total volume V and the total number of particles N are constant and N_1 and V_1 are variables. The partition function of the Gibbs ensemble method is defined as the summation and integration of the $Z_{\mathrm{red}}(N - N_1, V - V_1, T) Z_{\mathrm{red}}(N_1, V_1, T)$ over N_1 and V_1:

$$
Q_{\mathrm{Gibbs}}(N, V, T) \equiv \frac{1}{V} \int_0^V dV_1 \sum_{N_1=0}^{N} Z_{\mathrm{red}}(N - N_1, V - V_1, T) Z_{\mathrm{red}}(N_1, V_1, T).
\tag{C.6}
$$

Substituting Z_{red} into the above expression, $Q_{\mathrm{Gibbs}}(N, V, T)$ is expressed as follows:

$$
\begin{aligned}
Q_{\mathrm{Gibbs}}(N, V, T) \quad = \quad & \sum_{N_1=0}^{N} \int_0^V dV_1 \int_0^1 (d\mathbf{s}_1)^{N_1} \int_0^1 (d\mathbf{s}_2)^{N - N_1} \\
\times \quad & \frac{V_1^{N_1} (V - V_1)^{N - N_1}}{N_1! (N - N_1)!} \exp\left[-\frac{U(\mathbf{s}_1^{N_1}) + U(\mathbf{s}_2^{N - N_1})}{k_B T} \right] \frac{1}{V \Lambda(T)^{3N}}.
\end{aligned}
\tag{C.7}
$$

The integrand of the $Q_{\mathrm{Gibbs}}(N, V, T)$ represents the probability of finding a specific configuration for the system composed of two cells, where the degrees of freedom for the volume and the number of particle are included besides the energy. To assure that the Monte Carlo process covers all possible values of V_1, the integral of V_1 is transformed into the following form:

$$
\int_0^V dV_1 = \int_{-\infty}^{\infty} d\log\left(\frac{V_1}{V - V_1} \right) \frac{V_1 (V - V_1)}{V}.
\tag{C.8}
$$

In this case, the Q_{Gibbs} is expressed as follows:

$$
\begin{aligned}
& Q_{\mathrm{Gibbs}}(N, V, T) \\
= \quad & \frac{1}{V^2 \Lambda(T)^{3N}} \sum_{N_1=0}^{N} \int_{-\infty}^{\infty} d\log\left(\frac{V_1}{V - V_1} \right) \int_0^1 (d\mathbf{s}_1)^{N_1} \int_0^1 (d\mathbf{s}_2)^{N - N_1} \\
\times \quad & \frac{1}{N_1! (N - N_1)!} V_1^{N_1+1} (V - V_1)^{N - N_1 + 1} \exp\left[-\frac{U(\mathbf{s}_1^{N_1}) + U(\mathbf{s}_2^{N - N_1})}{k_B T} \right].
\end{aligned}
\tag{C.9}
$$

The probability of finding a specific configuration is identified as:

$$\mathcal{N}_{\text{Gibbs}}(N_1, V_1, \mathbf{s}^N) = \frac{1}{N_1!(N-N_1)!} V_1^{N_1+1} (V-V_1)^{N-N_1+1} \exp\left[-\frac{U(\mathbf{s}^N)}{k_B T}\right], \quad (C.10)$$

where the total energy is introduced by

$$U(\mathbf{s}^N) = U(\mathbf{s}_1^{N_1}) + U(\mathbf{s}_2^{N-N_1}). \quad (C.11)$$

We see that $\mathcal{N}_{\text{Gibbs}}(N_1, V_1, \mathbf{s}^N)$ is an extension of the probability used in the Metropolis method. When the configuration is modified from $\mathcal{N}_{\text{Gibbs}}(\text{old})$ to $\mathcal{N}_{\text{Gibbs}}(\text{new})$, the acceptance probability $\text{acc}(\text{old} \rightarrow \text{new})$ is related to them under the detailed balance condition as follows:

$$\frac{\text{acc}(\text{old} \rightarrow \text{new})}{\text{acc}(\text{new} \rightarrow \text{old})} = \frac{\mathcal{N}_{\text{Gibbs}}(\text{new})}{\mathcal{N}_{\text{Gibbs}}(\text{old})}. \quad (C.12)$$

Three variables in $\mathcal{N}_{\text{Gibbs}}(N_1, V_1, \mathbf{s}^N)$ lead to three ways of modifications:

(1) Displacement of a randomly selected particle

$$\frac{\mathcal{N}_{\text{Gibbs}}(N_1, V_1, \mathbf{s}_{\text{new}}^N)}{\mathcal{N}_{\text{Gibbs}}(N_1, V_1, \mathbf{s}_{\text{old}}^N)} = \exp\left[-\frac{U(\mathbf{s}_{\text{new}}^N) - U(\mathbf{s}_{\text{old}}^N)}{k_B T}\right], \quad (C.13)$$

$$\text{acc}(\text{old} \rightarrow \text{new}) = \min\left\{1, \exp\left[-\frac{U(\mathbf{s}_{\text{new}}^N) - U(\mathbf{s}_{\text{old}}^N)}{k_B T}\right]\right\}. \quad (C.14)$$

(2) Change of the volume in such a way that the total volume remains constant

$$\frac{\mathcal{N}_{\text{Gibbs}}(N_1, V_{1\ \text{new}})}{\mathcal{N}_{\text{Gibbs}}(N_1, V_{1\ \text{old}})} = \left(\frac{V_{1\ \text{new}}}{V_{1\ \text{old}}}\right)^{N_1+1} \left(\frac{V-V_{1\ \text{new}}}{V-V_{1\ \text{old}}}\right)^{N-N_1+1}$$
$$\times \exp\left[-\frac{U(\mathbf{s}_{\text{new}}^N) - U(\mathbf{s}_{\text{old}}^N)}{k_B T}\right], \quad (C.15)$$

$$\text{acc}(\text{old} \rightarrow \text{new}) = \min\left\{1, \left(\frac{V_{1\ \text{new}}}{V_{1\ \text{old}}}\right)^{N_1+1} \left(\frac{V-V_{1\ \text{new}}}{V-V_{1\ \text{old}}}\right)^{N-N_1+1}\right.$$
$$\left.\times \exp\left[-\frac{U(\mathbf{s}_{\text{new}}^N) - U(\mathbf{s}_{\text{old}}^N)}{k_B T}\right]\right\}.$$
$$(C.16)$$

(3) Transfer of a randomly selected particle from one cell to the other

$$\frac{\mathcal{N}_{\text{Gibbs}}(N_1 - 1, V_1)}{\mathcal{N}_{\text{Gibbs}}(N_1, V_1)} = \frac{(V-V_1)N_1}{V_1(N-N_1+1)} \exp\left[-\frac{U(\mathbf{s}_{\text{new}}^N) - U(\mathbf{s}_{\text{old}}^N)}{k_B T}\right], \quad (C.17)$$

$$\text{acc}(\text{old} \rightarrow \text{new}) = \min\left\{1, \frac{(V-V_1)N_1}{V_1(N-N_1+1)} \exp\left[-\frac{U(\mathbf{s}_{\text{new}}^N) - U(\mathbf{s}_{\text{old}}^N)}{k_B T}\right]\right\}.$$
$$(C.18)$$

Notice that the minimum function is used to evaluate which is larger in $\mathcal{N}_{\text{Gibbs}}(\text{old})$ and $\mathcal{N}_{\text{Gibbs}}(\text{new})$. In practice, a random number in the range $[0,1]$ is used in the code.

T=0.75

T=0.90

$\rho\ (\sigma^{-3})$

Monte Carlo cycles

Monte Carlo cycles

T=0.95

the coexistence curve
for Lennard Jones particles

$\rho\ (\sigma^{-3})$

Monte Carlo cycles
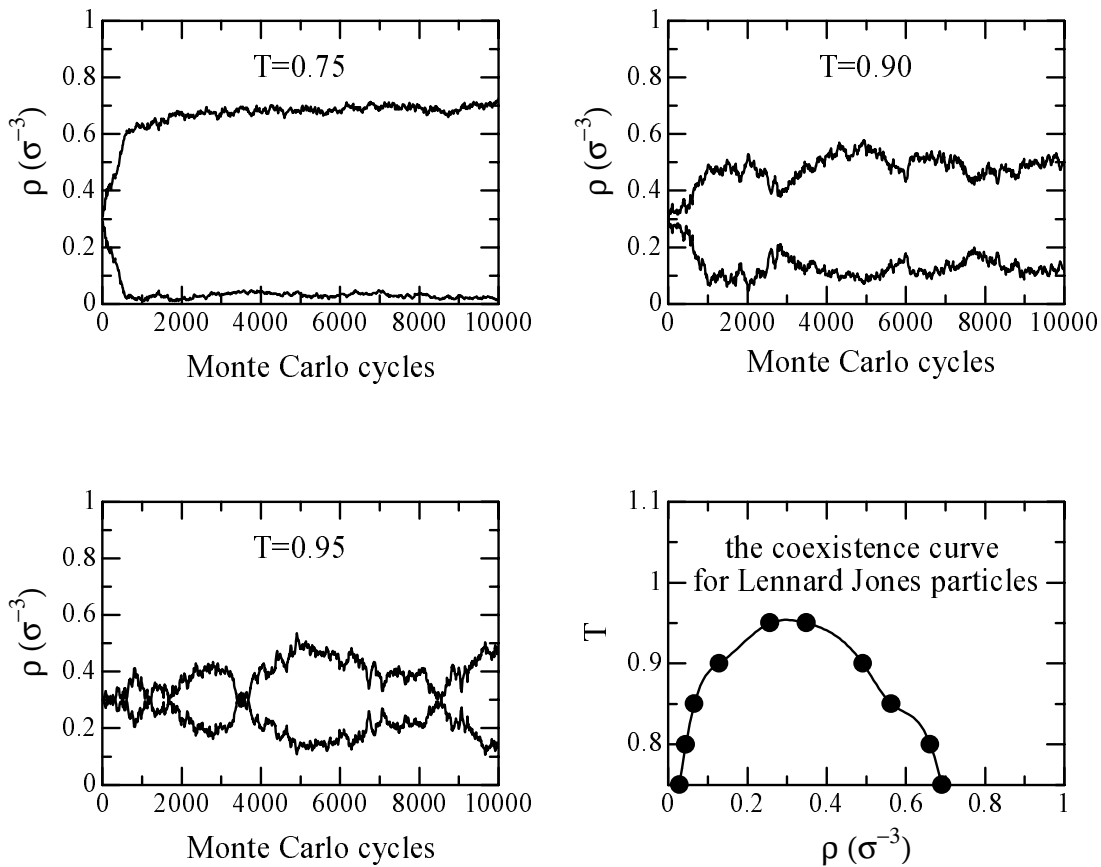
$\rho\ (\sigma^{-3})$

Figure C.1: The Density of the two cells of the Gibbs ensemble method as a function of the number of Monte Carlo cycles for a system of Lennard-Jones particles and the calculated coexistence curve. The particle number is 256.

C.2   Simulation results

Let us consider an actual calculation for the Lennard-Jones system. Figure C.1 shows the density of the two cells as a function of the number of Monte Carlo cycles composed of the above three kinds of modifications. At the beginning of the simulation, both densities of the two cells are set at $\rho = 0.3$. When the given temperature is below the critical temperature, the density of one cell increases and the density of the other cell decreases as the Monte Calro cycles proceeds. After a lot of modifications are carried out, the increased density fluctuates around the liquid density and the decreased density fluctuates around the gas density, where the total system is in thermal equilibrium at a given temperature.

The lower the given temperature is, the larger the difference between liquid density and gas density becomes. Above the critical temperature, both densities of the two cells fluctuates around the initial density, that is, the liquid phase and the

gas phase are not separated. We can see that the critical temperature is $T = 0.95$ in the figure.

Appendix D

Van der Waals gas

In this appendix, we shows the relation between the spinodal region and the coexistent region for van der Waals gas. The pressure and the chemical potential of van der Waals gas are calculated as follows [39]:

$$p(\rho, T) = \frac{T\rho}{1-\rho} - \rho^2\Gamma, \tag{D.1}$$

$$\mu(\rho, T) = T\left[\log\{\rho\Lambda(T)^3\} - 1 + \log\left(\frac{\rho}{1-\rho}\right) + \frac{\rho}{1-\rho}\right] - 2\rho\Gamma, \tag{D.2}$$

where $\Gamma > 0$ is a constant introduced in van der Waals approximation, which depends on the details of the interactions and $\Lambda(T)$ is given by

$$\Lambda(T) = \left(\frac{\hbar^2}{2\pi M k_B T}\right)^{\frac{1}{2}}. \tag{D.3}$$

First, we calculate critical values. The critical point is determined by the following conditions:

$$\frac{\partial P(\rho, T)}{\partial \rho} = 0, \tag{D.4}$$

$$\frac{\partial^2 P(\rho, T)}{\partial \rho^2} = 0. \tag{D.5}$$

The solution of these equations are obtained as follows:

$$P_{\rm c} = \frac{\Gamma}{27}, \qquad T_{\rm c} = \frac{8\Gamma}{27}, \qquad \rho_{\rm c} = \frac{1}{3}. \tag{D.6}$$

D.1 Coexistence curve

Let us calculate the coexistence curve, which is obtained by solving two phase coexistent conditions:

$$P(\rho_1, T) = P(\rho_2, T), \tag{D.7}$$

$$\mu(\rho_1, T) = \mu(\rho_2, T), \tag{D.8}$$

71

where ρ_1 is the density of the liquid phase and ρ_2 is that of the gas phase. Using normalized variables with the unit of critical value obtained in Eq. (D.6), these two conditions are transformed into the following two relations.

$$8\hat{T} = (3 - \hat{\rho}_1)(3 - \hat{\rho}_2)(\hat{\rho}_1 + \hat{\rho}_2), \tag{D.9}$$

$$\hat{T} \log\left[\frac{\hat{\rho}_1(3 - \hat{\rho}_2)}{\hat{\rho}_2(3 - \hat{\rho}_1)}\right] = \frac{3}{8}(\hat{\rho}_1 - \hat{\rho}_2)(6 - \hat{\rho}_1 - \hat{\rho}_2), \tag{D.10}$$

where $\hat{T} = \frac{T}{T_c}$, $\hat{\rho}_1 = \frac{\rho_1}{\rho_c}$ and $\hat{\rho}_2 = \frac{\rho_2}{\rho_c}$. The above simultaneous equations can be solved numerically.

D.2 Isothermal spinodal region

The normalized pressure $\hat{P} = \frac{P}{P_c}$ is expressed as follows:

$$\hat{P}(\hat{\rho}, \hat{T}) = \frac{8\hat{\rho}}{3 - \hat{\rho}}\hat{T} - 3\hat{\rho}^2. \tag{D.11}$$

The isothermal spinodal region is determined by solving the following equation.

$$\frac{\partial \hat{P}(\hat{\rho}, \hat{T})}{\partial \hat{\rho}} = -6\hat{\rho} + \frac{24\hat{T}}{(-3 + \hat{\rho})^2} = 0. \tag{D.12}$$

D.3 Adiabatic spinodal region

When the entropy is constant, the pressure and the temperature are expressed in terms of a constant C as follows:

$$\hat{P} = \frac{8}{3}C\left(\frac{3\hat{\rho}}{3 - \hat{\rho}}\right)^{\frac{5}{3}} - 3\hat{\rho}^2, \tag{D.13}$$

$$\hat{T} = C\left(\frac{3\hat{\rho}}{3 - \hat{\rho}}\right)^{\frac{2}{3}}. \tag{D.14}$$

To calculate the adiabatic spinodal region in the density-temperature plane, we calculate the derivative of the pressure with respect to the density on the condition that the entropy is constant:

$$\frac{\partial \hat{P}}{\partial \hat{\rho}} = -6\hat{\rho} + 40C\frac{(3\hat{\rho})^{\frac{2}{3}}}{(3 - \hat{\rho})^{\frac{8}{3}}} = 0, \tag{D.15}$$

$$\hat{T} = C\left(\frac{3\hat{\rho}}{3 - \hat{\rho}}\right)^{\frac{2}{3}}. \tag{D.16}$$

The above equations can be solved numerically using C as a parameter. Figure D.1 shows the coexistent region, isothermal spinodal, and adiabatic spinodal curve for van der Waals gas.
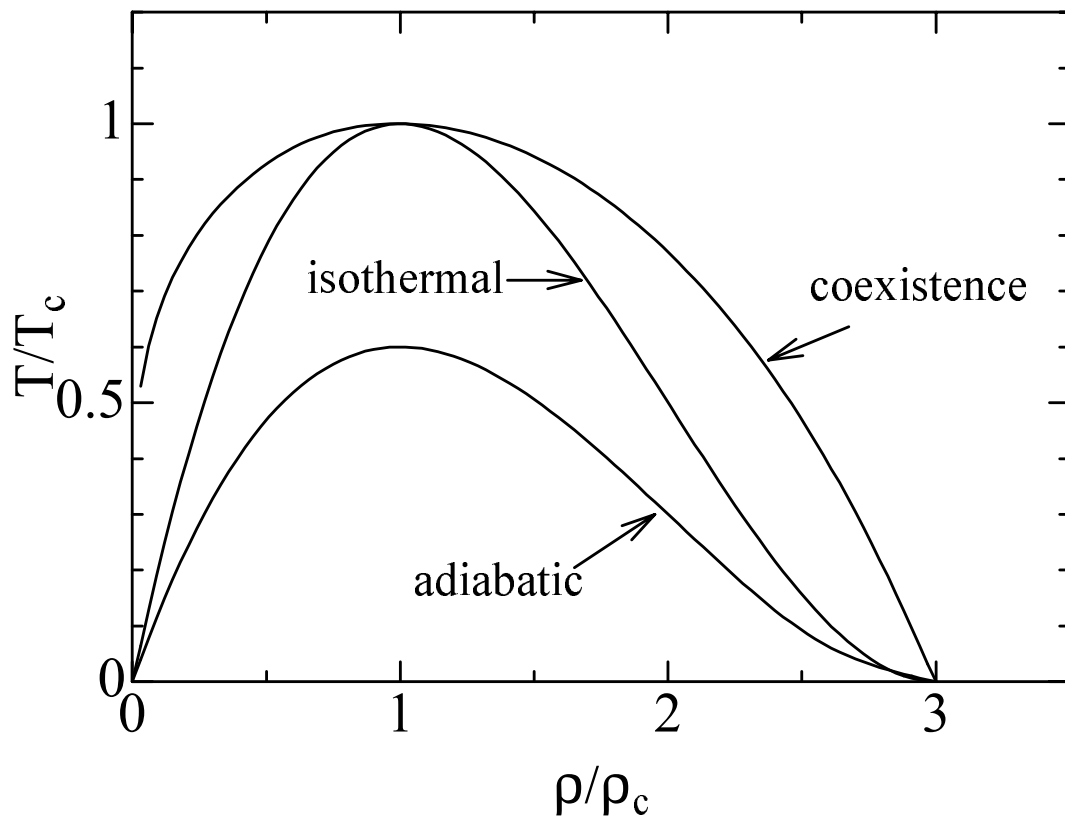
Figure D.1: The coexistent region, isothermal spinodal, and adiabatic spinodal curve for van der Waals gas

Appendix E

Fisher's droplet model

Fisher's droplet model is based on the partition function for the grand canonical ensemble [18]. Assuming that $Z(A, V, T)$ is the partition function for the single fragment composed of A particles at T in a volume V, $Z(A, V, T)$ is expressed as follows:

$$
\begin{aligned}
Z(A, V, T) &= \frac{1}{A! \Lambda^{3A}} \int (d\mathbf{r})^A \exp\left[-\frac{U(A)}{k_B T}\right], \\
\Lambda^{-2} &\equiv \frac{2\pi M k_B T}{h^2},
\end{aligned}
\tag{E.1}
$$

where $U(A)$ is the total potential energy of the single fragment. The grand partition function $Z_{\mathrm{G}}(\mu, V, T)$ is represented in terms of $Z(A, V, T)$ as follows:

$$
Z_{\mathrm{G}}(\mu, V, T) = \sum_{A=0}^{\infty} \lambda^A Z(A, V, T),
\tag{E.2}
$$

where $\lambda = \exp\left[\frac{\mu}{k_B T}\right]$ is the fugacity and the μ is the chemical potential. Using the relation $Z(A = 0, V, T) = 1$, $\ln Z_{\mathrm{G}}(\mu, V, T)$ is transformed as follows:

$$
\begin{aligned}
\ln Z_{\mathrm{G}}(\mu, V, T) &= \ln\left\{1 + \sum_{A=1}^{\infty} \lambda^A Z(A, V, T)\right\} \\
&= \sum_{n=1}^{\infty} \frac{(-1)^{n-1}}{n}\left\{\sum_{A=1}^{\infty} \lambda^A Z(A, V, T)\right\}^n.
\end{aligned}
\tag{E.3}
$$

When the fragments are well separated and the interactions between fragments can be neglected, the only $n = 1$ term in the above formula is significant:

$$
\ln Z_{\mathrm{G}}(\mu, V, T) \sim \sum_{A=1}^{\infty} \lambda^A Z(A, V, T).
\tag{E.4}
$$

In order to calculate $Z(A, V, T)$, let us assume a simple form of $U(A)$ which is the potential energy of the single fragment composed of A particles:

$$
U(A) = -AE_0 + \omega \bar{s}(A),
\tag{E.5}
$$

74

where E_0 is the volume energy per particle inside the fragment , ω is a surface energy arising through loss of binding energy by particles near the surface and $\bar{s}(A)$ is the surface area of the cluster. In this case, $Z(A, V, T)$ is calculated as follows:

$$Z(A, V, T) = \frac{V}{A! \Lambda^{3A}} \int (d\mathbf{r})^{A-1} \exp\left[\frac{AE_0}{k_B T}\right] \exp\left[-\frac{\omega \bar{s}(A)}{k_B T}\right]. \tag{E.6}$$

Notice that an integral with respect to one particle is carried out and the volume V appears. The remnant integrals depend on how the particles form a fragment. Introducing $g(\bar{s}(A))$ as a combinatorial factor, $Z(A, V, T)$ is simplified further:

$$Z(A, V, T) \simeq V g(\bar{s}(A)) \exp\left[\frac{AE_0}{k_B T}\right] \exp\left[-\frac{\omega \bar{s}(A)}{k_B T}\right]. \tag{E.7}$$

The function $g(\bar{s}(A))$ is subject to the geometrical structure of the fragment. According to [18], when $\bar{s}(a)$ is very large, $g(\bar{s}(A))$ is evaluated by

$$g(\bar{s}(A)) \simeq g_0 h^{\bar{s}(A)} \bar{s}(A)^{-\frac{3}{2}\tau} \qquad (\bar{s}(A) \to \infty), \tag{E.8}$$

where g_0, h and τ are constant. In particular, τ is related to the critical exponent and satisfies $\tau \geq \frac{4}{3}$. Substituting this into $Z(A, V, T)$, $\ln Z_{\mathrm{G}}(\mu, V, T)$ is calculated as follows:

$$\ln Z_{\mathrm{G}}(\mu, V, T) = g_0 V \sum_{A=1}^{\infty} \lambda^A h^{\bar{s}(A)} \bar{s}(A)^{-\frac{3}{2}\tau} \exp\left[\frac{AE_0}{k_B T}\right] \exp\left[-\frac{\omega \bar{s}(A)}{k_B T}\right]. \tag{E.9}$$

When the fragment mass is large, the surface area $\bar{s}(A)$ is approximated by

$$\bar{s}(A) = a_0 A^{\frac{2}{3}} \qquad (A \to \infty), \tag{E.10}$$

where a_0 is a constant. Substituting this into $\bar{s}(A)$, the following relation is obtained:

$$\ln Z_{\mathrm{G}}(\mu, V, T) = g_0 V a_0^{-\frac{3}{2}\tau} \sum_{A=1}^{\infty} \lambda^A h^{\bar{s}} A^{-\tau} \exp\left[\frac{AE_0}{k_B T}\right] \exp\left[-\frac{\omega \bar{s}(A)}{k_B T}\right]. \tag{E.11}$$

On the other hand, the expectation value of the fragment mass is calculated using $\ln Z_{\mathrm{G}}(\mu, V, T)$ as follows:

$$\langle A \rangle = \lambda \frac{\partial}{\partial \lambda} \ln \Xi(T, Z; V) \equiv \sum_{A=1}^{\infty} A P(A), \tag{E.12}$$

where $P(A)$ is introduced as the fragment mass distribution. Using the expression of $\ln Z_{\mathrm{G}}(\mu, V, T)$, $P(A)$ is obtained as follows:

$$\begin{aligned} P(A) &= g_0 V a_0^{-\frac{3}{2}\tau} \lambda^A h^{\bar{s}(A)} A^{-\tau} \exp\left[\frac{AE_0}{k_B T}\right] \exp\left[-\frac{\omega \bar{s}(A)}{k_B T}\right] \\ &= P_0 h^{\bar{s}(A)} A^{-\tau} \exp\left[\frac{A(E_0 + \mu)}{k_B T}\right] \exp\left[-\frac{\omega \bar{s}(A)}{k_B T}\right], \end{aligned} \tag{E.13}$$

where a new constant P_0 is introduced. When T is equal to or above the critical temperature, the surface term can be neglected:

$$P(A) = P_0 A^{-\tau} \exp\left[\frac{A(E_0 + \mu)}{k_B T}\right] \qquad (T \geq T_c). \qquad \text{(E.14)}$$

Notice that E_0 is the binding energy per particle inside the fragment, which is regarded as the chemical potential of the liquid. Therefore, when $T = T_c$, μ is equal to $-E_0$, $P(A)$ becomes the power law:

$$P(A) = P_0 A^{-\tau} \qquad (T = T_c). \qquad \text{(E.15)}$$

Bibliography

[1] P. Bak, How nature works; the science of self-organized criticality, Springer-Verlag New York, Inc, 1996.

[2] H. J. Jensen, Self-Organized Criticality; Emergent Complex Behavior in Physical and Biological Systems, Cambridge University Press, 1998.

[3] M. Colonna, P. Chomaz, Unstable infinite nuclear matter in stochastic mean field approach, Physical Review C 49 (1994) 1908.

[4] P. Chomaz, M. Colonna, A. Guarnera, J. Randrup, Brownian one-body dynamics in nuclei, Physical Review Letters 73 (1994) 3512.

[5] M. Colonna, P. Chomaz, A. Guarnera, B. Jacquot, Spinodal instabilities in expanding fermi liquids, Physical Review C 49 (1995) 1908.

[6] S. Ayik, M. Colonna, P. Chomaz, Quantal effects on growth of instabilities in nuclear matter, Physics Letters B 353 (1995) 417.

[7] P. Finocchiaro, M. Belkacem, T. Kubo, V. Latora, A. Bonasera, Second order phase transitions: from infinite to finite systems, Nuclear Physics A 600 (1996) 236.

[8] A. Guarnera, M. Colonna, P. Chomaz, 3D stochastic mean-field simulations of the spinodal fragmentation of dilute nuclei, Physics Letters B 373 (1996) 267.

[9] M. Colonna, P. Chomaz, Spinodal decomposition in nuclear molecular dynamics, Physics Letters B 436 (1998) 1.

[10] Y. Sugawa, H. Horiuchi, Nuclear phase transition studied with antisymmetrized molecular dynamics with momentum fluctuations: A microscopic analysis without model assumption, Physical Review C 60 (1999) 064607.

[11] M. L. Gilkes, et al., Determination of critical exponents from the multifragmentation of gold nuclei, Physical Review Letters 73 (1994) 1590.

[12] M. Petrovici, et al., Cluster formation during expansion of hot and compressed nuclear matter produced in central collisions of Au on Au at 250A MeV, Physical Review Letters 74 (1995) 5001.

[13] P. F. Mastinu, et al., Circumstantial evidence for critical behavior in peripheral Au + Au collisions at 35 MeV/nucleon, Physical Review Letters 76 (1996) 2646.

[14] W. Reisdorf, et al., Central collisions of Au on Au at 150, 250 and 400 A·MeV, Nuclear Physics A 612 (1997) 493.

[15] W. Trautmann, Hot fragmentation of nuclei, Nuclear Physics A 685 (2001) 233c.

[16] O. Lopez, Experimental signatures of the nuclear liquid-gas phase transition, Nuclear Physics A 685 (2001) 246c.

[17] B. Zwieglinski, et al., Interplay of equilibrium and nonequilibrium phenomena in the nuclear liquid-gas phase transition, Nuclear Physics A 681 (2001) 275c.

[18] M. E. Fisher, The theory of equilibrium critical phenomena, Reports on progress in physics 30 (1967) 615.

[19] A. Vicentini, G. Jacucci, V. R. Pandharipande, Fragmentation of hot classical drops, Physical Review C 31 (1985) 1783.

[20] T. J. Schlagel, V. R. Pandharipande, Classical simulations of heavy-ion collisions, Physical Review C 36 (1987) 162.

[21] A. Strachan, C. O. Dorso, Temperature and energy partition in fragmentation, Physical Review C 59 (1999) 285.

[22] J. Aichelin, 'Quantum' molecular dynamics - a dynamical microscopic n-body approach to investigate fragment formation and the nuclear equation of state in heavy ion collisions, Physics Report 202 (1991) 233.

[23] H. Horiuchi, Molecular dynamics description of fragmentation, Nuclear Physics A 685 (2001) 260c.

[24] H. Feldmeier, Jürgen Schnack, Molecular dynamics for fermions, Reviews of Modern Physics 72 (2000) 655.

[25] H. Feldmeier, Liquid-gas phase transition in fermionic molecular dynamics, Nuclear Physics A 681 (2001) 398c.

[26] T. Maruyama, K. Niita, K. Oyamatsu, T. Maruyama, S. Chiba, A. Iwamoto, Quantum molecular dynamics approach to the nuclear matter below saturation density, Physical Review C 57 (1998) 655.

[27] B. L. Holian, D. E. Grady, Fragmentation by molecular dynamics: The microscopic "Big Bang", Physical Review Letters 60 (1988) 1355.

[28] S. Toxvaerd, Fragmentation of fluids by molecular dynamics, Physical Review E 58 (1998) 704.

[29] W. T. Ashurst, B. L. Holian, Droplet formation by rapid expansion of a liquid, Physical Review E 59 (1999) 6742.

[30] D. Frenkel, B. Smit, Understanding Molecular Simulation, Academic Press, 1996.

[31] S. Chikazumi, T. Maruyama, K. Niita, A. Iwamoto, QMD simulation of expanding nuclear matter, Physics Letters B 476 (2000) 273.

[32] S. Chikazumi, T. Maruyama, S. Chiba, K. Niita, A. Iwamoto, Quantum molecular dynamics simulation of expanding nuclear matter and nuclear multifragmentation, Physical Review C 63 (2001) 024602.

[33] T. Kido, T. Maruyama, K. Niita, S. Chiba, MD simulation study for nuclear matter, Nuclear Physics A 663&664 (2000) 877c.

[34] G. F. Bertsch, S. D. Gupta, A guide to microscopic models for intermediate energy heavy ion collisions, Physics Reports 160 (1988) 189.

[35] W. G. Hoover, Lecture Notes in Physics 258: Molecular Dynamics, Springer-Verlag Berlin Heidelberg, 1986.

[36] J. M. Thijssen, Computational Physics, Cambridge University Press, 1999.

[37] C. S. Kiang, Use of liquid-droplet model in calculations of the critical exponent δ, Physical Review Letters 24 (1970) 47.

[38] T. Pang, Introduction to computational physics, Cambridge University Press, 1997.

[39] A. Daanoun, C. F. Tejero, M. Baus, van der waals theory for solids, Physical Review E 50 (1994) 2913.